The Development and Control of Soft Robotic Materials Driven by Hydraulically Amplified Self-Healing Electrostatic (HASEL) Actuators

by Brian K. Johnson

B.S., Cornell University, 2017

M.S., University of Colorado Boulder, 2020

A thesis submitted to the
Faculty of the Graduate School of the
University of Colorado in partial fulfillment
of the requirement for the degree of
Doctor of Philosophy
Paul M. Rady Department of Mechanical Engineering
2022

Committee members:
Mark Rentschler
Sean Humbert
Christoph Keplinger
Nikolaus Correll
Kaushik Jayaram

Johnson, Brian K. (Ph.D., Paul M. Rady Mechanical Engineering)

The Development and Control of Soft Robotic Materials Driven by Hydraulically Amplified Self-Healing Electrostatic (HASEL) Actuators

Thesis directed by Professor Mark E. Rentschler

Abstract

Soft robotics is a growing research area focused on the development of compliant, adaptable, and bio-inspired robotic systems. Compared to traditional robotic solutions, soft robots are better suited for medical devices, wearable electronics, human-robot interaction, and other unique applications. The use of compliant materials enables design simplicity and bio-inspiration as well as entirely new functionalities not present in rigid robotic solutions.

Electrostatic actuators are an effective way to drive soft robotic motion because of their low cost, mechanical simplicity, and high actuation bandwidth. A specific class of electrostatic actuator, the Hydraulically Amplified Self-healing Electrostatic (HASEL) actuator, further improves performance. However, system integration of HASEL actuator-driven robots is lacking. One approach to solving this problem is through the use of robotic materials which integrate actuation, sensing, communication, and control through a scalable constituent unit. Developing a HASEL actuator-driven soft robotic material would enable the creation of high degree of freedom robots with increased functionality. To do so, several challenges related to the sensing and feedback control of HASEL actuators must first be addressed.

This thesis describes research efforts in the design and control of HASEL actuator-driven systems. Chapter 1 presents a literature review of soft robotics, soft actuators, and introduce the concept of robotic materials. Chapter 2 then presents a system identification and control technique for a single HASEL actuator. The system integrates a soft capacitive sensor onto the actuator. Then the control of a multi-HASEL-actuator robot using a novel magnetic sensing mechanism is presented in Chapter 3. Chapter 4 builds upon these results by introducing sTISSUE, a soft robotic material using HASEL actuators and the magnetic sensing mechanism. Multiple advanced demonstrations highlight the capabilities of this robotic material. Chapter 5 presents a multi-functional artificial potential field control method to enable highly controllable object manipulation with actuator arrays. Finally, Chapter 6 provides concluding statements and suggested next steps.

Acknowledgements

This work was not performed in a vacuum and I can not take sole responsibility for the ideas and achievements discussed here. Thank you to the Advanced Medical Technologies Laboratory, Keplinger Research Group, Bio-inspired Perception and Robotics Laboratory, Correll Lab, and especially the following individuals who contributed to the work presented here:

Vani Sundaram[1], Mantas Naris[1], Dr. Khoi Ly[1], Angela Volchko[1], Dr. Eric Acome[1], Dr. Shane K. Mitchell[1], Dr. Nick Kellaris[1], Dr. Mark E. Rentschler[1], Dr. Christoph Keplinger[1,2,3], Dr. J. Sean Humbert[1], Dr. Nikolaus Correll[2,4]

[1] Paul M. Rady Mechanical Engineering, University of Colorado Boulder
[2] Materials Science and Engineering, University of Colorado Boulder
[3] Robotic Materials Department, Max Planck Institute for Intelligent Systems
[4] Department of Computer Science, University of Colorado Boulder
(affiliations at the time of contribution)

Further acknowledgements of specific contributions are mentioned at the end of each chapter of this thesis.

This work was also supported by the National Science Foundation under Grants 1739452 and 1650115, by the Air Force Office of Scientific Research (FA9550-18-1-0243), and by the Max Planck Institute for Intelligent Systems.

Additional thanks to Mark E. Rentschler for always helping to guide me in my Ph.D. career and for providing unbiased feedback and opinions. Special thanks to my family, to Beilei, and to Vani and all my other friends who helped me along this journey.

Contents

List of Tables

List of Figures

Chapter 1

Introduction and literature review

In this chapter I provide an overview of the field of soft robotics and discuss several subdomains; I describe some popular applications of soft robots, discuss notable robots that have been developed in recent years, and compare soft actuation technologies. I discuss weaknesses of current soft robot technologies in comparison to biological systems and introduce the concept of robotic materials as a potential solution. The chapter concludes with a summary of findings from the literature review and an outline of the remaining chapters of this thesis.

1.1 Soft robots

In the simplest terms, a ”robot” is a machine which can automatically execute actions to accomplish a task. Robots are an integral part of worldwide economics and manufacturing processes, and robotic labor increases task speed, efficiency, and precision over human labor [1–4]. The majority of these robots are made of rigid materials and implement precise control schemes using complex arrangements of actuators and sensors. This approach requires complexity because each actuator within the robot typically only has one degree of freedom, and degrees of freedom can only be introduced by adding new series of joints and linkages [5]. Likewise, the control of such robots also requires complexity because the actuators and joints are more susceptible to external disturbances due to their rigidity.

Soft robots stand in contrast to their traditional counterparts through material elasticity and compliance. A compliant material is that which has low mechanical stiffness which renders it able to deform more easily compared to rigid materials. The range of elastic deformation is also higher than rigid materials, allowing greater deformation without structural damage. Soft robots are simply defined as robots built with compliant materials. This enables design simplicity, multi-functionality, adaptability, and mechanisms inspired by biology [5–11]. In contrast to rigid robots, the compliance of soft robots allows them to more easily reject external disturbances and adapt to unknown conditions. The compliant structure of the robot allows disturbances and unknowns to be transformed into local elastic deformations, resulting in reduced digital computational effort [5,10]: this ”embodied intelligence” is another advantage of soft robotic systems.

Applications of soft robots are plentiful. Robot compliance is particularly useful for medical devices because the mechanical properties of soft materials are similar to those of tissue, enabling the creation of artificial organs, rehabilitation devices, and surgical robots which can more easily interface with human biology [8, 9, 12–18]. Wearable technology is another field in which soft robotics can excel for similar reasons [12,16,19–22] - the typical strains associated with human body movement are within the range of today's soft actuators and sensors. Such wearable robots can provide real-time measurement and feedback of human motion. Human-robot interaction outside of wearable technology can also be improved through soft robotics [5, 6, 23–27]. Accidental human injury caused by a robot executing its task is a continual concern for industrial and medical robots because of the rigidity, strength, and lack of feedback of available robots. The use of soft materials for robotics poses a lower risk to human injury and may also affect human perception of robots. Outside of all these advantages, soft robots also enable new functionalities that are not possible in traditional rigid robotic systems [5, 28–32], most notably ”bio-inspired” functionalities: robot designs and capabilities which draw inspiration from the design and function of biological systems.

1.2 Relevant examples

The compliance of soft robots make them a popular choice for specific designs, like deforming grippers, continuum devices, shape displays, wearable systems, and adaptable mobile robots. One well-cited example is a multigait mobile soft robot created by Shepherd et al. [33]. The robot is entirely soft due to its molded silicone body and can achieve multiple forms of locomotion. The fabrication method is rapid and simple compared to the resulting functionality. The robot also demonstrates an ability to deform underneath obstacles, highlighting the compliant advantage of soft robots.

A mobile soft robot with even more advanced obstacle navigation capabilities is a 'growth'-based inflatable snake robot from Hawkes et al. [34]. In this case, the deformable and continuous aspect of the robot allows it to easily twist through variable environments. Careful material selection enables the robot to traverse across fire or other hazards without damage. The authors also suggest additional functionality that can be induced by the robot's compliance, such as a mobile radio antenna. Another snake-like soft robot is able to navigate beneath sand [35]. These snake-like mobile robots are much more difficult to implement in a rigid form, as they require complex segment joints, more actuators, and more complex control schemes [36].

In addition to land-based soft robots, swimming soft robots can also utilize compliance to their advantage to create fish-like biomimetic swim strokes. One example by Marchese et al. is a robot with a complaint body that enables multifunctional swimming [37]. The robot can mimic a rapid 'escape' maneuver to avoid danger in addition to its forward swim - both functions are a result of soft body compliance. Other soft swimming robots demonstrate simple single-actuator designs to induce smooth forward swimming motion [38]. This compliance-induced motion can benefit from periodic resonance for increased energy efficiency [39], and it avoids propeller-driven problems like debris blocking or damaging the propeller.

Another popular realm of soft robots is continuum manipulators. One foundational example is a tentacle soft robot which has longitudinal and transverse actuation modes, mimicking the muscular hydrostat within an octopus [40]. The design took inspiration from octopus biology to achieve more advanced motion. The authors also demonstrate similar functionality to an octopus arm such as object grasping and manipulation. In contrast to traditional rigid robot arms, these soft devices have a theoretical infinite number of degrees of freedom (DOF), resulting in increased adaptability but also the need for additional dynamic modeling and control theory [36, 41].

Compliance is valuable for underactuated robots, especially grippers. An underactuated, soft gripper by Wang et al. was able to grab a variety of delicate food items using the same basic control method [42]. The compliance of the gripper's fingers allow them to bend around objects, enabling higher grip adhesion and reduce control complexity compared to rigid robotic grippers. This approach was applied by another research group to an underwater gripper designed to retrieve coral samples [43]; the variability in shape, texture, and fragility of such corals make a soft robot solution particularly attractive.

In the realm of wearable technology, soft robots excel because of their ability to conform to the human body. A soft robotic glove developed by Polygerinos et al. provides assistive input to hand motions, gripping, and object manipulation [44]. Using soft materials results in a simple, lightweight, and adaptive glove design which can fit a variety of different hand sizes. The electronics and driving systems for the glove can be worn on a belt, allowing for full mobility and portability. Such soft devices have life-changing applications in the medical field including assistive living and injury rehabilitation [44].

While there are numerous other applications and successful demonstrations of soft robots, the above examples highlight the breadth and depth of soft robot technologies today.

1.3 Soft actuation

All of the aforementioned examples use some form of soft actuation to drive their motion. Just like a soft robot, a soft actuator is made principally of compliant materials. Because of the premium placed on mechanical compliance in soft robotic systems, the soft robotics field is intertwined with the field of soft actuators. Many types of soft actuators have been developed, three of the most commonly used being pneumatic [15, 25, 45–51], shape memory alloy [52–57], and electrostatic [30,45,50,54,54,57–68]. While other soft actuator technologies exist [53,57], the focus of this thesis is on electrostatic actuation - the other two popular actuators are discussed in order to compare and contrast technologies and to motivate our focus on electrostatic actuation.

Pneumatic actuators rely on the pressurization of a fluid inside a soft pressure vessel to induce strain. By selectively designing stiffer or softer segments of the pressure vessel, deformation and strain can be induced [69]. Pneumatic actuators are characterized by high force output and strain, but they typically have low actuation frequency (approximately 1 Hz) and require pumps and valves to control pressurization and depressurization of the actuator [50]. Because of the difficulty in controlling multiple pressure channels, researchers are looking towards pneumatic-based computation methods to offset the complexity in digital computation and valve design [70,71]. The pumps required to pressurize the working fluid are often very large and loud, with reported noise levels up to 70 dB [72]. Despite these challenges however, many soft robots today utilize pneumatic actuators [33,37,40,43,73], and some have demonstrated untethered operation using a miniaturized pump or pressurized fluid source [43,73].

Shape memory alloy (SMA) actuators operate based on unique material chemistry. The molecular structure of the SMA exhibits 'shape memory', which causes the substance to undergo a mechanical transformation under thermal stimulus [56]. The application of heat causes the SMA to expand or contract depending on its shape memory. Coiled springs are a popular shape for SMA actuators [52, 56]. SMA actuators have a very high power-to-weight ratio because the wire-like SMA is light and thin, but they typically have small strain outputs [52]. In addition, the actuation bandwidth is even lower than pneumatic actuators due to the time required to heat the SMA, and the stroke output is nonlinear because it takes several times longer for the SMA to cool to its undeformed temperature [57]. The high temperature required for actuation also presents a design and integration problem, as the temperatures could damage other components within the robot. These systems are also power intensive due to the energy needed to heat the SMA.

In comparison to those forms of actuation, electrostatic actuators use the principal of electrostatic attraction to create force. A voltage is applied across two electrodes which generates an attractive force between them. This force is transformed into actuator strain [30, 58]. In dielectric elastomer actuators (DEAs), this strain comes from the deformation of an incompressible elastomer that lies between the two electrodes [68, 74]. Other actuators use electrostatic force to pressurize a fluid, acting in some sense as a pneumatic actuator [62, 63, 75]. One application of this approach is small-scale pumps [76–78]. Electrostatic principles have also been applied to jamming-type actuators [79] and controllable optical lenses [80, 81]. Electrostatic actuators are typically lower force compared to other soft actuators, but achieve fast actuation in the 10s of Hz with a simple design [50]. The maximum actuation frequency bandwidth is often an order of magnitude above fluidic actuators [82]. They also have high energy density and high power output for their mass [67, 83]. However, the voltages required for electrostatic actuators are typically in the kiloVolt (kV) range, and the electronics to supply high voltage power are often bulky or expensive [63, 84]. Like pneumatically-driven systems, however, there are examples of untethered electrostatically-driven soft robots using miniaturized voltage sources [85, 86].

One recently developed form of electro-hydraulic actuator is the HASEL (Hydraulically Amplified Self-healing ELectrostatic) actuator [63, 64] which is based on both electrostatic and hydraulic actuation principles. Like electrostatic actuators, HASEL actuators generate force from the electrostatic attraction of two oppositely charged electrodes. However, instead of an elastomer between the electrodes, as in DEAs, there is a pouch of dielectric fluid encased in a thin film. As the electrodes are drawn together, the cavity of fluid is pressurized and changes shape due to Maxwell stress, which results in a strain [87]. Unlike the previously mentioned examples of electro-hydraulic actuators, HASEL actuators do not require a rigid backing to provide pressurization of the dielectric fluid. HASEL actuators exhibit similar performance characteristics to mammalian skeletal muscle, a benchmark for soft actuator performance [64]. In comparison to typical other fluidic or SMA actuators, HASEL actuators are also capable of high frequency actuation up to 100 Hz in some designs [88].

The actuation principals of HASEL actuators can be applied to many different geometries and form factors. A planar HASEL actuator was made from a stretchable elastomer and functioned the same way as laterally stretched DEAs [89]. Other forms such as a linear expanding "folded HASEL actuator" and a bending HASEL actuator are possible [88, 90]. HASEL actuators are also capable of capacitive self-sensing because of the relationship between the strain of the actuator and its internal capacitance [64, 91, 92]. In addition, their operation can be reversed, allowing them to function as energy generators [93]. Higher performing actuators have also been created using thin-film polymers and unique geometries [64, 67, 78]. As a result of these recent advancements, polymer film-based HASEL actuators are practical for a wide range of applications [62, 93–95]. HASEL actuators are receiving increased scientific and commercial interest and have exciting use-cases, but are still a new and relatively undeveloped technology.

While soft electrostatic actuator technologies continue to expand and improve, control of such systems using integrated sensing and electronics is a less mature domain. Many electrostatic soft robots use pre-programmed or open loop control schemes to drive their motion [63, 84, 85, 96, 97]. In other cases, very simplistic state feedback, lookup tables, or single-state PID control is applied [98–101]. While this is suitable for basic demonstrations of such technologies, these types of controllers do not enable complex, adaptive, or autonomous robotic motion. Another challenge is that soft actuators often exhibit nonlinear responses, increasing the complexity of system kinematics, modeling, and controller design in some cases [99, 100].

Another weakness in the current literature is that experimental control hardware is often not practical for real-world application. Often, large and expensive data acquisition (DAQ) units are required to collect data for closed loop control [101]. Function generators or other benchtop amplifiers are also used to generate high voltage for the electrostatic actuations or for generating control input signals [63, 64, 91, 100]. In addition, the sensors used for feedback control in some experimental systems are not integrated onto the robot (this includes large laser position sensors, motion capture camera systems, and particle tracking systems which do not translate out of the laboratory environment). For electrostatic soft robots to function fully untethered or with more compact support systems, further improvements are required for soft robot electronics and control systems.

1.4 High degree-of-freedom soft robots

However, advancing the field of soft robotics requires more than improving a single actuator. The prominent soft robot examples highlighted in this introduction all have relatively low DOF; they use a small number (typically less than 10) of actuators such as the ones described above in addition to a small number of sensors (or no sensors). While there are some advantages to using underactuated design principles, such as in robotic gripper designs which use a low DOF to their advantage, the overall multifunctionality (the ability to perform a variety of tasks) of these robots is limited due to their DOF. Today's soft robots can crawl, swim, or grasp objects, but are typically built for that sole task, limiting their multifunctionality and adaptability to different situations [102].

In comparison, biological structures are extremely multifunctional. A human being can not only walk, but can run, jump, crawl, swim, grasp objects, and manipulate the environment with dexterity using multiple limbs; meanwhile, the body possesses a suite of sensors which provide information about temperatures, textures, and forces. Even less complex biology like a common bird is highly multifunctional. Beyond the complexities of controlling these systems, the reason biology is able to achieve these multiple functions is due to their high degrees of freedom: the human body uses over 600 muscle groups in coordination with millions of various sensory receptors throughout the body and skin [103, 104]. In addition, these complex biological systems take advantage of "emergent properties" [105, 106], capabilities which arise from organizational structure. In other words, the functionality of the system is greater than the sum of the individual components. Bridging this gap in DOF by increasing the number of integrated actuators, sensors, and control loops may help soft robots become more like biology: multifunctional and adaptable to a variety of environments and situations.

However, high-DOF soft robots like actuator arrays have seen many challenges in their development and implementation. Such actuator arrays have been driven by either fluidic [107–109], electrostatic [62, 110, 111], or other forms of actuation [112–114], and have been scaled from the millimeter range [109] to the decimeter range [107] in the size of each actuator in the array. These actuator arrays have been used for haptic user interfaces [62,108,109,111,115–117], object-conveying surfaces [107,109–112,118–120], and shape morphing structures [71,113,114,119,120], showing that high-DOF systems can yield increased functionality.

Yet such systems still face limitations and challenges in their development. This includes the integration of subsystems like electronics, sensors, actuators, and power sources. On the hardware end, both electrostatic and fluidic actuator arrays face issues when scaled from a single actuator up to higher-dimensional arrays; the challenges of individual channel control of each actuator often limit the robot to 15-30 actuators total [109, 113, 115, 116]. Other systems with large numbers of actuators have been reported but are often under-actuated [119], not possessing control authority over every actuator. In addition, many systems contain no direct sensing, and adding state measurements of each actuator through sensing adds another layer of complexity to these devices. HASEL or other electrostatic actuators are particularly prone to these complexities because the high voltages associated with actuation tend to interfere with nearby electronics including some state sensors [121].

There are also many challenges in the control domain in implementing high-DOF soft robots. Many soft actuator arrays only demonstrate open loop or pre-programmed control schemes with limited adaptability [110]. Particularly dynamic environments like object manipulation using actuator arrays are either reduced to simple quasi-static problems [109] or only demonstrate dynamics far below the maximum capabilities of the system [112]. Those actuator arrays which do demonstrate closed loop object manipulation have not openly published the control algorithms or methods [107, 122], and are often made using rigid robotic components.

One approach to designing improved soft robotic systems with high DOF is through the interdisciplinary concept of ”robotic materials” [102, 123, 124]. The design philosophy of such robotic materials is centered on a basic set of constituent units which are repeated within a structural matrix. These units contain actuation, sensing, communication, and computation; coordination of all units in the material results in higher-level global functionality [124]. This is a similar concept to "programmable matter" which utilizes small, modular, repeated units to achieve larger-scale robotic operation [125]. Other approaches to the "robot material" concept are the development of electro-mechanical elastomers which can be integrated into actuators and sensors into a conglomerate soft device [126]. The design philosophy of robotic materials mirrors biological organization, which uses constituent cells that build into larger tissues, organs, and organisms through interaction. Like biology, robotic materials may also yield emergent capabilities, granting greater robot capability without an increase in complexity [105,106]. By focusing on the development of a single repeatable unit following the robotic materials concept, we can reduce the complexity in designing and controlling soft actuator arrays. Developing these soft robotic materials could thus lead to increased capabilities within the soft robotics field.

Existing robotic materials are limited, however. One example of a highly repeatable robotic material is "Blinky Blocks" which demonstrate high-speed communication and control albeit without actuation [127]. Another modular system incorporated actuation, but only demonstrated a grouping of five modules [128]. Likewise, a wearable dress incorporating a robotic material demonstrated the advantages of this approach but with only a handful of actuators and sensors [129]. In addition, none of the demonstrated systems use soft actuation or sensing, relying instead of rigid robot solutions like DC motors.

1.5 Conclusions and outline

Due to the existing performance limitations of soft robotics (especially when compared to biology), there is a strong argument to develop soft robotic materials which can integrate high-DOF actuation, sensing, control, and communication to enable multifunctionality, intelligence, and adaptability in the next generation of soft robots. As discussed previously, electrostatic actuators like HASEL actuators are an attractive choice to drive such a soft robotic material due to their increased performance characteristics when compared to other soft actuators. To move in this direction, however, several small- and large-scale developments must be achieved. First, more robust system identification and control techniques are required for electrostatic actuators before more advanced robots can be constructed [30]. In addition, sensor integration needs to be improved as the large electric fields produced by electrostatic actuators create sensing challenges [58,121]. Electrostatic circuitry and control must also be improved to enable multiple actuators to be independently controlled from a single voltage source without the use of large benchtop setups [30, 61]. Then, these systems can be scaled up to form high-DOF soft robotic materials. Finally, after developing these systems, more advanced control algorithms must also be created to fully take advantage of these robotic materials and achieve diverse multifunctionality [102].

I begin in Chapter 2 where I present a system identification and control technique for a folded HASEL actuator. The system integrates a soft capacitive sensor onto the actuator, and the system model and controller are validated through closed loop control experiments. This is a small yet necessary step in building larger HASEL actuator-driven systems like a soft robotic material.

Chapter 3 expands upon the single actuator work of Chapter 2 into multi-actuator, multi-sensor systems. I discuss my work related to a magnetic sensing mechanism for electrostatic actuators, including an application of the system identification technique in Chapter 2 as well as the kinematics and control of a multi-HASEL actuator robot.

Chapter 4 builds upon the developments from Chapters 2 and 3, culminating in the creation of a HASEL actuator-driven soft robotic material, sTISSUE, which integrates the magnetic sensing mechanism and new control strategies. I present and validate a voltage regulator, displacement controller, and dynamic motion controller with nested feedback loops which drive the sTISSUE system. I then apply these controllers towards a variety of demonstrations and applications of the sTISSUE material in the form of a 10x10 shape display.

In Chapter 5, I present an artificial potential field control method for shape displays which expands upon the dynamic motion controller in Chapter 4. This is a novel application of artificial potential field theory to enable multiple motion modalities on shape displays. I validate the algorithm through quantitative and qualitative experiments on the sTISSUE shape display from Chapter 4.

Lastly, Chapter 6 provides a conclusion and summary of the work presented in this thesis and suggests next steps and future work to continue to advance the field. While the work in this thesis is focused on HASEL actuators as the electrostatic actuator system, the content presented here can be applicable to other electrostatic systems and actuator arrays as well. Finally, references are provided at the end of the document.

Chapter 2

Characterization and control of a single HASEL actuator[1]

2.1 Overview

As discussed in Chapter 1, developing easily controllable soft actuators is crucial to the viability of soft robots. Many types of soft actuators already exist, including electrostatic [45, 59, 60], fluidic [25,45], and thermal actuators [130,131]. A unique form of soft actuator is the HASEL (hydraulically amplified self-healing electrostatic) actuator [63, 64] which is based on electrostatic and hydraulic actuation principles. These actuators exhibit similar performance characteristics to mammalian skeletal muscle, a benchmark for soft actuator performance [64].

Previously, a planar HASEL actuator was modeled and controlled in a closed loop system using a high-speed camera and a capacitive self-sensing circuit [91]. However, this research only modeled the frequency response at a single operating voltage. In addition, the planar HASEL actuator was made from a stretchable elastomer and functioned the same way as laterally stretched dielectric elastomer actuators [89]. Higher performance HASEL actuators have now been created using thin-film polymers [64]; compared to elastomer-based HASEL actuators, these do not require prestretch or mounting to rigid components which simplifies their fabrication and decreases overall weight. The shape of the actuators can also be modified for different modes of actuation [88]. As a result, polymer film-based HASEL actuators with closed loop control are more practical for a wide range of applications.

This chapter provides the first example of system identification and closed loop control of

---

[1] The work in this chapter was reprinted with permission, from *Johnson, Brian K., et al. "Identification and control of a nonlinear soft actuator and sensor system." IEEE Robotics and Automation Letters (2020): 3783-3790.* ©2020 IEEE [121]. My contribution to this work is in the design and integration of the capacitive sensor, frequency response modeling and experimentation, feedback controller design, and closed-loop control experimentation. As this is a collaborative work, full acknowledgements of the contributions of all authors are listed at the end of this chapter.

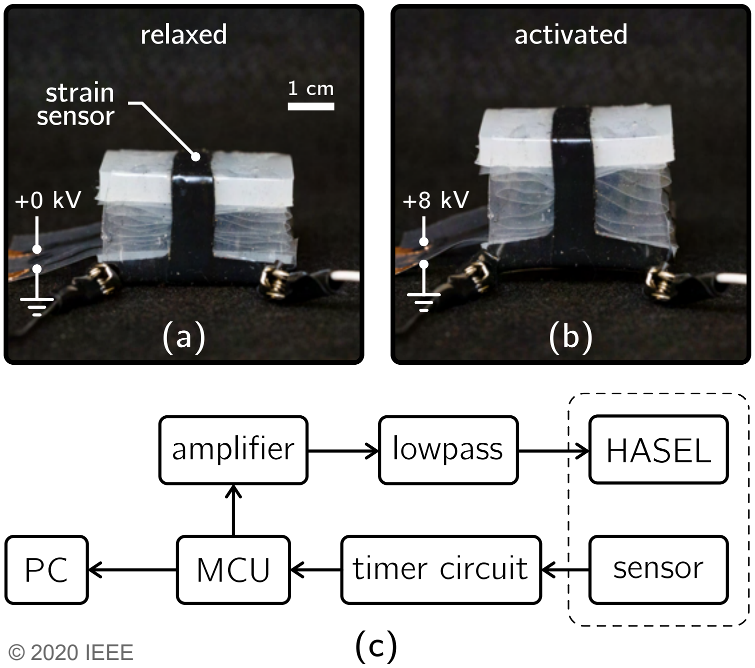

Figure 2.1: **(a)** Relaxed HASEL actuator. The actuator is wrapped with an elastomeric strain sensor, which is shielded from electric fields by dielectric layers. **(b)** Activated HASEL actuator. Applying high voltage across the electrodes causes an increase in actuator stroke. **(c)** Hardware for closed loop control. The output from the strain sensor changes proportional to the increase in stroke and is measured by an LMC555 timer circuit (Fig. 2.2c). The microcontroller unit (MCU) receives measurements from the timer circuit and computes the control output. This is sent to a 5kV/V high voltage amplifier. The amplified voltage is sent to a 500 Hz low pass filter to reduce noise, and is then applied to the HASEL actuator, causing a change in stroke. The MCU also sends data to a computer (PC) to be logged.

HASEL actuators made from thin-film polymers. We describe a technique to model the actuator dynamics as a sum of static and dynamic terms using frequency chirp testing at multiple operating points. This model was used to develop an effective feedback controller for the closed loop system shown in Fig. 2.1.

Although thin-film HASEL actuators are capable of capacitive self-sensing [64], the technique is highly nonlinear and has variable sensor lag, making it unsuitable for high frequency control. It also requires additional hardware to superimpose the multiple AC signals required for self-sensing. We present an external capacitive elastomeric strain sensor with a simple DC circuit that is integrated onto the actuator for close-loop control.

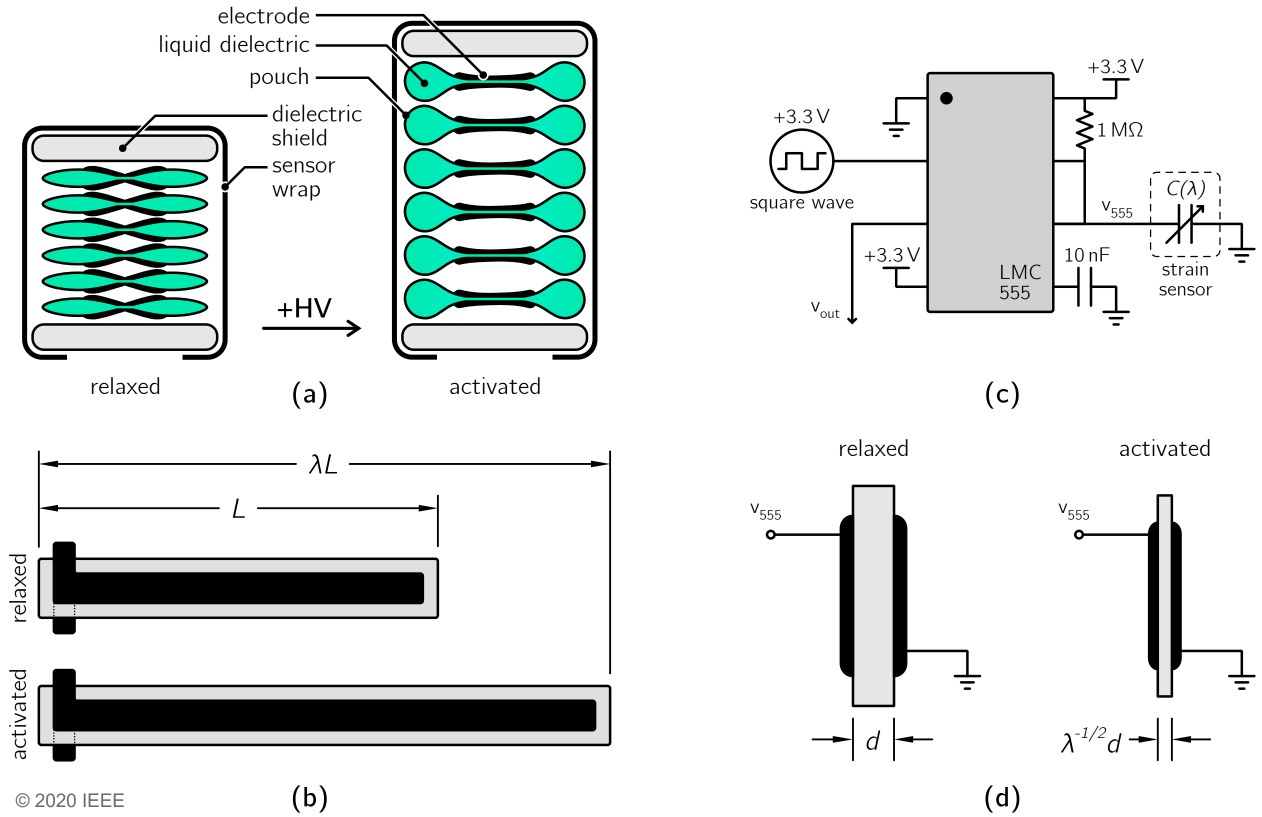

Figure 2.2: **(a)** The foldable HASEL actuator expands upon application of high voltage (HV) to the pouch electrodes. An EcoFlex 00-30 wrap around the outside of the actuator provides a restoring force and contains an integrated strain sensor to measure actuator stroke. Dielectric layers shield the sensor from electric fields generated within the actuator. **(b)** Side view of the foldable HASEL actuator with the sensor wrap attached. Fig. 2.1 also shows this view. **(c)** Circuit design to transduce capacitance change of the sensor to measured actuator stroke. The LMC555 timer runs in a monostable configuration to relate sensor capacitance $C(\lambda)$ to the duty cycle of v_{out}, which is measured by the MCU. **(d)** Sensor electrode cross-section. The change in dielectric thickness d is proportional to the sensor stretch ratio λ and causes the change in capacitance $C(\lambda)$. The left electrode is v_{555} at 3.3 V and the right electrode is ground. The dielectric layer is EcoFlex 00-30. **(e)** The stretch ratio λ of the sensor electrodes is proportional to the sensor capacitance $C(\lambda)$, which is measured through the timer circuit.

2.2 HASEL actuator design and fabrication

The principles of HASEL actuators are well described in previously published works [63, 64, 88]. In summary, HASEL actuators consist of a soft or flexible pouch which is filled with a liquid dielectric. A pair of electrodes are placed on either side of the pouch. When voltage is applied across the electrodes, electrostatic forces displace the liquid dielectric resulting in overall shape change of the pouch. In this work, the pouches are designed to expand linearly when voltage is applied. These pouches are folded and stacked on top of one another to amplify the overall stroke, as shown in Fig. 2.2.

The fabrication of these foldable HASEL actuators is similar to the process described by Mitchell et al. [88]. However, we used a different polymer film for the shell of the actuators. A 20 μm thick polyester (PE) lidding film (L0WS, Multiplastics) was selected because it exhibited less charge retention than biaxially-oriented polypropylene (BOPP) films used in previous works [64,88]. Charge retention in HASEL actuators, which is related to dielectric absorption in film capacitors, results in HASEL actuators exhibiting changes in maximum and minimum stroke over time when a single polarity high voltage (HV) signal is applied. HASEL actuators made with the PE film exhibited less change in stroke than the BOPP films used in Kellaris et al. and Mitchell et al. [64,88]. As a result, we were able to activate HASEL actuators made from PE using a single polarity HV signal which simplified the electronics and controls.

In this work, each stack of foldable HASEL actuators consisted of twelve individual actuators. An actuator consisted of two separate 30 mm x 15 mm pouches, resulting in a 30 mm x 30 mm overall size for an individual actuator. A CNC heat-sealer was made from a commercially available CNC machine (Shapeoko 3 XL, Carbide 3D) fitted with a hot end designed for 3D printers (V6, E3D). The hot end, which consists of a heating element and extruder tip, was mounted to the z-axis of the CNC machine using a spring-loaded fixture that allows for varying the pressure applied by the extruder tip. Temperature of the extruder tip was regulated using a proportional-integral-derivative (PID) controller (ITC-100, Inkbird). The sealing speed was 450 mm/min, temperature was 195 °C, and sealing pressure was approximately 560 kPa. The pouch electrodes were of a conductive carbon ink (CI-2051, Engineered Materials Systems) which was applied using the screen-printing process described by Mitchell et al. [88]. The liquid dielectric used was a vegetable-based transformer oil (Envirotemp FR3, Cargill). As described in Mitchell et al. [88], all twelve actuators were sealed in a single strip. The heat seal pattern included connections between all of the pouches so that all actuators could be simultaneously filled with liquid dielectric. Each actuator consisted of two pouches with 0.38 mL volume of liquid dielectric in in each pouch. After filling, the actuators were then folded in an accordian pattern and two small slivers of transfer tape (924, Scotch) were placed on the shell of each actuator to hold the stack together.

To insulate the actuator and mitigate the electric field effects caused by exciting the actuator, we created a silicone rubber dielectric shield. The actuator was sandwiched between two 5 mm-thick blocks of DragonSkin 30 (Smooth-On), covering the top and bottom of the actuator as shown in Fig. 2.2.

An elastomeric skin was wrapped around the outside perimeter of the dielectric shield. When the actuator stroke increases, the wrap stretches and provides a restorative force to return the actuator to the undeformed state when voltage is removed. The wrap is made of EcoFlex 00-30 (Smooth-On), which is another silicone-based elastomer that exhibits low stress relaxation and good cyclic loading properties [132]. No viscoelastic effects were observed. Additionally, the system identification includes the dynamics of this wrap. The elastomeric strain sensor shown in Fig. 2.1, described in Section III, is incorporated into this wrap.

2.3 HASEL actuator strain sensing

2.3.1 Design of a capacitive elastomeric strain sensor

We created a capacitive strain sensor to measure the stroke of the foldable HASEL actuator and close the loop on the actuator system. The design of the capacitive elastomeric sensor we describe is similar to others used throughout soft robotics [133–135].

The sensor is comprised of two elastomer electrodes with a dielectric material between them, forming a parallel plate capacitor. The dielectric in this sensor is an incompressible elastomer: when the sensor is uniaxially strained, the thickness of the dielectric layer decreases. Using the parallel plate capacitor equation and the fact that the material is incompressible, the change in capacitance of the strained sensor ΔC can be written in terms of only the stretch ratio λ, which is the ratio of stretched length over original length:

$$\Delta C = \frac{\varepsilon_0 \varepsilon \Delta A}{\Delta d} = \frac{\lambda \varepsilon_0 \varepsilon A}{d} = \lambda C_o \tag{2.1}$$

where C_o is the pre-strained sensor capacitance, A the original area of the electrodes, d the original distance between electrodes, ε_0 the vacuum permittivity, and ε the dielectric permittivity. The change in capacitance is thus directly proportional to the strain of the sensor.

Since the actuator was already wrapped in Ecoflex 00-30, which is a commonly used sensor dielectric [135], we used the actuator wrap as the dielectric layer for the sensor. This allowed us to relate the change in stroke of the actuator to a change in total capacitance C as the wrap (and sensor) is stretched by a ratio λ. This relationship is shown in Fig. 2.2.b.

We manufactured conductive electrodes for the sensor in a similar manner to other conductive polymers [135]. We mixed EcoFlex 00-30 with 9 w.t.% carbon black powder (VULCAN-72, Cabot Corp) and 51 w.t.% iso-octane (Sigma Aldrich), which acted as the solvent. To create a degassed, homogeneous mixture, we added 1/4" ball bearings into the mixture container before placing the container in a planetary mixer (ARV-310, Thinky) for seven minutes. The mixer first created a vaccuum during the preliminary mixing stage, then gradually increased the mixing speed from 500 rpm to 1750 rpm. We then blade-casted (ZAA 2300, Zehntner) the mixture onto a 500 μm-thick layer of EcoFlex 00-30 and placed the thin layer into an oven at 70°C. Once fully cured, the electrodes were laser cut out of the conductive EcoFlex 00-30 sheet and placed on both sides of the dielectric EcoFlex 00-30 layer. Uncured EcoFlex 00-30 was painted over the electrodes to bind the electrodes to the dielectric layer. The total thickness of the sensor was about 800 μm.

An LMC555 timer circuit was used to transduce the capacitance change ΔC into a change in DC voltage, as shown in Fig. 2.2c. The LMC555 runs in a monostable configuration, where the duty cycle of the output v_{out} is a function of the capacitor $C(\lambda)$ in the circuit. We used an ARM-based microcontroller unit (MCU) (Teensy 3.6, PJRC) to generate the input signal to the LMC555 at a frequency of 4500 Hz and duty cycle of 89.9%. The MCU measured the rising and falling edges of the output via interrupts, and from the elapsed time between rising and falling edge it transduced the capacitance change.

2.3.2 Experimental verification of strain sensor measurements

We tested the elastomeric strain sensor to validate its use in our closed loop system. The same experimental setup used to identify the foldable HASEL actuator model described in Section IIB, with the addition of sensor circuitry, was used to determine the sensor model. The sensor was wrapped around the actuator and the dielectric shields, and the sensor electrodes were connected according to the circuit shown in Fig. 2.2c.

In the experiment, we sent a set of step inputs – 2, 3, 4, 5, 6, and 7 kV – to the actuator via the high voltage amplifier. The laser then captured the corresponding stroke. The analog voltage

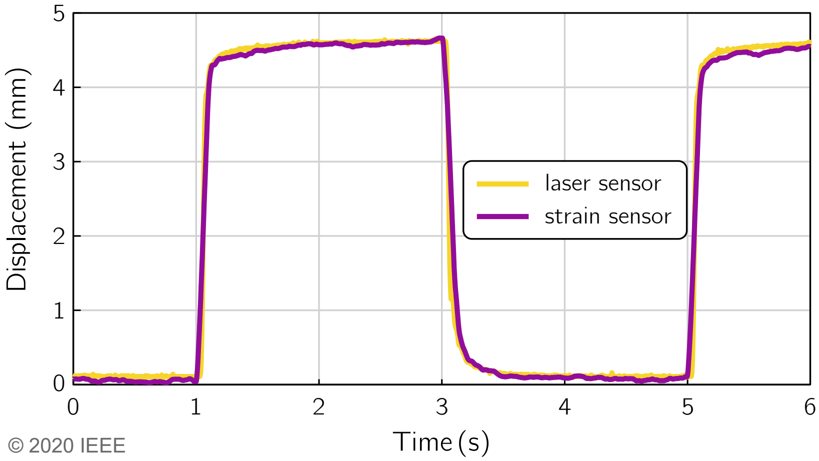

Figure 2.3: Strain sensor response to an open loop actuator step input from 0 to 6 kV. The strain sensor measurement was filtered with a 40 Hz second order low pass filter to reduce noise. It is plotted alongside the measurement from the laser position sensor, which is considered the ground truth for the HASEL actuator stroke. The strain sensor has less than 5% error compared to the laser and is fast enough to capture the step response dynamics. The open loop step responses also show that the HASEL actuator has two response modes: a fast activation for positive steps (t = 1 s) and a more damped relaxation for negative steps (t = 3 s).

outputs of both the sensor and the laser were read by the MCU via a 12 bit ADC and then logged by the computer via serial connection. The sensor measurement was digitally filtered using a second order low pass filter with a cutoff frequency of 40 Hz to reduce noise. The data from one step test are shown in Fig. 2.3. The results show that the strain sensor has an error less than 5% in steady state and has a high signal-to-noise ratio for closed loop control. The results also highlight that the foldable HASEL actuator responds different to negative step inputs than positive step inputs; this is discussed further in Section V.A.

2.4 Integration and system identification

A planar HASEL actuator is a nonlinear time-varying (NLTV) system [83]. We similarly expect foldable HASEL actuators to be NLTV systems, with a single input single output (SISO) relationship between an applied voltage v and the resulting stroke z represented as

$$z = h\left(v\left(t\right), t\right), \tag{2.2}$$

where h is some unknown nonlinear function and t is time. In this paper, we make several assumptions which enable us to approximate the dynamics of a foldable HASEL actuator with a linear time-invariant (LTI) model.

As described in Section II.A, the HASEL actuator is time-varying due to the effects of charge retention. However, we found that the change in stroke due to charge retention was less than 5% during any 180 s duration of any applied voltage between 0-9 kV. We decided to consequently treat the system as time-invariant within time scales of 180 s. Note that although the real system is slowly time-varying, closed loop control will allow us to counteract the effects of charge retention using integral control. Since we treat the system as time invariant, (2.2) becomes:

$$z = h\left(v\left(t\right)\right) \text{ assuming } t \leq 180\ s. \tag{2.3}$$

A traditional frequency domain analysis technique [136] is used to experimentally determine a model for foldable HASEL actuators. Typically, these methods utilize zero-mean input signals (e.g. sinusoids) over a range of frequencies so that the system only responds in its dynamic modes. However, a zero-mean signal is not realizable in our system because the actuator stroke is strictly positive. To circumvent this, the system input is calculated using

$$v(t) = v_s + v_d\left(t\right), \tag{2.4}$$

a combination of v_s, a static DC offset voltage, and v_d, a dynamic zero-mean test signal.

Our test signal is a chirp signal, defined as a function of amplitude A (kV), time t (s), and a variable frequency $f(t)$ (Hz):

$$v_d\left(t\right) = A \sin\left(2\pi f\left(t\right) t\right). \tag{2.5}$$

A linear chirp is used in which the frequency increases linearly as a function of time. The equation for $f(t)$ is

$$f(t) = \Big(\frac{f_f - f_o}{t_{tot}}\Big) t \tag{2.6}$$

where f_o is the start frequency (Hz), f_f is the end frequency (Hz), and t_{tot} is the total test duration (s).

The actuator input is thus a superposition of a step input (the v_s term) and a linear chirp input (the v_d term). We assume the system response stroke z can be similarly separated:

$$z(t) = z_s + z_d(t), \tag{2.7}$$

where the static term z_s only depends on v_s:

$$z_s = h_s(v_s), \tag{2.8}$$

and the dynamic response term z_d depends on some unknown combination of both the static input v_s and the dynamic input v_d:

$$z_d(t) = h_d(v_s, v_d(t)). \tag{2.9}$$

To determine the influence of the static input on the dynamic response, we performed frequency response testing using an identical dynamic input v_d at a variety of operating points v_s. This provided a set of responses:

$$\begin{aligned} z_1(t) &= h_s\left(v_{(s,1)}\right) + h_d\left(v_{(s,1)}, v_d(t)\right) \\ z_2(t) &= h_s\left(v_{(s,2)}\right) + h_d\left(v_{(s,2)}, v_d(t)\right) \\ &\vdots \\ z_n(t) &= h_s\left(v_{(s,n)}\right) + h_d\left(v_{(s,n)}, v_d(t)\right). \end{aligned} \tag{2.10}$$

Subtracting the static $z_{(s,i)}$ term from each response z_i isolates the dynamic responses z_d:

$$\begin{aligned} z_{(d,1)}(t) &= h_d\left(v_{(s,1)}, v_d(t)\right) \\ z_{(d,2)}(t) &= h_d\left(v_{(s,2)}, v_d(t)\right) \\ &\vdots \\ z_{(d,n)}(t) &= h_d\left(v_{(s,n)}, v_d(t)\right). \end{aligned} \tag{2.11}$$

The equivalence of each dynamic response $z_{(d,i)}$ despite variations in their respective static inputs $v_{(s,i)}$, would imply that z_d is fully independent of v_s, and is only a function of the dynamic input v_d. We expect that this also holds for approximation:

$$\begin{gathered} z_{(d,1)}\left(t\right) \simeq z_{(d,2)}\left(t\right) \simeq \cdots \simeq z_{(d,n)}\left(t\right) \\ \Rightarrow z_d\left(t\right) \simeq h_d\left(v_d\left(t\right)\right). \end{gathered} \tag{2.12}$$

The results described in Section II.B.2 and shown in Fig. 2.4 suggest that v_s indeed has a negligible effect on z_d in the 2-7 kV range, and justify the simplification of our model to the form:

$$z\left(t\right) = h_s\left(v_s\right) + h_d\left(v_d\left(t\right)\right). \tag{2.13}$$

In summary, the output stroke of the actuator $z(t)$ is a superposition of the static input response h_s and the dynamic chirp response h_d.

Experimental setup and test parameters

We experimentally determined the foldable HASEL actuator model using a data acquisition system (DAQ) (NI 6212, National Instruments), a 5kV/V high voltage amplifier (Trek Model 50/12, TREK), laser position sensor (LK-H157, Keyence), and a processing script in MATLAB 2019a (MathWorks). Each input signal from (2.4) was created in MATLAB and sent to the DAQ, which then forwarded the voltage signal to the amplifier. The amplifier applied the high voltage to the actuator, while the laser simultaneously measured the stroke of the top of the actuator. The DAQ returned laser voltage and amplifier voltage to MATLAB.

The form of the input signals was the same as (2.4) and (2.5) with signal characteristics are given in Table 2.1. The sample rate for all tests was 10 kHz. The foldable HASEL actuators were characterized using only the elastomeric skin wrapped around the actuator without the dielectric shield included. This was done to create a general model for foldable HASEL actuators that is not dependent on the dielectric shield thickness or material. We separately tested the system including the dielectric shields and observed negligible changes in the frequency response because the mass added by the dielectric layer is minimal.

Our system operating points V_s were 2, 3, 4, 5, 6, and 7 kV, as listed in Table 2.1. The end frequency was selected at 20 Hz. We observed a drastic decrease in stroke amplitude when the input frequency was greater than 20 Hz so we constrained our analysis up to this limit.

The chirp signal was repeated consecutively for a total of three chirps over 60 s. The goal of the repeated chirps was to account for any effects of charge accumulation; a single 20 s chirp began with low charge accumulation at the start frequency f_0 and greater accumulation near the end of the chirp at f_f. Repeating the chirp allowed us to analyze the low frequency response at higher levels of charge accumulation.

To verify the consistency of the actuator dynamics between actuator copies, we completed one test at each operating point on three similarly-constructed foldable HASEL actuators for a total of 18 tests. Before performing each chirp test, we input a negative 1 kV constant voltage through the HASEL actuator to reverse any accumulated charge from previous tests.

Data processing

After performing these frequency response tests, we processed the amplifier voltage and laser position data in MATLAB. To obtain frequency response data, we took the Fast Fourier Transform (FFT) of both the input (amplifier voltage) and output (laser position measure) using MATLAB's 'fft' function. Dividing the output FFT by the input FFT and then taking the magnitude and phase of the resultant in the real/imaginary plane yielded the complete frequency response of the system.

2.5 Closed loop controller

2.5.1 Hardware for closed loop control

We closed the loop around a foldable HASEL actuator using the hardware outlined in Fig. 2.1: an ARM-based MCU (Teensy 3.6, PJRC), a sensor, a low pass filter, a high voltage amplifier, and a foldable HASEL actuator.

The sensor generates a voltage proportional to the HASEL actuator stroke, which is read by the MCU via its onboard 12 bit ADC. The sensor reading is digitally filtered in the MCU using a 40

Table 2.1: Chirp signal test parameters. ©2020 IEEE

V_s (kV)	A (kV)	f_o (Hz)	f_f (Hz)	t_{tot} (sec)
{2, 3, 4, 5, 6, 7}	1	0.001	20	20

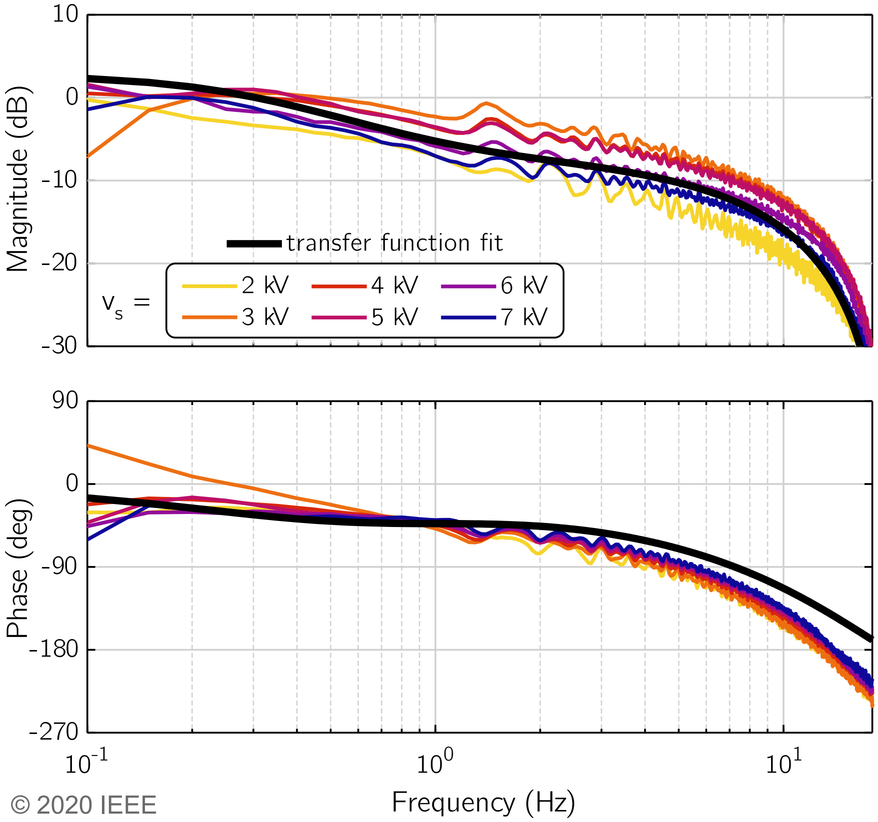

Figure 2.4: Bode plot set for a foldable HASEL actuator with elastomeric restoring wrap. Each curve shows the frequency response at 2, 3, 4, 5, 6, and 7 kV static offsets. The offset voltage has negligible effects on the dynamic response between curves. The estimated transfer function fit for this set of curves is also plotted using Eq. (2.17).

Hz second order low pass filter to reduce noise, and the filtered signal is then applied to the control algorithm, which will be discussed in Section IV.B. Based on the controller, a desired command voltage is computed and output from the MCU using a built-in DAC. The analog output voltage is then amplified by 5 kV/V. The amplified voltage signal is passed through an analog 500 Hz second order low pass filter to reduce high voltage ripples and is then applied to the HASEL actuator. As the HASEL actuator deforms, the sensor reading changes, and the command voltage updates. The overall frequency of the closed loop system is 200 Hz.

We first used the laser position sensor as the feedback sensor for closed loop control. The laser exhibits full linearity to within 16 μm throughout its full sensing range, a repeatability of 0.25 μm, and a sampling rate of over 100 kHz: it can therefore accurately and precisely track a 20 Hz system and thus provided a baseline closed loop result to easily fine-tune the controller. After performing closed loop tests with the laser position sensor, we switched the sensor to the integrated strain sensor described in Section III. We then compared the closed loop control results from both sensing methods.

The laser sensor circuit output a voltage proportional to the sensed actuator stroke with a range of 0-3.3 V. The analog sensor signal was converted to a 12 bit integer by the MCU ADC, which was converted into an estimated stroke measurement in mm for the control algorithm. For the laser we used the manufacturer's software (LK-Navigator 2, Keyence) to set this conversion rate to 3 mm/V (e.g. the laser will output 3 V for an actuator stroke of 9 mm). On the other hand, the capacitance change of the strain sensor corresponds to a change in the duty cycle of the LMC555 timer's output. Two hardware interrupt pins on the MCU were programmed to compute the elapsed time between the falling edge and the rising edge of the LMC555's 4.5 kHz square wave output. The elapsed time, which were directly proportional to the actuator's stroke, was then calibrated using the laser position sensor as ground truth. To map the elapsed time to the displacement, we measured the laser position data and elapsed time at 1 mm step increments from 2-7 mm to determined the line of best fit, relating the strain sensor data to laser position sensor data.

2.5.2 Controller design and closed loop simulation

As shown in Fig. 2.3, the actuator behaves differently in an activation (increasing voltage) than relaxation (decreasing voltage) response; we discuss this further in Section V.A. To account for these differences we chose to implement a dual-mode system for feedback control. The block diagram of this dual-mode system is shown in Fig. 2.5. Reference r is our commanded actuator stroke in mm, which is compared to our sensor measurement $\hat{z}$ and used to calculate error $e = r - \hat{z}$. When $e \geq 0$, the actuator must activate to reach reference position r. When $e < 0$, the actuator must relax to reach r.

To control each response, separate controllers C_+ and C_- were created. We first assumed both controllers to be the same and used the basic form of PID control. The C_+ controller was tuned using a Simulink simulation based on the block diagram in Fig. 2.5 and the foldable HASEL actuator model we derived shown in (2.17). We optimized the gains for a fast rise time at the cost of some overshoot. Although the derivative gain is small, we observed an improved overshoot compared to just employing PI control. We then adjusted the C_- controller to achieve the desired step response for HASEL actuator relaxation. Since the relaxation is more damped, C_- is more

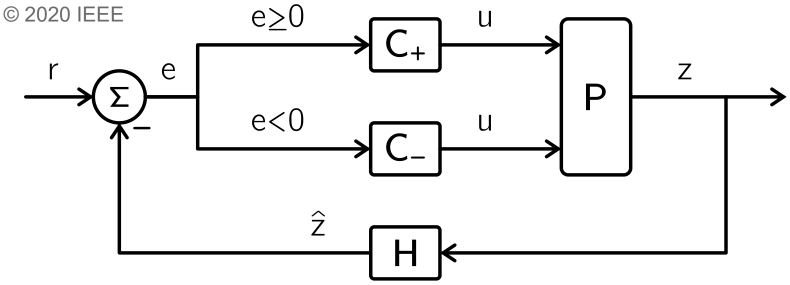

Figure 2.5: A dual-mode controller allows separate control of the activation and relaxation responses of the foldable HASEL actuator (plant P). Reference r is the commanded actuator stroke (mm), $\hat{z}$ is the estimated sensor measurement (mm) based on actual stroke z (mm), and u is the control output. The gains of the control switch based on the sign of the error $e = r - \hat{z}$; C_+ is used for $e \geq 0$ and C_- is used for $e < 0$. H represents the sensor used in closed loop control; we performed closed loop control using both a laser position sensor and the integrated strain sensor.

aggressive than C_+ in order to achieve a faster rise time than the open loop. The final transfer functions for both controllers are given as:

$$C_+(s) = 1.15 + \frac{25}{s} + (1.74 \times 10^{-5})s \tag{2.14}$$

$$C_-(s) = 1.25 + \frac{26}{s} + (3.2 \times 10^{-5})s. \tag{2.15}$$

These were converted to the discrete-time domain by applying the trapezoidal rule on the integral term and the backward rectangular rule on the derivative term, using a time step of 0.005 s (200 Hz closed loop frequency). Taking the inverse z-transform yielded difference equations which we implemented directly on the MCU using Arduino IDE.

2.5.3 Closed loop experimental validation

To validate our actuator model and controller design, we performed real-time closed loop experiments on the foldable HASEL actuator. Using the test setup described in Section IV.A, shown in Fig. 2.1, we performed a series of step input tests.

We tested the step response of the actuator for both positive and negative steps to see the effects of both controllers C_+ and C_-. We expect that the more aggressively designed C_- controller will increase the rise time of the negative step response in comparison to the open loop.

We ran a sequence of positive steps and then negative steps in consecutive order. We ran these tests both for closed loop control using the laser position sensor and for closed loop control using the integrated strain sensor. The sequence of stroke commands was as follows (all values in mm):

$$2 \rightarrow 4 \rightarrow 6 \rightarrow 4 \rightarrow 2. \tag{2.16}$$

The strokes were kept between 2 and 6 mm to avoid saturation of the amplifier voltage. We set a limit of 9 kV on the voltage in order to prevent dielectric breakdown in the actuator, which may occur in voltages above 9 kV.

In addition, we repeated these steps under strain sensor control while the actuator lifted a 25.5 g load. This load is 64.7% of the total actuator mass of 39.4 g (including dielectric shields). This was done to demonstrate that the closed loop system can perform work on external loads. The results from all tests are listed in Table 2.2 and discussed in Section V.B.

2.6 Results and discussion

2.6.1 Foldable HASEL actuator model

From the frequency response data shown in Fig. 2.4, we found an anti-resonance at 19.45 Hz and associated drop in phase. Although the physical cause of this is unknown, we determined that a notch filter was a good first approximation. From there, we used a combination of the MATLAB System Identification Toolbox and manual pole/zero placement to arrive at a model for foldable HASEL actuators.

As described in Section II.B.1, we observed that the actuator had a more damped step response in relaxation (removal of voltage across the actuator) than in activation (application of voltage). This behavior is shown in Fig. 2.3. The two modes are likely caused by the driving actuation mechanism within HASEL actuators [64]. The actuator expands when dielectric fluid is displaced by electrodes zipping together, which is a fast process. The actuator contracts only when the dielectric fluid returns to its original location, but without the active force of the zipping electrodes this takes additional time, causing a slower step response in relaxation. However, the two modes are not significantly different, so we modeled the actuator as a single plant transfer function; our dual-mode controller design discussed in Section IV.B accounts for any differences from our model.

The resulting foldable HASEL actuator transfer function is:

$$P(s) = \frac{K(s+50.27)(s+62.83)(s+628.3)(s^2+\omega^2)}{(s+18.85)(s+56.55)(s^2+230s+\omega^2)^2}, \tag{2.17}$$

$$where\ K = 10.836,\ \omega = 122.2 rad/s.$$

This transfer function maps the actuator input voltage (kV) to an output stroke (mm). The fit of this model is plotted against the frequency response data in Fig. 2.4.

The data we collected support our conclusion that foldable HASEL actuator responses can be approximated as a sum of independent static and dynamic response components. Although there is not a complete separation of static and dynamic responses, this modeling technique was successful in predicting the actuator dynamics.

2.6.2 Closed loop control

closed loop step responses using the laser position sensor show a faster rise time for both activation and relaxation compared to the open loop responses shown in Fig. 2.5. The results of both series of tests are summarized in Table 2.2 and shown in Fig. 2.6. The values in Table 2.2 represent the best achieved from each test, prioritizing a fast rise time. The results of closed loop control with the integrated strain sensor show a fast rise time of 0.029 s and 0.07 s for a positive and negative step input, respectfully. These times are 16% slower and 71% faster, respectfully, to those achieved using the laser sensor in closed loop control. It is not expected that the closed loop performance using the strain sensor is better than that achieved with the laser sensor; any improved performance is likely due to variability in the physical system and noise.

We found that despite an increase in signal noise, the strain sensor could track actuator strokes as small as 0.1 mm and at frequencies up to 20 Hz. In addition, there was no significant sensor drift over time; the conversion from bits to mm described in Section 1.0.4 remained constant throughout our testing.

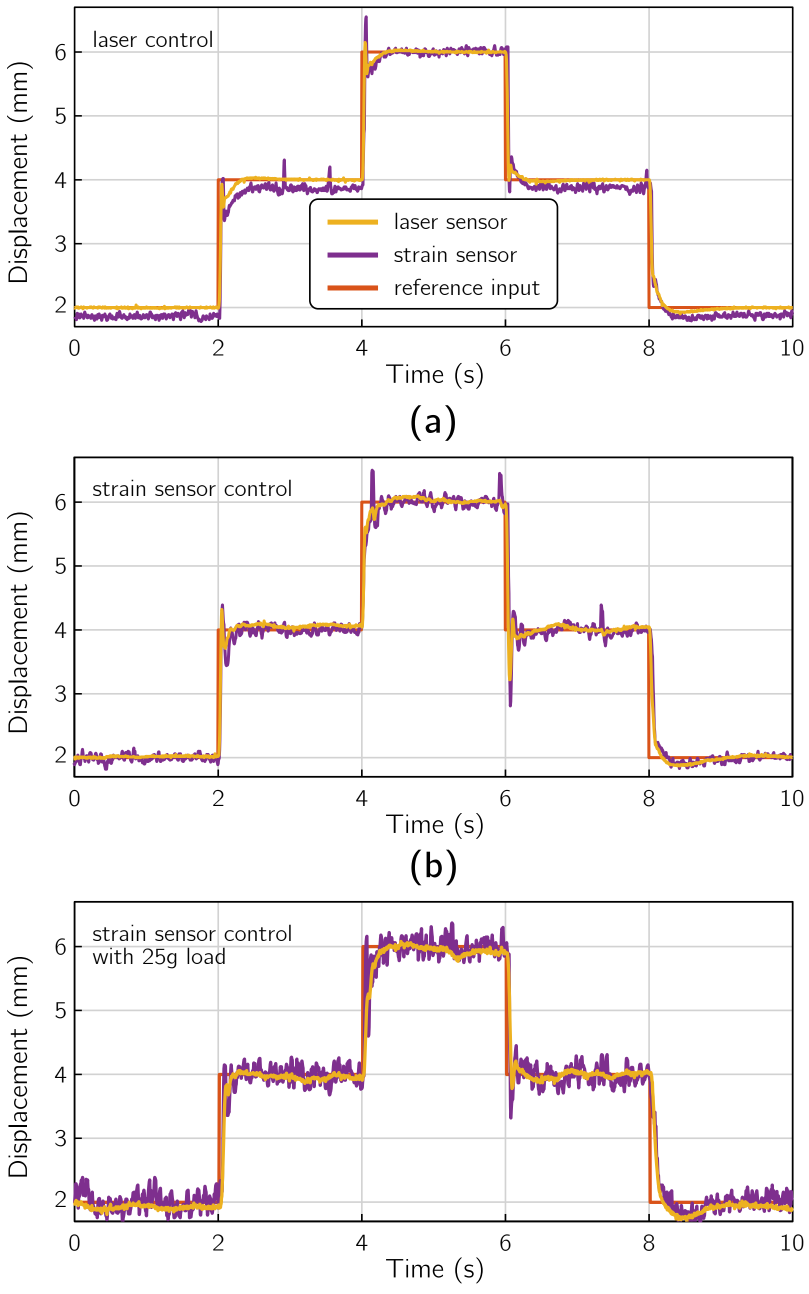

(a)

(b)

(c)

Figure 2.6: **(a)** closed loop responses using the laser position sensor. The first two steps show control of the activation actuator dynamics, while the second two steps show control of the relaxation dynamics. The step response is faster than the open loop, and the more aggressive C_- controller for the relaxation response significantly reduced the rise time. Small nonlinearities in the strain sensor calibration resulted in a measurement offset at 2 and 4 mm displacement, though the error remains under 5%. **(b)** closed loop responses using the integrated strain sensor. Closed loop control using the strain sensor had a higher overshoot and larger settling time compared to the laser position sensor, but still achieved a faster rise time than the open loop. **(c)** closed loop response using the integrated strain sensor under a 25.5 g load, which is 64.7% of the total actuator weight. Under load, closed loop control was similarly fast.

Table 2.2: Closed loop test results. ©2020 IEEE

HASEL mode	*Closed loop test*	*10-90% Rise time (s)*	*5% Settling time (s)*	*Overshoot (%)*
Activation	open loop	0.13	0.11	0
	Laser	0.026	0.185	6.0
	Strain Sensor	0.029	0.14	16.0
	25.5 g Load	0.025	0.23	0
Relaxation	open loop	0.165	0.275	0
	Laser	0.12	0.17	0
	Strain Sensor	0.071	0.67	5.5
	25.5 g Load	0.12	0.17	0

2.7 Strain sensor denoising

As discussed, the strain sensor used in this work suffered from significant noise which impacted its performance compared to the laser sensor. One significant result of integrating the sensor around the actuator is that the sensor electrodes are subjected to high electric fields due to the voltages used in the HASEL actuator. This was found to significantly increase the noise level of the sensor compared to when it was physically separated from the area of greatest electric field. The dielectric shields and the 40 Hz low pass filter helped reduce this noise, but it was not eliminated completely. Another small contributor of noise could be via small vibrations of the actuator which we observed in the laser sensor measurements.

However, it may be possible to improve the sensor and feedback loop via real-time signal processing. One approach could be to add a Kalman filter since the majority of the noise appears to be Gaussian. Other approaches such as real-time wavelet denoising [137] may help eliminate noise without introducing significant phase lag, as is the case with low-pass filters. As exploratory work, we implemented a real-time wavelet filter on the microcontroller.

The filter takes 16 sample segments and performs a discrete wavelet transform to 4 compression levels. For each compression level, approximate and detail coefficients are calculated using a Haar wavelet [138]. A threshold of 0 is used to denoise the approximate coefficients. The signal is then reconstructed from the thresholded approximate and detail coefficients. To improve edge performance, the 16 sample signal is mirror padded. For example, at time step k, the filter segment of signal $u[k]$ takes the form

$$\{u[k-15], ..., u[k-1], u[k], u[k], u[k-1], ..., u[k-15]\}. \quad (2.18)$$

The discrete wavelet filter was implemented at 1 kHz on the MCU using the output of the 555 timer circuit as $u[k]$. Preliminary results show that the wavelet filter has slightly improved performance when compared to 1st- or 2nd-order low pass filters. However, we leave the quantitative analysis and design improvements of the filter to future work.

In addition to signal processing strategies, we also explored approaches to electrical shielding in an effort to reduce the electromagnetic interference on the capacitive sensor. The first approach is the application of a grounded shield (braided mesh or aluminum foil) which encapsulates the sensor circuit and the wires connecting the circuit to the sensor itself. This reduces some of the coupling effects caused by the electromagnetic noise, but it is not eliminated.

The primary source of coupling occurs between the HASEL actuator electrode and the sensor electrodes; however, since the sensor must be compliant to stretch with the actuator, traditional shielding is insufficient. One approach may be to modify the layout of the sensor electrodes to either (a) reduce coupling, or (b) shield from the effects of coupling using a grounded electrode. Fig. 2.7 shows some proposed sensor electrode topologies which may address these challenges. In addition to alternate electrode layouts, it may be possible to improve sensor performance by improving the design of the LMC555 circuit. Buffer op-amps could be placed throughout the circuit to eliminate impedance problems. Differential signaling could also be used to subtract out any noise added to the signal measurement. However, we leave it as future work to evaluate the effectiveness of these approaches.

2.8 Conclusions

Our work has shown that nonlinear foldable HASEL actuators can be modeled using simple linear frequency response tests. We have demonstrated that the dynamic response of the actuator is approximately separate from their static response, and that the dynamics are consistent between copies of actuators.

Using this model, we designed a dual-mode PID controller for real-time closed loop feedback control. We achieved this using an elastomeric strain sensor integrated onto the actuator and

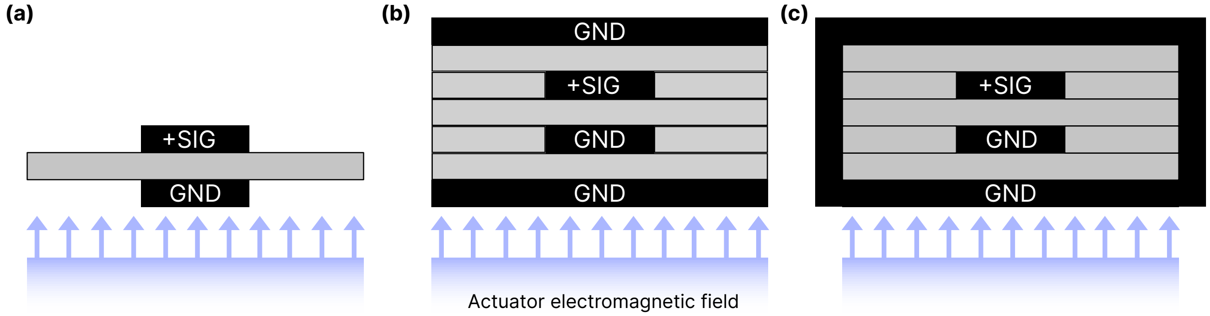

Figure 2.7: **(a)** Original sensor layers from this work with a single ground (GND) and signal (SIG) electrode and a layer of Ecoflex 00-30 between them. The interaction with the electromagnetic field of the HASEL actuators induces noise on the SIG electrode. **(b)** Alternate layout which adds large, grounded electrode shields on the top and bottom of the sensor. **(c)** Alternate layout which fully encloses the capacitive sensor in a grounded electrode, similar to a coaxial cable design. This may be the most robust layout because the external shield can prevent electromagnetic flux from entering the SIG electrode in any direction. All (a), (b), and (c) layouts use the same materials described in Section 2.3.1.

benchmarked these results with closed loop control using a laser position sensor. In both cases, we achieved step responses with faster rise times and settling times compared to the open loop, shown in Table 2.2. We also achieved closed loop control while under a 25.5 g load, equal to 64.7% the total mass of the actuator, which shows that this system can perform useful work.

Using this actuator model and dual-mode controller, more complex robotic systems driven by foldable HASEL actuators may be controlled. The system identification techniques we utilized may also be applied to other nonlinear soft actuators.

Lastly, we discussed approaches to reduce noise for sensors integrated with HASEL actuators. Both hardware- and software-based solutions show promise, but an in-depth analysis is left for future work.

2.9 Acknowledgements and contributions

As the work presented in this chapter is the result of collaboration with multiple researchers, here I describe the contributions of each team member for clarity. The conceptualization of this work was done by myself, Mark E. Rentschler, Vani Sundaram, Sean Humbert, and Mantas Naris. The capacitive sensor material selection was performed by Eric Acome. The dielectric block for sensor shielding was conceptualized and designed by Vani Sundaram. The dynamic modeling at multiple static offset voltages was conceptualized by Sean Humbert and myself. The mathematical model of separate static and dynamic responses was developed by myself and Mantas Naris. The folded HASEL actuator design and material selection was performed by Eric Acome. Software for closed-loop control was written by Khoi Ly, myself, and Vani Sundaram. The microcontroller pinout and low pass filter were designed by Khoi Ly. Data collection was performed by myself and Vani Sundaram. The dual mode control scheme was conceptualized by Mantas Naris and myself. The control design and tuning was performed by myself and Vani Sundaram. Figure visualizations were created by Mantas Naris, myself, and Vani Sundaram.

In addition to the above, I performed the system identification based on the frequency response data, design and implementation of the capacitive sensor, design of the capacitive sensing circuit, modeling of the sensor capacitance to strain relationship, and design of the wavelet denoising technique and electrical circuit shielding.

Chapter 3

Multi-HASEL actuator system development through magnetic sensing[2]

3.1 Introduction

Chapter 2 described the development and control of a single electrostatic actuator/sensor system. However, most robot applications require multiple degrees of freedom which necessitates additional actuators and sensors. This chapter describes technology developments which enable the creation of robots driven by several HASEL actuators simultaneously and how those technologies can create scalable and modular HASEL actuator systems.

Due to the deformable and compliant nature of soft actuators, state estimation using embedded sensing has been an ongoing challenge [121, 139, 140]. For example, the soft strain sensor that was used in Chapter 2 is prone to electric field noise generated by the electrostatic actuators and is vulnerable to high voltage arcing. While it was usable for a single HASEL actuator, the electric field coupling renders it incapable of accurate sensing in the presence of multiple HASEL actuators. This motivated the development of a more robust soft sensing method for HASEL actuator arrays.

In particular, magnetic-based sensing is enticing for robotic systems that require highly accurate and fast sensor information [141]. Magnetic field sensing has been used as a basis for several soft robot feedback sensors in literature [142–152]. This led to the development of a soft magnetic sensor system by Sundaram et al. for use with electrostatic drivers like HASEL actuators [153].

---

[2] The work in this chapter was presented in *Sundaram, Vani, Ly, Khoi, Johnson, Brian K., et al. "Embedded Magnetic Sensing for Feedback Control of Soft HASEL Actuators," accepted to IEEE Transactions on Robotics, 2022.* I refer only to the portions of this work in which I made a contribution and to the portions which provide relevant background information. My contributions are in the system identification techniques, kinematic control system, and kinematic closed-loop experimentation. As this is a collaborative work, full acknowledgements of the contributions of all authors are listed at the end of this chapter.

The magnetic sensor relates a change in actuator stroke to a change in magnetic flux density using a soft magnetized block for each actuator and measured by a local magnetometer.

In this chapter we use techniques from Chapter 2 to create a closed loop HASEL actuator height controller using the magnetic sensor of Sundarem et al. [153], and demonstrate an application of this magnetic sensing approach by precisely controlling the end effector of a HASEL-actuator-driven robotic platform (referred to as the deformable platform, shown in Fig. 3.2(b)-(c)). Acknowledging that the magnetic sensing mechanism is a two-part mechanism requiring a magnetometer and a magnetic block, we refer to this combined mechanism as the sensor. We also refer to the combination of the sensor with a folded HASEL actuator as a unit.

3.2 Magnetic sensing hardware

3.2.1 Magnetic sensing circuit

In Sundaram et al. a low cost, off-the-shelf 3-axis magnetometer (LIS3MDL, ST Electronics) on a breakout board (LIS3MDL Carrier, Pololu) was used to sense the change of the magnetic flux density of a moving magnetic block [153]. The magnetic block is a 50 mm x 50 mm x 5 mm soft permanent magnet made by mixing silicone (Ecoflex 00-30, Smooth On) with neo-powder (NQP-B+ 20441, Neo Magnequench) cured into a north-south alignment. A microcontroller unit, or MCU (Teensy 3.6, PJRC), receives digital data of the raw magnetic flux density from the sensor via a four-wire SPI communication protocol at a selectable resolution, range, and sampling rate up to 1 kHz. The magnetic block covers the top of a HASEL actuator, and both are placed on top of the magnetometer (Fig. 3.2(a)). This configuration allowed Sundaram et al. to measure the change in magnetic flux density as the distance between the block and the sensor varies due to the displacement of the actuator [153]. To simplify the sensing problem, the x- and y- sensing axes of the magnetometer were disabled, and only the z-axis, which is parallel to the direction of travel of the magnetic block, was used.

Folded HASEL actuator

The method of creating the folded HASEL actuators in this section is the same as described in Chapter 2. However, the vegetable-based dielectric liquid was replaced with a silicone liquid dielectric (PSF-5cSt, Clearco). The lower viscosity dielectric liquid was used to improve the rise and fall times of the actuator compared to the previous folded HASEL actuator.

3.3 Sensing range, resolution, and validation

3.3.1 Characterization and mapping of the sensor

Sundaram et al. conducted a set of trials to map the magnetic flux density registered by the magnetometer to the change of distance of the magnetic block [153]. The resulting polynomial map was:

$$d_{map} = p_3 B_z^3 + p_2 B_z^2 + p_1 B_z + p_0 \tag{3.1}$$

$$p_3 = 9.332\text{x}10^{-10}, \qquad p_2 = 10.41\text{x}10^{-5}, \qquad p_1 = -0.044, \qquad p_0 = 85.618$$

where d_{map} is the displacement of the block relative to the magnetometer in mm and B_z is the change in magnetic flux density along the z-axis in mG.

Since HASEL actuators operate under low current (in the milliampere-range [88]), we expect the sensor to be unaffected by the actuators current-induced magnetic field. With the actuator placed in between the magnetometer and magnetic block, an input voltage was fed to the actuator and the corresponding change in height of the block was registered by the sensor. The sensor was able to track the folded HASEL actuator at frequencies up to 30 Hz with a normalized room means squared error below 6% [153].

3.4 Frequency response of single-unit closed loop system

3.4.1 System identification of the open loop system

We validated the sensor in a closed loop system with a single unit. We performed sinewave-based, dynamic tests with logarithmic chirp input signal to experimentally determine an open loop model of the actuator. Here, we used the laser position sensor to measure the actuator's true change in height. This system identification technique is the same as what was derived in Chapter 2.

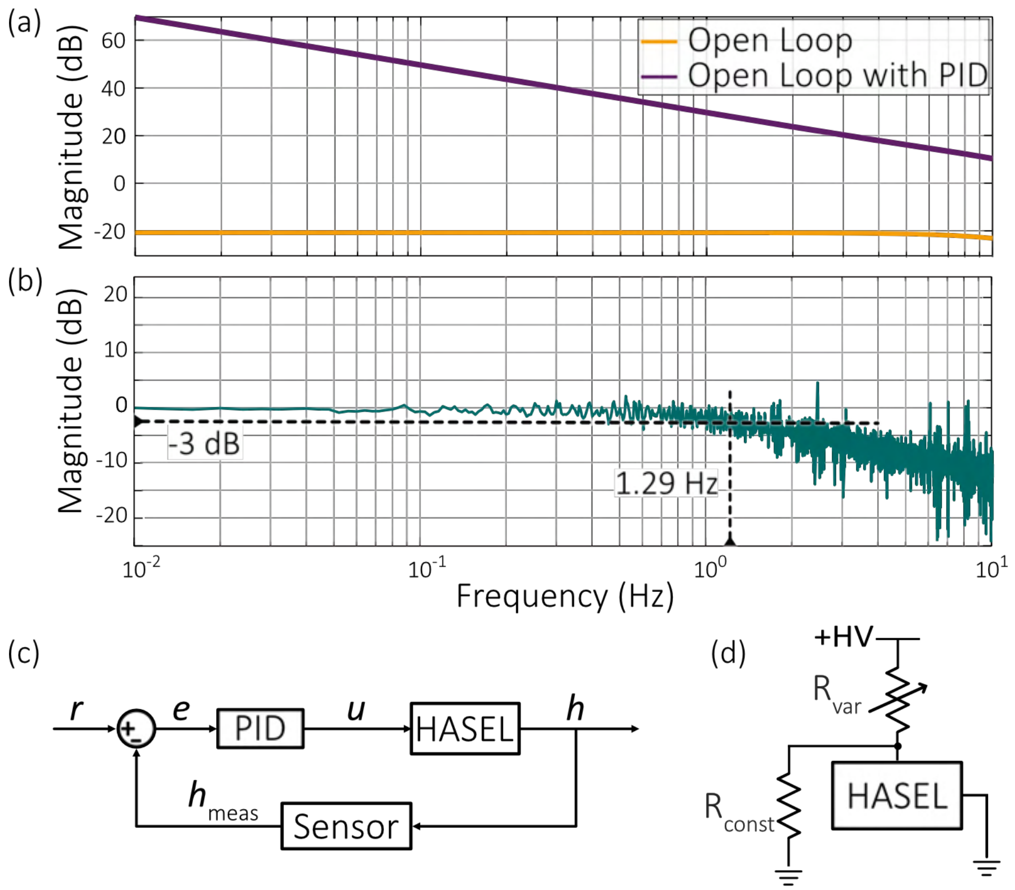

Figure 3.1: **(a)** The magnitude frequency response of the approximated HASEL model (h (mm)/D_{var} (%)) compared to the approximated open loop system, or the feed forward loop gain, which includes the PID controller shown in (c). **(b)** The magnitude frequency response of the closed loop system. The magnitude compares the output measured height to the input reference signal. Here, the corner frequency (1.29 Hz) is labeled. **(c)** A block diagram of the closed loop system using a PID controller and the magnetic sensor to control the HASEL actuator. **(d)** A basic schematic of the driving circuit. The impedance of the variable resistor R_{var} is used control the voltage across the HASEL actuator.

However, instead of using the TREK to provide the variable voltage to the HASEL actuator, we used a driving circuit (see Fig. 3.1(d)).

The driving circuit design is similar to existing HV switches that are used to control DEAs [154] and HASEL actuators [88]. We customized an optocoupler used on the driving circuit using an infrared LED (L1IZ-0940000000000, Lumileds) and an opto-diode (OZ100SG, Voltage Multipliers, Inc.). We used a pair of optocouplers for each actuator: a charging optocoupler with a variable PWM duty cycle D_{var} (%) and a discharging optocoupler with a fixed 45% PWM duty cycle D_{const} (%). The frequency of both PWM inputs was 500 Hz. By changing D_{var}, we can tune the current through the actuator, thereby controlling the input voltage. We fixed D_{const} to simplify the feedback control to a SISO system. D_{const} was tuned to obtain a reasonable relaxation time, which describes the time it takes for the actuator to reduce in stroke when the input voltage decreases. The driving and discharging optocouplers act like a variable resistor R_{var} and a fixed resistor R_{const} (see Fig. 3.1(d)).

A high voltage amplifier (610E, TREK) supplies a constant voltage of 8 kV to the driving circuit. The driving circuit allows for independent control of multiple units in tandem by regulating what fraction of the 8 kV HV line each actuator sees. Using the driving circuit to vary the voltage input during the characterization tests allowed us to use the model and controller designed for a single unit in the larger, multi-unit deformable platform described in Section 3.5.

To vary the voltage to the actuator, D_{var} (t) is determined by a logarithmic chirp signal generated in MATLAB:

$$D_{var}(t) = Asin(2\pi f(t)t) + D_{const} \tag{3.2}$$

where A is the amplitude of the input signal (%), t is time (s), and D_{const} is the operating point (45% duty cycle). The frequency $f(t)$ of the input sinewave is determined by

$$f(t) = f_0 \left(\frac{f_1}{f_0}\right)^{t/T} \tag{3.3}$$

where f_0 and f_1 are the starting and ending frequencies (Hz), respectively, and T is the total time of the chirp signal (s). We fixed the f_0 at 0.01 Hz, the f_1 at 20 Hz, and T at 360 s. We have observed that the maximum stroke of a folded HASEL actuator reduces as frequency increases, until approximately 20 Hz, when the actuator's stroke is minimized to a vibration [121]. Therefore, we mainly focused on the dynamics of the actuator at frequencies below 20 Hz. The amplitude of D_{var} was 30%, making the range of D_{var} equal 15 – 75%. This amplitude was experimentally tuned to allow the HASEL actuator to move along its full range of motion at lower frequencies.

We recorded the mapped sensor data, the measured laser position sensor data, and the PWM input at a sampling frequency of 500 Hz to estimate a transfer function that maps the input PWM duty cycle D_{var} (%) to the output HASEL actuator height h (mm). Although we were only interested in the response of the actuator for frequencies below 20 Hz, we used a sampling frequency larger than ten-times the end frequency to ensure that we were obtaining enough data for characterization. Based on this frequency response data, we approximated our open loop single unit as a second-order transfer function:

$$P(s) = \frac{683}{s^2 + 145.5s + 7452} \tag{3.4}$$

3.4.2 Controller design and closed loop system dynamics

While this system is stable, as verified by a Routh-Hurwitz stability test, we wanted to improve the steady-state error and the tracking performance at lower frequencies. We designed a PID controller that increases the gain at lower frequencies to keep the tracking error below 5% up to a 2.86 Hz corner frequency, (see Fig. 3.1(b)). This requires the magnitude of the open loop system with the PID controller to be larger than 20 dB up to 2.86 Hz, which we achieve (see Fig. 3.1(a)). The integral component of the controller also insures no steady state error. The discrete-time equations for PID control at time-step k with reference height r, input to the MCU u, measured height h_{meas}, and height error e are:

$$e[k] = r[k] - h_{meas}[k] \tag{3.5}$$

$$u[k] = u[k-1] + Ae[k] + Be[k-1] + Ce[k-2] \tag{3.6}$$

The coefficients on the controller are calculated with:

$$A = K_p + \frac{K_i}{2f} + K_d f, \quad B = -K_p + \frac{K_i}{2f} - 2K_d f, \quad C = \frac{K_d}{f} \tag{3.7}$$

where f is the closed loop frequency (Hz), $K_p = 4,061$, $K_i = 45,800$, and $K_d = 0.002$ are the tuned PID constants. The input u from Eq. (3.6) is the 16-bit value which corresponds to D_{var} (%); that is sent to the optocoupler via the MCU. The PID constants are generally large because of the conversion from single-digit actuator heights in mm to five-digit PWM values. However, K_d was kept relatively small to prevent overshoot from the controller.

To measure the bandwidth of the closed loop system, we generated a logarithmic chirp input like the input described in Eqs. (3.2, 3.3). However, to understand the frequency response of the closed loop system, we examined the frequency response between the laser position sensor data (output) and the reference heights (input). The reference heights $h_{ref}(t)$ were determined using:

$$h_{ref}(t) = Asin(2\pi f(t)t) + h_{off} \tag{3.8}$$

where $f(t)$ was computed using Eq. (3.3) with $f_0 = 0.01$ Hz, f_1= 20 Hz, and $T = 360$ s. The offset height h_{off} was 3 mm and the amplitude A was 3 mm, resulting in an h_{ref} range of 0-6 mm. Since the HASEL actuation stroke is minimal at frequencies above 20 Hz, we set the closed loop frequency to greater than ten times that frequency at 250 Hz. The controller was programmed in Julia v1.6.2 [155], which read the magnetometer and the laser position sensor data from the MCU and sent PWM inputs to the MCU via USB.

The Bode plot of the closed loop system is shown in Fig. 3.1(a), where the input is reference height h_{ref} (mm) and the output is the tracked height of the actuator h (mm). We can achieve at least 70% of the total actuator stroke (-3 dB) at a corner frequency of about 1.29 Hz. This low corner frequency is not surprising when we consider the intrinsic dynamics of the HASEL actuator, which result in a 2.86 Hz corner frequency for the open loop system (comparing input PWM signal to output height). However, this indicates that the closed loop performance will result in higher errors at higher actuation frequencies if the reference height approaches the maximum stroke.

3.5 Deformable platform demonstration for multi-sensor, multi-actuator closed loop control

3.5.1 Demonstrating magnetic sensing on a multi-unit system

To demonstrate the scalability of a single unit, we created a multi-unit soft robotic platform, referred to as the deformable platform. This application showcases the sensor's ability to be used near the electric field generated by the HASEL actuators and highlights the minimal sensor coupling among nearby sensors without impacting the sensor's accuracy or precision. The individual unit control (Fig. 3.2(a)) allows for position tracking of the platform's end effector.

3.5.2 Design of the deformable platform

Our deformable platform is comprised of two segments (top and bottom), with each segment driven by units placed in tri-radial symmetry (Fig. 3.2), like designs of other soft robotic platforms [156,157], where there is a 120º separation between the placement of each actuator on each segment. The elongation of any of the three actuators causes a pose change of the segment's top surface (Fig. 3.2(b)).

The magnetic sensing setup is the same as for the individual unit in Section III; each of the three units has its own magnetic block and sensor. The top of each segment is a 1.5 mm acrylic sheet, and the bottom is the sensor PCB described in Section 3.5.3. To match the 120º separation between each unit on both segments, the units are labeled as such on each segment: b_0, b_{120}, b_{240} on the bottom segment and t_0, t_{120}, t_{240} on the top segment; b_0 lies below t_0, b_{120} below t_{120}, and b_{240} below t_{240} (Fig. 3.3(a)).

At the boundary between the first and second segments, the magnetic blocks of the bottom segment are near the magnetic sensors of the top segment; however, there is no relative motion between them. Therefore, the magnetic blocks in the bottom segment only impact the base magnetic field measured by the sensors on the top segment. The sensors of the top segment still have full sensitivity to the changes in heights of their respective magnetic blocks.

We used a 4-camera motion capture system (Primex 13, OptiTrack) to track the reflective markers used to calibrate the six sensors and measure the end effector's true position during the closed loop control experiments. During the calibration process described in Section 3.5.4, six reflective markers were placed in-line with the center of each actuator, perpendicular to the edge of the acrylic divider. During the closed loop experiments, a reflective motion-capture marker was placed on the center point of the top acrylic plate (Fig. 3.2(c)). The marker mount was 60 mm tall, and the spherical marker diameter is 8 mm. We defined the center of the marker as the end effector of the deformable platform and used this to measure the overall error between the end effector position and the reference trajectory.

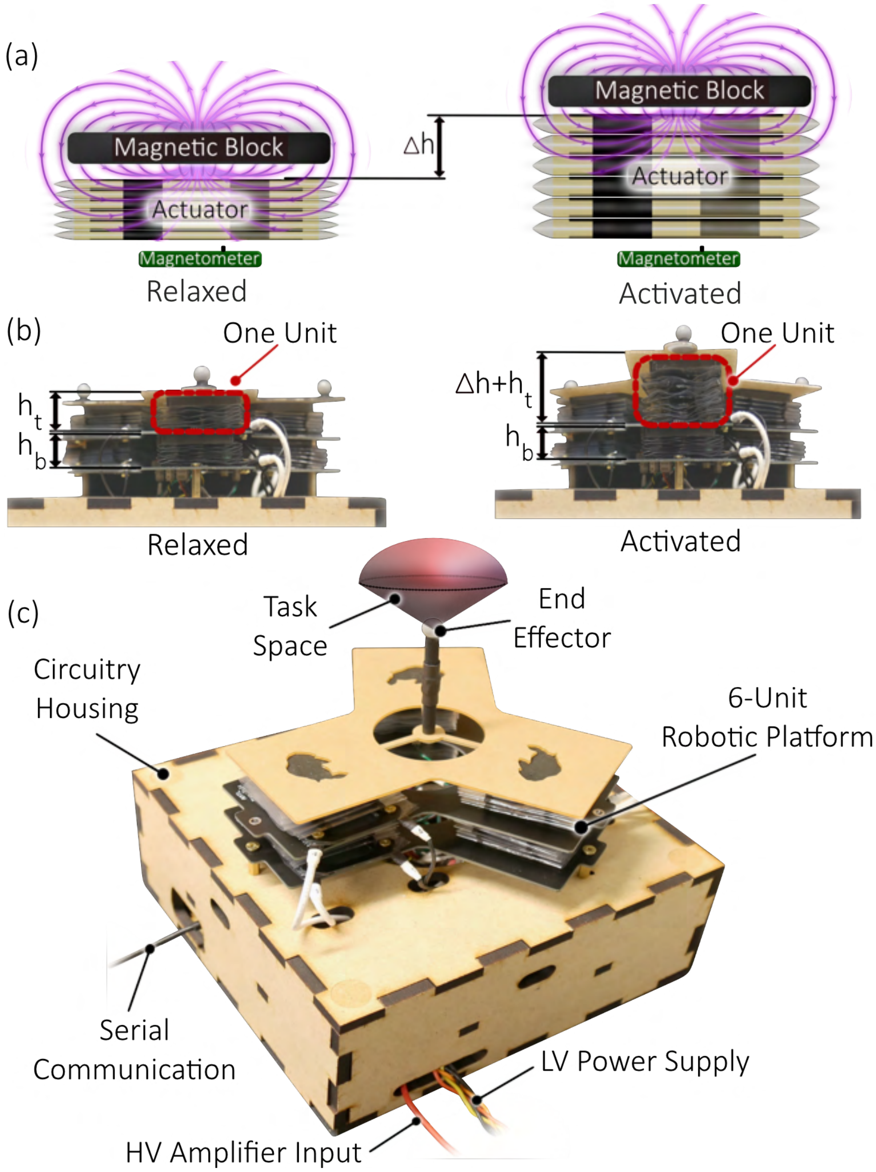

Figure 3.2: **(a)** One unit includes the magnetic sensing mechanism (composed of the magnetometer and soft magnetic block) used to measure the change in height, Δh, of a folded HASEL actuator. **(b)** The front view of the 6-unit deformable robotic platform when relaxed and when one actuator on the top layer is activated. Each layer is comprised of three of the units shown in (a). The height of the top layer ht is measured relative to the base of the top layer. The bottom layer height h_b is relative to the stationary base. **(c)** An isometric view of the two-segment deformable platform. The task space represents the volume that the deformable platform's end effector can exist. A high voltage (HV) amplifier provides 8 kV to each of the six actuators, which are individually controlled by a microcontroller unit (MCU). The low voltage (LV) power supply provides 3.3 V to the magnetometers and the low voltage circuit components that control the actuators. The MCU is mounted in the circuitry housing and communicates to a computer via serial communication.

3.5.3 Platform circuitry

The base of each segment is a printed circuit board (PCB) that connects the sensors in parallel. These base PCBs connect the three sensors in parallel for each segment and allow for the attachment of additional base PCBs. Each base PCB interfaces with the three HASEL actuators on each segment and their respective driving circuits. To prevent arcing between the HV across the actuators and the LV components of the sensing mechanism, the section where the actuators attach to the PCB is isolated from the rest of the PCB.

The bottom base PCB is connected to the same MCU that is sending signals to the six driving circuits. The MCU receives all six sensor signals at 250 Hz as 16-bit integers before converting the data to magnetic flux density B_Z in mG. To minimize the large noise spikes in the sensor data, we applied a three-point moving median filter. An AC/DC power supply (SF600, Corsair) supplies 3.3 V to both base PCBs and to the six driving circuits.

3.5.4 Sensor mapping to actuator height

We used the motion capture system to collect the true heights for calibration; this was required to map the change in magnetic flux density to change in actuator height for the deformable platform. The motion capture system tracked the movement of six reflective motion capture markers at 240 Hz during the platform calibration tests. We fed the x, y, and z coordinates of each reflective marker through a set of parametric equations to account for the distance between the actual center of the actuator and the center of the motion capture marker. The baseline height of the bottom segment was approximately 26 mm (from the magnetometer to the magnetic block) and the baseline height of the top segment was approximately 28 mm.

We performed six calibration tests, where each test measured the change in marker position and change in magnetic flux density as the actuator received a series of step inputs: 1) input steps from 2 to 8 kV with 1 kV increments and held at 5 s each and 2) 0.5 kV steps held at 5 s starting at 8 kV and stepping down to 2 kV. We then fit the magnetometer data to the z-position of the respective marker using the same fitting function from Section IV.B. There is some variability in the polynomial coefficients for each actuator due to the higher baseline values of the top segment, differences in the structure and fabrication of each actuator, and error in the placement of the top segment, affecting the weight distribution experienced by the bottom segment.

Platform kinematics and control

The aim of the deformable platform is to demonstrate integrated sensing between multiple sensors and actuators, so we implemented closed loop feedback control individually on each of the six units, as outlined in Fig. 3.3(c). The loop is closed around the height of each HASEL actuator at a closed loop frequency of 250 Hz. The desired position of the platform end effector, $\boldsymbol{p} = (x, y, z) \in \mathbb{R}^3$, is fed into our custom inverse kinematic solver using MATLAB (R2021a, MathWorks), described later in this section, which computes the necessary heights for all six actuators $[r_1, r_2, r_3, r_4, r_5, r_6]$. These heights are sent to the individual controllers in Julia (v1.6.2), effectively moving the end effector to the desired position.

We implemented the PID controller derived on the single unit in Section 3.4 for each of the six units in the deformable platform (see Fig. 3.3(c)). The hardware is identical and each of the six driving circuits receive the same 8 kV input from the TREK. Utilizing identical hardware and software setup for the multi-unit system highlights the independence and modularity of the sensor and controller for each unit.

We approximated the inverse kinematics of the deformable platform to relate the end effector's position in $\mathbb{R}^3$ to the scalar heights of the six actuators on the platform. These heights can then be set as the reference height $r[k]$ in (4) for the closed loop controller of each actuator/sensor unit. Since our primary focus is to demonstrate the effectiveness of independent and uncoupled multi-HASEL actuator control, we developed an inverse kinematic approach which is much simpler to implement than typical methods [158, 159], but at the cost of end effector tracking accuracy.

Following Jones et al., the kinematics can be represented as two mappings; the task space can be mapped to a configuration space, and the configuration space mapped to the actuator space [160]. We are defining the actuator space as the space where the six actuators can move based on a given reference height input and the task space as the volume where the platform is physically able to track a given reference trajectory. Our configuration space is based on three basis vectors $\{\hat{\boldsymbol{b}}_1, \hat{\boldsymbol{b}}_2, \hat{\boldsymbol{b}}_3\}$ and describe the stacked pairs of HASEL actuators: the first basis vector corresponds to the movement of the b_0 - t_0 actuator unit pair, the second to the $b_{120} - t_{120}$ pair, and the third to the $b_{240} - t_{240}$ pair. The three basis vectors span S, which is a subset of $\mathbb{R}^3$ that describes the task space. A visual representation of $\hat{\boldsymbol{b}}_1$ is illustrated in Fig. 3.3(a).

The basis vectors were experimentally determined by recording the position of the end effector position using the motion capture system as the three HASEL actuator pairs were independently actuated (see Fig. 3.3(a)). For example, when b_0 and t_0 are actuated to their respective maximum heights, and we can measure the change in the end effector position as (x_0, y_0, z_0), then the basis vector $\hat{\boldsymbol{b}}_1$ for the $b_0 - t_0$ pair is

$$\hat{\boldsymbol{b}}_1 = (x_0, y_0, z_0) \tag{3.9}$$

Thus, actuating HASEL actuators b_0 and/or t_0 to any height, while keeping the other actuators unactuated, will move the end effector to a position of $\alpha\hat{\boldsymbol{b}}_1$, where α is a scalar value that represents the projection of $\boldsymbol{p}$ on $\hat{\boldsymbol{b}}_1$ (see Fig. 3.3(b)). We use the same experimental process of measuring the position change of the end effector when the $b_{120} - t_{120}$ pair and the $b_{240} - t_{240}$ pair are fully actuated to determine $\hat{\boldsymbol{b}}_2$ and $\hat{\boldsymbol{b}}_3$, respectively. Note that we have linearized the end effector path; although the true path has curvature, supported by constant-curvature kinematic models [161], it is negligible enough within our platform to be linearized (see Fig. 3.3(a)), which greatly simplifies our mappings with some reduction in accuracy.

This allows us to represent the referenced end effector position p as a linear combination of the bases $\{\hat{\boldsymbol{b}}_1, \hat{\boldsymbol{b}}_2, \hat{\boldsymbol{b}}_3\}$:

$$\boldsymbol{p} = (x, y, z) = \alpha\hat{\boldsymbol{b}}_1 + \beta\hat{\boldsymbol{b}}_2 + \gamma\hat{\boldsymbol{b}}_3 \tag{3.10}$$

where α, β, and γ are the scalar parameters corresponding to the reference heights of each respective tri-radial HASEL actuator pair. Any position $\boldsymbol{p}$ within $S \in \mathbb{R}^3$ can be expressed as a sum of these scaled basis vectors. The inverse mapping from the task space S to the configuration space is calculated as

$$\begin{bmatrix} \alpha \\ \beta \\ \gamma \end{bmatrix} = [\hat{\boldsymbol{b}}_1 \;\; \hat{\boldsymbol{b}}_2 \;\; \hat{\boldsymbol{b}}_3] \cdot \boldsymbol{p} \tag{3.11}$$

The mapping from the configuration space to the actuator space is achieved via piecewise linear

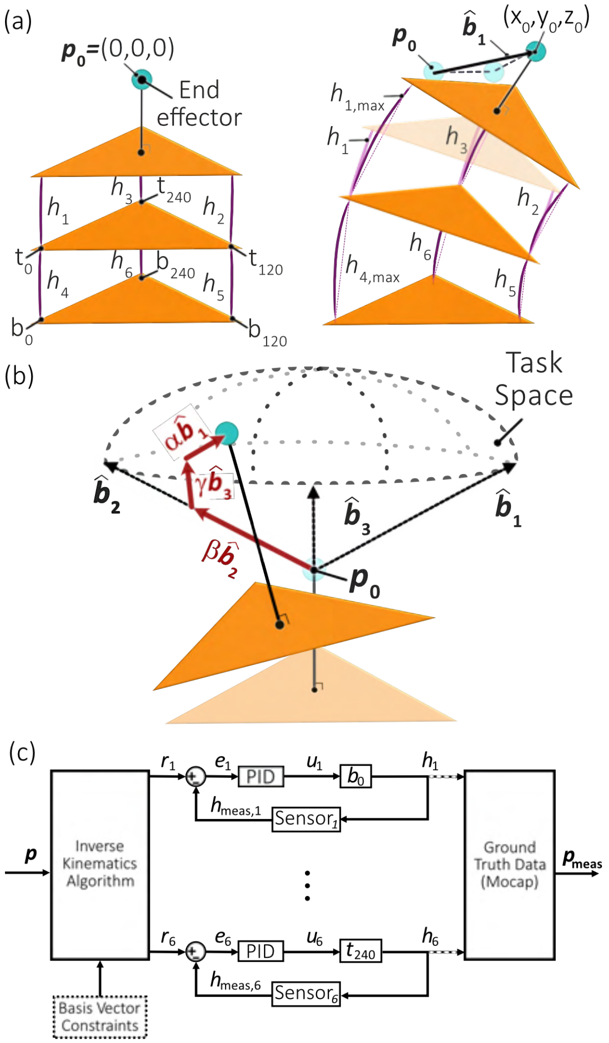

Figure 3.3: **(a)** We experimentally determine three basis vectors $\{\hat{\boldsymbol{b}}_1, \hat{\boldsymbol{b}}_2, \hat{\boldsymbol{b}}_3\}$ by determining the change in end effector position (x_0, y_0, z_0) in reference to the end effector's starting position $\boldsymbol{p}_0 = (0, 0, 0)$ when an actuator pair (the 0º, 120º, or 240º position pairs) is at its max stroke. This diagram shows how the basis function $\hat{\boldsymbol{b}}_1$ determined: the vector created by the end effector position when the b_0-t_0 pair is fully actuated compared to $\boldsymbol{p}_0$. For the kinematics model, the changes in stroke are assumed to be a linear (dotted line), but the changes in actuator stroke are slightly curved (thick, curved line). Additionally, the position change between the end effector position when b_0 is fully actuated and when t_0 is fully actuated is assumed to be constant. **(b)** The corresponding projections of a reference end effector position $(\alpha\hat{\boldsymbol{b}}_1, \beta\hat{\boldsymbol{b}}_2, \gamma\hat{\boldsymbol{b}}_3)$ are used to determine the six heights $(h_1, h_2, h_3, h_4, h_5, h_6)$ of the actuators based on the reference end effector position $\boldsymbol{p}$ in $\mathbb{R}^3$. In this example, b_{120} is fully actuated and t_{120} and b_0 are partially actuated. Therefore, $\boldsymbol{p}$ can be expressed as a combination of $\alpha\hat{\boldsymbol{b}}_1$ and $\gamma\hat{\boldsymbol{b}}_3$. **(c)** The inverse kinematic algorithm outputs the reference heights r for all six actuators. The difference between the reference height and the measured height is the error e in mm that feeds into each controller. The six, identical PID controllers independently control the heights of the folded HASEL actuator stacks h in mm based on their respective mapped, measured height from the magnetometer output h_{meas} in mm. The resulting end effector position $\boldsymbol{p}_{meas}$ in mm is measured by the motion capture system.

Table 3.1: HASEL heights as a percentage of maximum for α, β, γ

$0 \leq \alpha \leq 0.5$	$0 \leq \beta \leq 0.5$	$0 \leq \gamma \leq 0.5$
t_0: 0% b_0: 100α%	t_{120}: 0% b_{120}: 100β%	t_{240}: 0% b_{240}: 100γ%
$0.5 < \alpha \leq 1$	$0.5 < \beta \leq 1$	$0.5 < \gamma \leq 1$
t_0: $100(\alpha - 1)$% b_0: 100%	t_{120}: $100(\beta - 1)$% b_{120}: 100%	t_{240}: $100(\gamma - 1)$% b_{240}: 100%

functions of the parameters α, β, and γ. Parameter values between 0 and 0.5 are linearly scaled between the min-max heights of the HASEL actuators on the bottom segment of the platform, and values between 0.5 and 1 are scaled between the min-max heights of the HASEL actuator on the top segment in addition to the fully actuated HASEL actuators on the bottom segment. This breakdown is laid out in Table 3.1. Using the combined mappings from the task space to the configuration space (Eq. (3.11)) and the configuration space to the actuator space (Table 3.1), we can generate a unique solution for the 6 reference HASEL actuator heights $[r_1, \ldots, r_6]$ for any given end effector position $\boldsymbol{p}$ (see Fig. 3.3(b)).

To increase ease of implementation and reduce computational complexity, this inverse kinematic approximation technique uses several simplifications of the real behavior of the platform. As mentioned previously, we linearized the end-effector path during the experimental characterization to form the three basis vectors $\{\hat{\boldsymbol{b}}_1, \hat{\boldsymbol{b}}_2, \hat{\boldsymbol{b}}_3\}$. In addition, the superposition of the basis vectors as shown in Eq. (3.10) is not mathematically proven to result in a superposition of the end effector position on the robot.

These assumptions result in small inaccuracies in the inverse kinematic approach. To improve the inverse kinematic accuracy, we additionally scaled α, β, and γ depending on the distance of the end effector position from the origin. This was achieved experimentally by fitting the predicted end effector position to data obtained from the motion capture system. However, this tuning has no impact on the closed loop performance of each local control loop; it only improves the accuracy of end effector prediction to account for the simplifications that were used.

3.6 Closed loop control results

We demonstrate the ability to perform precise tracking control of a reference trajectory in $\mathbb{R}^3$ by commanding the deformable platform to follow a reference conical helix, where the approximate maximum range in the x-direction is 13 mm, 11 mm in the y-direction, and 5 mm in the z-direction. The reference position p traces the conical helix that starts at $\boldsymbol{p} = (0, 0, 0)$ and increases in diameter and height (see Fig. 3.4(b)). Despite the assumptions made to simplify the platform kinematics, the deformable platform was able to successfully track the helix trajectory, shown in Fig. 3.4(b). The error between the reference heights determined from the reference end effector position and the measured heights based on the outputs of the six magnetometers is minimal (Fig. 3.4(a)). The average residual errors for actuators b_0, b_{120}, b_{240}, t_0, t_{120}, t_{240} are $|e| = [0.10, 0.11, 0.14, 0.10, 0.069, 0.032]$ mm, respectively, where the total average is 0.093 mm.

While the residual errors between the mapped and reference heights for all six actuators are low, there is some increased variability between the measured end effector position $\boldsymbol{p}_{meas}$ and the reference end effector position $\boldsymbol{p}$. The mean of the overall residual error,

$$|e|_{xyz} = \sqrt{(x - \hat{x})^2 + (y - \hat{y})^2 + (z - \hat{z})^2},$$

is 0.45 mm. This increase in error is due to the previously mentioned simplifications of the platform kinematics used when calculating the heights of each actuator based on the desired end effector position.

3.7 Conclusion and discussion

This demonstrates the effectiveness of using a magnetic-based sensing mechanism to measure shape deformations of soft electrostatic and electro-hydraulic actuators, specifically HASEL actuators. The sensing method is simple and elegant to manufacture, scale, and implement, and it proves to be a highly effective method when used with soft electrostatic and electro-hydraulic actuators.

In addition to a high resolution, this sensing mechanism is not influenced by HV noise from HASEL actuators, resulting in a clean mapping between change in magnetic flux density and change in actuator height, even at the high end of the actuator operating range (30 Hz). When compared

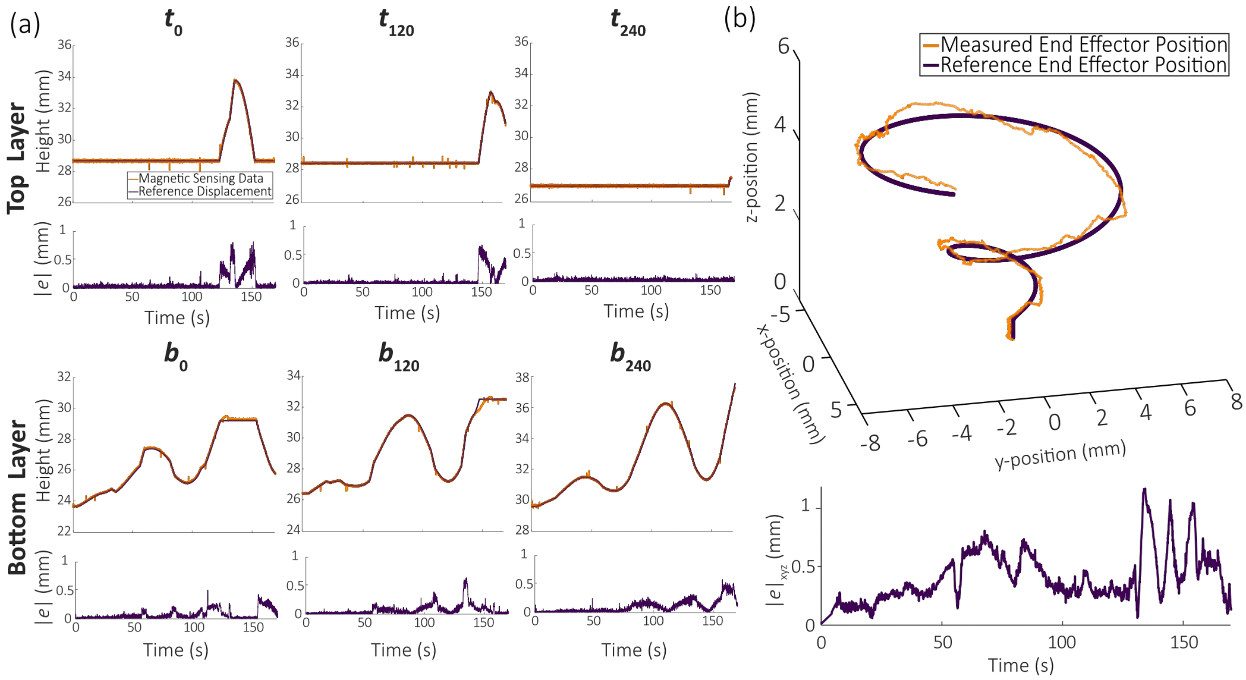

Figure 3.4: **(a)** The measured heights based on sensor data h_{meas} and the reference heights r for all six actuators. There is minimal absolute error between the mapped height from the magnetic sensing data and the commanded reference displacement, which is shown below each height subplot. The mean $|e|$ across all six actuators is 0.093 mm. **(b)** The measured $\boldsymbol{p}_{meas}$ and reference end effector positions $\boldsymbol{p}$ start at $\boldsymbol{p}_0 = (0, 0, 0)$ and move up along a predetermined spiral as each actuator follows the prescribed profile shown in (a). Tracking a reference conical helix demonstrates the precise control that the platform can accomplish using the magnetic sensing mechanism and a basic control method. The mean of the overall residual error ($|e|_{xyz}$) shows the magnitude of the error between $\boldsymbol{p}_{meas}$ and $\boldsymbol{p}$.

to the capacitive stretch sensor previously used to measure the change in HASEL actuator stroke, the magnetic sensing mechanism is significantly more accurate. The $|e|$ for the magnetic sensor is approximately eight times less than that of the capacitive stretch sensor. We expected this performance since the capacitive sensor is affected by the electric field generated by the HASEL actuator, but the magnetic sensor is not.

We characterized a unit and approximated the open loop system as a second-order transfer function. Based on this model, we designed a PID controller that we used to control six units in a deformable platform. This highlights the ability to independently control multiple units, a task that we have found to be difficult using other soft sensors. For the deformable platform, we assumed the changes in magnetic flux density measured by each sensor were independent of the environment. In reality, the tilt of the platform adds a slight influence on the change in magnetic flux density that each magnetometer measures. Accounting for this would improve the accuracy of the mapping and performance of the controller.

Despite the fully decoupled magnetic field assumption to allow for independent control, we can maintain a low tracking error for each individual HASEL actuator height (see Fig. 3.4(a)), where the average $|e|$ for all six units is 0.093 mm. The error between the reference end effector position, which is fed through our inverse kinematic algorithm to generate the six HASEL actuator reference heights, and the actuator position, which is measured by the motion capture system, is 0.45 mm. The assumptions made to simplify the inverse kinematics algorithm increased the overall end effector tracking error. Additionally, the small error in height for each of the six units amplifies the overall end effector tracking error. However, we were not controlling the position of the end effector (see Fig. 3.3(c)), so this error does not give us much information about the performance of the sensing mechanism in a multi-unit soft robotic system.

Overall, there is a plethora of applications that can use this simple sensing mechanism in soft robotic systems due to its high resolution and accuracy, high sampling frequency, ease of manufacturing, and scalability. In particular, the scalability of these sensor mechanism (up to larger arrays of actuators/sensors) makes this system very useful in the development of HASEL actuator-driven soft robotic materials. In contrast to the capacitive sensor discussed in Chapter 2, which suffered from electromagnetic coupling and noise and subsequently prevented the system from scaling to multiple DOF, those influences are eliminated through this method.

3.8 Acknowledgements and contributions

As the work presented in this chapter is the result of collaboration with multiple researchers, here I describe the contributions of each team member for clarity. The conceptualization of this work was done by Vani Sundaram, Khoi Ly, myself, Mark E. Rentschler, and Nikolaus Correll. The design of the magnetic sensing mechanism was done by Khoi Ly and Vani Sundaram. Characterization and modeling of the magnetic sensing mechanism was done by Vani Sundaram. The folded HASEL actuator design and material selection was performed by Eric Acome. System dynamic modeling and data collection was performed by Vani Sundaram. The design of the deformable platform, microcontroller pinout, and circuit design was also performed by Vani Sundaram. The HV driving circuit was designed by Mantas Naris and Shane K. Mitchell with additional improvement by Angella Volchko and myself. Figure visualizations were created by Vani Sundaram, Khoi Ly, and myself.

In addition to the above, I created the inverse kinematic model for the deformable platform, performed data collection and identification of the basic vectors, created the software for the inverse kinematic solver and for the closed loop controller, tuned the closed loop control algorithm, and performed data collection and analysis of the kinematic end-effector control.

Chapter 4

Developing a HASEL-actuated soft robotic material: sTISSUE[3]

In this chapter, we build upon the previous work presented in Chapters 2 and 3. While Chapter 2 discussed sensor integration and feedback control for a single HASEL actuator, and Chapter 3 expanded this to a 6-actuator, 6-sensor system with more complex controls, here we seek to scale these systems even further: a 100-actuator, 100-sensor system with feedback control that enables advanced functionality in soft robotic systems.

4.1 Introduction

Soft robots possess several advantages over traditional robotic systems due to their mechanical compliance – including embodied intelligence, robustness, adaptability, and inherent user safety – leading to a wide range of applications like in biomedical devices, wearable technology, and human-robot-interaction [5–11, 93]. Biological systems often inspire soft robot designs and are considered the gold standard of high-performance, adaptable, and multifunctional soft systems [8,40,105]. Yet many examples of soft robots [27,33,34,37,40,42,71,73,162,163] contain fewer than 10 independent actuators and sensors, while multifunctional biological structures like the human body have more than 600 unique muscle groups [103] with sensory receptors embedded throughout the body [104]. The disparity in functionality between existing soft robotic systems and biological organisms can be explained partly due to the contrasting quantity of actuators and sensors between the two: additional actuators and sensors yield additional degrees of freedom (DOF) as well as redundancy in actuation and control. This DOF disparity is compounded by the emergent properties which

---

[3] The work in this chapter is presented *Brian K., Johnson*, Naris, Mantas*, et al. "A scalable multifunctional soft robotic material combining high-speed actuation, sensing, and control," in preparation for submission.* My contributions in this work lie in assisting with sTISSUE circuit and hardware design, performing system identification and data analysis, controller design, and demonstrating applications of this robotic material through active feedback control. As this is a collaborative work, full acknowledgements of the contributions of all authors are listed at the end of this chapter.

arise from the cellular-based structures of biological systems, in which the functionality of the system is greater than the sum of the individual components [105, 106].

One solution to bridge the gap between soft robots and biology may be the development of "robotic materials", systems which combine actuation, sensing, and control in large quantities [123, 124]. The design philosophy of such robotic materials mimics that of biology: the material is principally comprised of small constituent units which are repeated within a structural matrix (just as biological tissues are comprised of many repeated interacting cells). These units contain actuation, sensing, communication, and computation; coordination of all units in the material results in global functionality [124]. By repeating the constituent unit in two dimensions, planar robotic materials can be formed which can function as shape displays or interactive devices [122, 164]. Such soft robotic materials could yield increased robot functionality and intelligence, yet several challenges have prevented this development to date.

The first challenge is the ability to create high-DOF soft actuator arrays. Pneumatic soft actuators – valuable for high-force and high-strain applications – require complex flow and valve systems to control multiple actuators separately [109]. One approach to this problem used a single pneumatic source together with shape memory polymer actuators, which enabled independent actuation of more than 100 actuators in an array [165]. Electrostatic actuator arrays on the other hand face problems related to the independent control of high voltage (HV) to each actuator; many use a matrix addressing scheme from a single HV source for actuation control [62, 166, 167], but the control speed decreases as the array becomes larger. Other actuator arrays including shape memory alloy (SMA) and shape memory polymer (SMP) have also been demonstrated, but the response times of these methods are slower than 1 Hz [113, 165], limiting dynamic performance. In addition, many soft actuator systems do not integrate their energy source onto the robot, instead relying on tethered electrical or pneumatic power sources to drive actuation. Those which do integrate the driving method result in a very large device [122]. It is beneficial to integrate the driving components directly because it results in shorter electrical wires or pneumatic tubing, decreasing energy losses due to electrical or fluidic resistance. Integrating the driving components can also improve portability and scalability.

The second challenge in creating high-DOF soft robotic materials is the ability to create large sensor arrays that can integrate with actuators. Popular soft sensors like capacitive sensors exhibit capacitive crosstalk [168–170] which is amplified in the proximity of electrostatic actuators [121]. Resistive-type sensors can be scaled to large arrays relatively well and are less prone to crosstalk but are more sensitive to viscoelastic hysteresis and relaxation which prevent high frequency sensing [170, 171]. Since electrostatic actuators are capacitors themselves, self-sensing methods have demonstrated feasibility, yet they have not been able to scale for multi-actuator systems and have limited bandwidth [63, 90, 172]. Magnetic sensors, however, show high sensitivity without hysteresis, and the magnetic components can be embedded in an elastomer to maintain softness [147, 148]; this is a promising approach for any type of actuation. In conjunction with design challenges of the sensors themselves, many existing sensor arrays rely on a single computing source which limits the number of available inputs and limits the processing speed for multiplexed inputs [167], thus limiting the total size of the array.

Finally, the third challenge of creating high-DOF robotic materials is the integration and coordinated control of the soft actuator and sensor arrays. While previously highlighted examples show progress in creating actuator or sensor arrays separately, very few works combine them together for active feedback control [172]. Existing soft actuator arrays typically use open loop inputs without the ability to sense or react to stimuli [62, 110, 165, 173]. In other cases, the sensors on the array are not directly coupled with the actuators [167], limiting the ability for displacement feedback control. These robotic systems are thus unable to regulate their actuation states in the presence of external disturbances. For the systems which do combine actuation and sensing for direct closed loop feedback [172], the control strategies applied to the system are still insufficient for high-speed dynamic tasks. However, there are other high-DOF robotic materials which demonstrate high-speed communication and control albeit without actuation [127].

4.1.1 Creating a soft robotic material: sTISSUE

We present sTISSUE (Fig. 4.1) as a novel soft robotic material which addresses these scalability challenges. sTISSUE (synthetic tissue) demonstrates the integration of high-speed electrostatic actuation, magnetic-based sensing, and feedback control. The core design strategy of sTISSUE is based on a hierarchical architecture that enables easy scaling from a single constituent unit to larger arrays. Like biological tissue, which is comprised of constituent cells embedded throughout a structure matrix, sTISSUE is comprised of repeated 'cells' that combine actuation, sensing, and localized control within a lattice structure. Each cell within sTISSUE is driven by a hydraulically amplified self-healing electrostatic (HASEL) actuator, a class of soft electrostatic actuator that exhibits high actuation frequency and a power throughput comparable to biological muscle [63, 64]. A driver circuit enables independent voltage control of the HASEL actuator in each cell from a shared high voltage (HV) source. Embedded with the actuator is a soft magnetized block and corresponding magnetic field sensor, enabling displacement and force sensing of the cell. This cell is repeated to form higher dimension arrays. The combined coordination of all cells results in a soft robotic material that bridges the gap between simple, low-DOF soft robots and multifunctional, high-DOF biological systems (Fig. 4.1A).

We demonstrate a 10x10 (100 cell) shape display as a model system built from sTISSUE. Groups of 10 cells are organized into 1x10 modules which share power and computation, and these modules likewise share power from a centralized source. Computation is also hierarchically scaled, with voltage regulation implemented within each cell, displacement-feedback control integrated at the module level, and a global controller for the entire system operated by a centralized computer. sTISSUE simultaneously communicates with all 100 cells at 600 Hz. It is capable of surface deformation up to 30 Hz with a -3 dB bandwidth of 20 Hz. By sensing applied force, the system can react to the shape and pressure of external physical stimuli without the need of external sensors. Like a biological system, sTISSUE takes advantage of emergent properties that arise from the organization of cells into a larger structure [105, 106]. While each degree of freedom of a cell is limited to a vertical displacement, the combined actuation of cells enables the creation of transverse waves which can travel at high speed and manipulate objects (Fig. 4.1B). Embedded sensors enable displacement and force sensing of external objects. When combined in closed loop feedback, precise shape control is possible. This also allows for human interaction with sTISSUE. The force output of each cell also proportionally scales, enabling sTISSUE to move heavier objects at high frequency (Fig. 4.1B). Individual cell control means that these functions can be implemented simultaneously across the sTISSUE surface (Fig. 4.1B).

These combined capabilities result in a multifunctional, intelligent, high-DOF soft robotic material: the first in its class. In this work, we describe sTISSUE system design and fully characterize both static and dynamic performance from a single cell up to a demonstrated 10x10 material. We apply the system characterizations to develop high-speed feedback controllers at each hierarchical

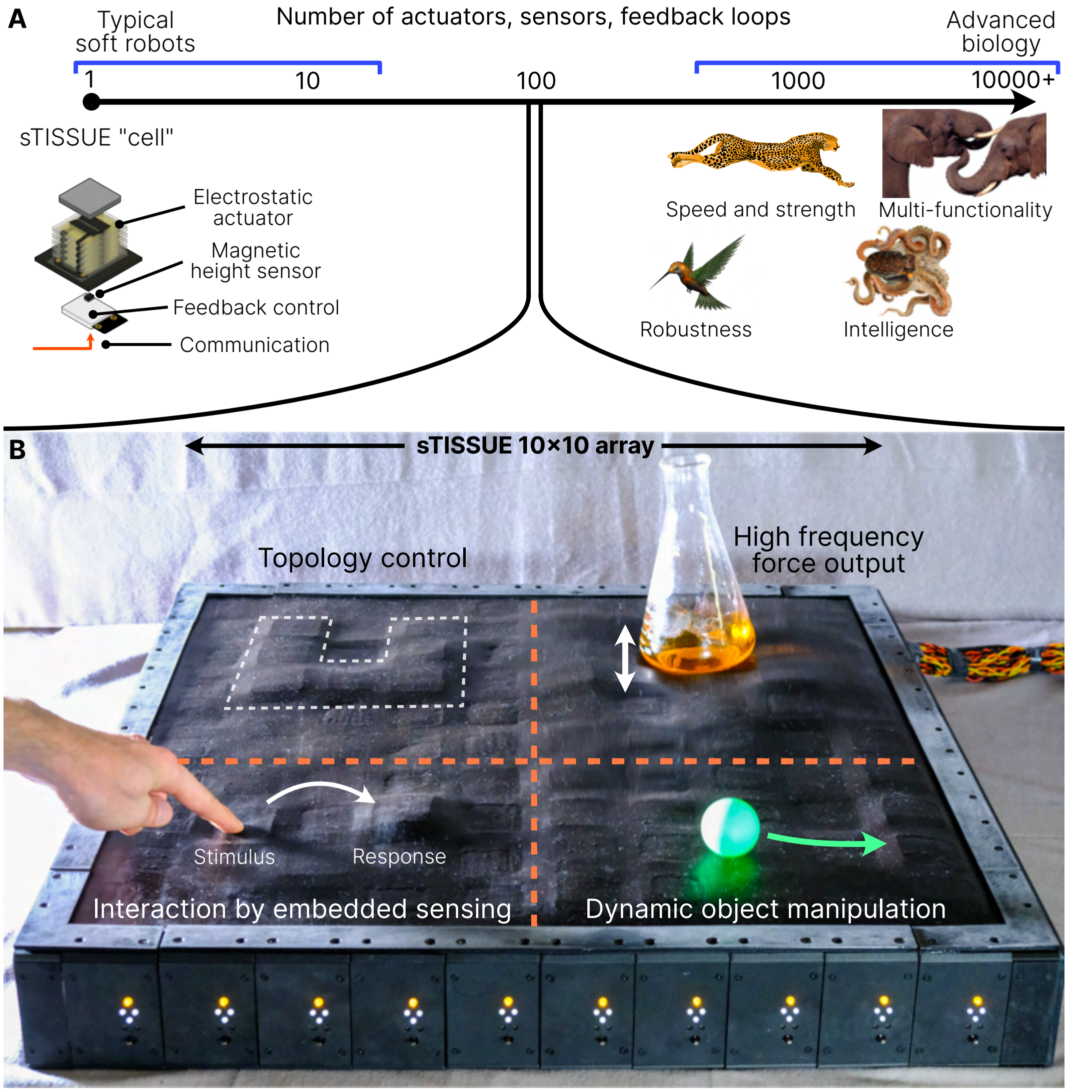

Figure 4.1: Motivation and overview of sTISSUE. **(A)** Using a single "cell" that combines actuator, sensing, and feedback which can scale to higher order arrays, sTISSUE bridges the gap between current soft robots and biological systems **(B)** A 10x10 sTISSUE array, consisting of 100 cells, acts as a high-speed, intelligent, multifunctional shape display capable of simultaneous activities.

level of the material and quantify their performance through practical demonstrations. Finally, we compare the results against existing actuator and sensor arrays and discuss future applications of such a soft robotic material.

4.2 Results

4.2.1 A hierarchical scalable electrohydraulic system with embedded sensing

sTISSUE is a fully integrated electrostatic system combining actuation, sensing, control, and communication. The basic hardware design scales from a single actuating and sensing "cell" (Fig. 4.2A). At the cellular level, each cell contains a folded HASEL actuator which transduces voltage to vertical strain using electrohydraulic principles [87, 88]. The choice of HASEL actuator is because of the high achievable actuation frequencies [88], low power use during activation, and lack of complex valve systems required by high-frequency pneumatic actuators. The actuator voltage is controlled through a HV driving circuit and sensor, described later. By placing a magnetized silicone block on top of the HASEL actuator and a magnetometer (magnetic field sensor) below it, the displacement of the actuator can be measured. This forms the same actuator/sensor "unit" described in Chapter 3. Unlike other sensing methods [121], the magnetic-based system is not susceptible to electromagnetic coupling with the actuators.

The basic cell is supported by a scalable power supply and control architecture (Fig. 4.2B). Up to 10 cells are laid adjacent to each other and combine into a single "module" which shares a HV amplifier, a Driver micro-Controller Unit (DCU), a Sensor micro-Controller Unit (SCU), and a power distributor. The HV amplifier supplies the HV and ground (GND) rails to all 10 cells. A capacitor bank also acts as a temporary source of current during high intensity applications. The DCU reads the voltage divider measurements from each cell through dedicated analog-digital-conversion (ADC) pins, runs closed loop voltage regulation for each cell, and sends command signals to the HV driver circuit in each cell. The SCU records magnetometer measurements from each cell using a serial peripheral interface (SPI). The power distributor supplies low voltage inputs to power the controllers, sensors, opto-couplers, and HV amplifier. Each module supports 1-10 cells (with minor changes, even more cells can be supported; see Discussion), enabling an easily scalable system.

Above the module level, the material level integrates each module to form sTISSUE (Fig. 4.2C). In our model system, 10 modules each with 10 cells are placed adjacent to each other forming a 10x10 sTISSUE shape display. A continuous silicone skin is stretched across the top surface of

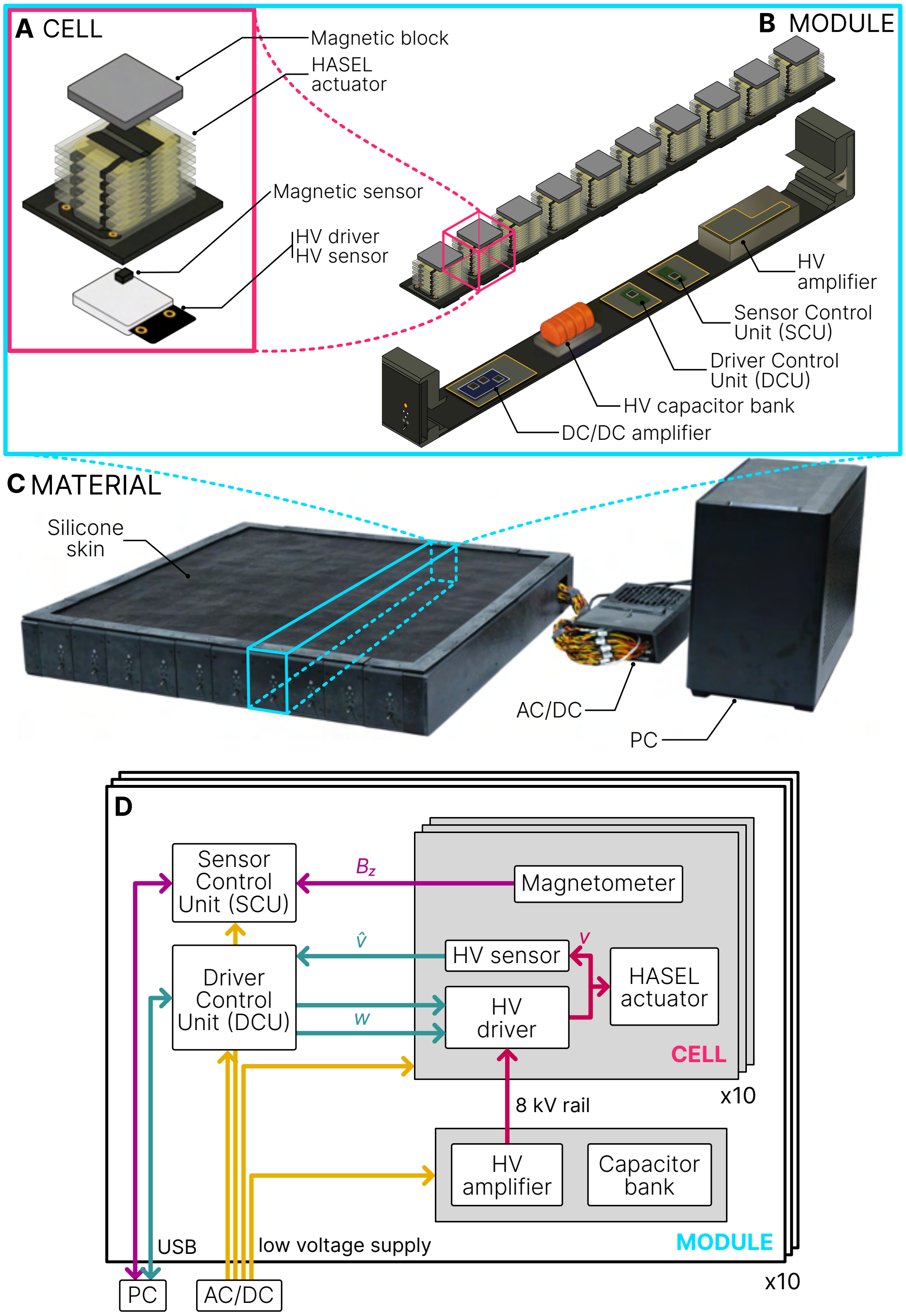

Figure 4.2: sTISSUE architecture and hardware. **(A)** sTISSUE is composed of individual cells, each containing a hydraulically amplified self-healing electrostatic (HASEL) actuator, a magnetic displacement sensor, plus a driving circuit and voltage sensor. **(B)** Groups of 10 cells are organized into modules which share a high voltage (HV) power source and coordinate control and sensing using the DCU and SCU microcontrollers. **(C)** Modules combine together to form sTISSUE. A continuous soft silicone skin interacts with the external environment. A personal computer (PC) and AC/DC power respectively supply control and power to every module. **(D)** Signal architecture for sTISSUE. The module level controls each cell using the magnetometer input. The cell level controls the voltage of each HASEL actuator using the HV driver and sensor.

the shape display which acts as the interface between sTISSUE and the world. A central AC/DC power supply uses a standard 120 V AC wall outlet to supply all power to each module (Fig. 4.2D). A personal computer (PC) interfaces with the DCUs and SCUs on all 10 modules via USB ports (Fig. 4.2D). The PC receives cell voltage measurements from each DCU and magnetometer measurements from each SCU and computes control inputs on a global level for all 100 sTISSUE cells (Fig. 4.2D). The PC also logs and stores experimental data and acts as a user interface through keyboard inputs. The unactuated footprint of each sTISSUE cell (including module level hardware) is 6 cm x 6 cm with a 9 cm height.

4.2.2 High-bandwidth electrohydraulic actuation and control

sTISSUE is driven by HASEL actuators, electrohydraulic soft actuators capable of high-bandwidth actuation up to 20-100 Hz [64, 88]. Each HASEL actuator consists of a stack of 12 fluid-filled pouches with electrodes on both sides which transduce HV to strain (Fig. 4.3A). The actuator has a 6 cm x 6 cm footprint. Using a motion capture marker system (see Materials and Methods), the displacement of each HASEL actuator is measured with high accuracy and precision at 240 Hz. On a single-cell level, the typical voltage-to-displacement relationship of the HASEL actuator (Fig. 4.3B) is generally linear above 2 kV with two caveats: (1) hysteresis results in a different relationship when the voltage is decreasing versus increasing, and (2) the retention of small amounts of charge on the film of the actuator results in a small decrease in stroke over multiple cycles [88]. The maximum HASEL actuator stroke is approximately 12 mm, but because each actuator is primarily fabricated by hand (see Materials and Methods), the maximum stroke can vary across the sTISSUE array.

High frequency independent voltage regulation is necessary to control the displacement of each actuator in sTISSUE. This is accomplished through a pair of optocouplers in each cell. Each optocoupler consists of a low voltage light emitting diode (LED) and a HV photosensitive diode which are optically coupled; light emitted from the LED onto the HV diode causes current to flow through the diode. The "charging optocoupler" allows current to flow to the HASEL actuator electrodes and the "draining optocoupler" sinks current to ground (Fig. 4.3C). This approach has been successful for voltage regulation of electrostatic actuators [88, 173, 174]. We add an integrated voltage divider (Fig. 4.3C) to measure the voltage of each actuator, enabling independent

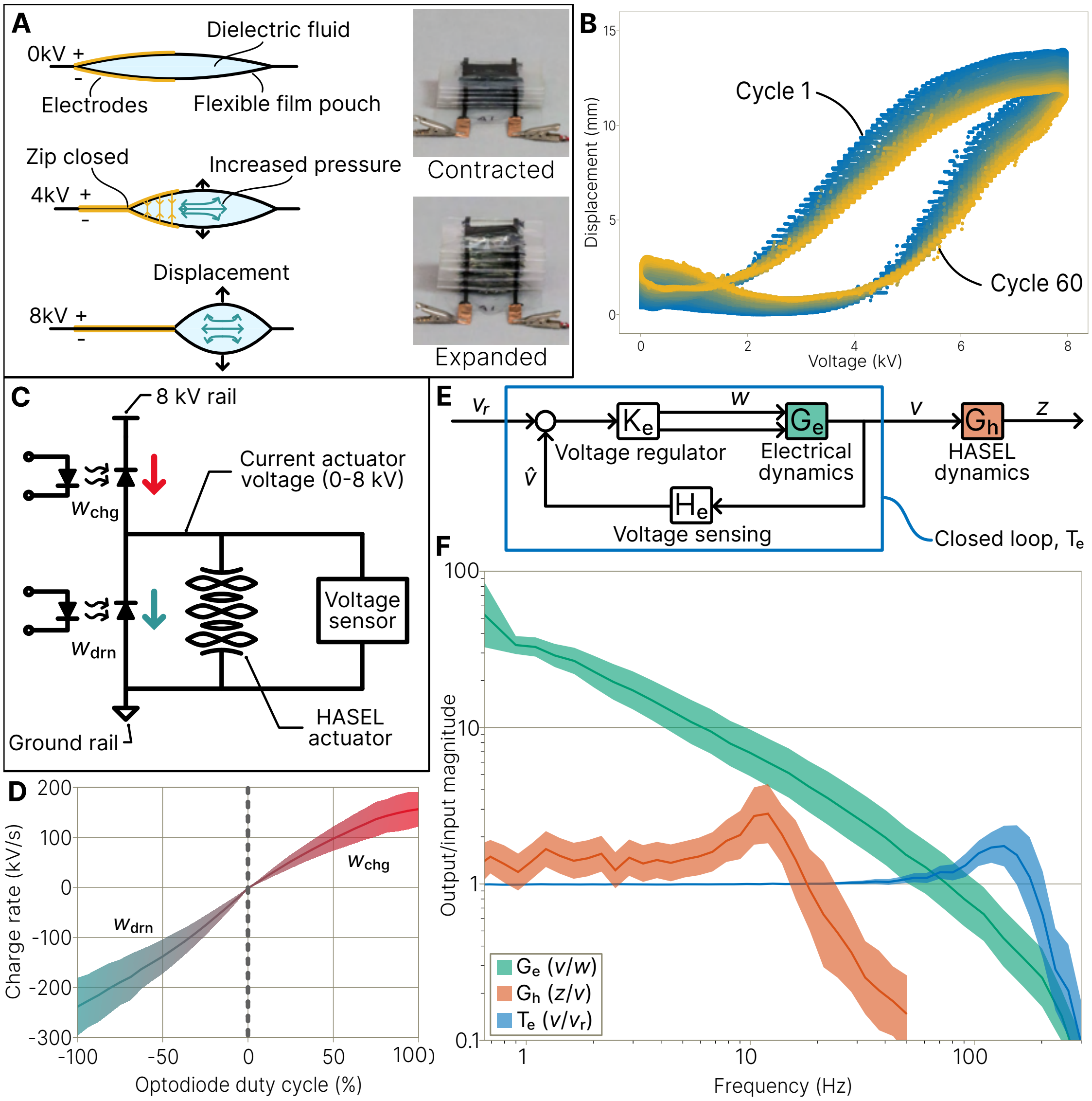

Figure 4.3: Actuation characteristics of an sTISSUE cell. **(A)** Left: basic dynamics of a HASEL pouch. Application of high voltage (up to 8 kV) results in displacement. Right: a stack of pouches builds a linearly expanding HASEL actuator. **(B)** The voltage/displacement relationship for a typical HASEL actuator over 60 cycles. **(C)** The circuit to drive the actuator contains a charging optocoupler (w_{chg}), draining optocoupler (w_{drn}), voltage sensor, and HASEL actuator. The 8 kV HV rail and ground rail are shared among all cells in a sTISSUE module. **(D)** Relationship between input duty cycle and charge rate on the HASEL actuator. Negative charge rates are controlled by wdrn, positive charge rates by wchg. **(E)** Block diagram of the HASEL actuator voltage regulation loop. The electrical dynamics, HASEL actuator dynamics, and the voltage closed loop (from v_r to v) are key dynamical systems which are characterized. **(F)** Frequency response of the three dynamical systems on each of 100 cells. The closed loop voltage regulator has a mean bandwidth of approximately 200 Hz while the open loop HASEL actuator response has a 30 Hz bandwidth, providing sufficient control authority. For both (D) and (F), the shaded areas represent +/- 1 standard deviation; the solid line is the mean response at each frequency.

closed loop voltage control. The duty cycle of the pulse-width modulation (PWM) signal on each optocoupler (w_{chg}, w_{drn}) can be varied to change the impedance of the HV diode.

The DCU on each module uses dedicated ADC pins for each cell to measure the voltage divider and set the charge and drain PWM duty cycles. The relationship between duty cycle and charge rate (Fig. 4.3D) is roughly linear, allowing for linearized control analysis. The relationship between the low voltage ADC signal (v_{raw}) and the estimated HASEL actuator voltage $\hat{v}$ (kV) is also a linear relationship of

$$\hat{v} = v_{raw}/102.82. \tag{4.1}$$

The system dynamics of voltage regulation are primarily driven by the electrical dynamics $G_e(s)$ (Fig. 4.3E) which lumps the dynamics of the optocouplers, HASEL actuator, and voltage sensor (Fig. 4.3C). We assume that the voltage sensor has unity gain, $H_e(s) = 1$.

The open loop frequency response of the electrical dynamics was characterized through a series of sinusoidal input/output tests performed across all 100 cells (see Materials and Methods). A key aspect of the characterization and control is that only one optocoupler is controlled at a time, simplifying the dynamics to a single-input system (see Eqs. (4.7)-(4.8)). The experimentally derived relationship between the input duty cycle to the optocoupler pair, w (where 100% duty cycle = 1), and the output voltage v (kV) is

$$G_e(s) = \frac{293.58}{s}. \tag{4.2}$$

The open loop system acts as an integrator on actuator voltage. Using loop shaping techniques, we designed a controller with zero steady state error, <10% error below 10 Hz, <20% error below 20 Hz, and disturbance rejection of 1/10 at 200 Hz (see Materials and Methods). The controller was implemented on each DCU in a 600 Hz loop using a zero-order hold (ZOH) discretization. The controller runs independently for each cell in the module.

The closed loop response $T_e = G_eK_e/(1 + G_eK_e)$ of the voltage regulation shows a -3 dB bandwidth above 200 Hz across all 100 cells (Fig. 4.3F), much higher than the bandwidth of the actuators. The result is a controller which can rapidly and accurately modulate the voltage of the HASEL actuator in every sTISSUE cell. This rapid voltage modulation enables sTISSUE to achieve

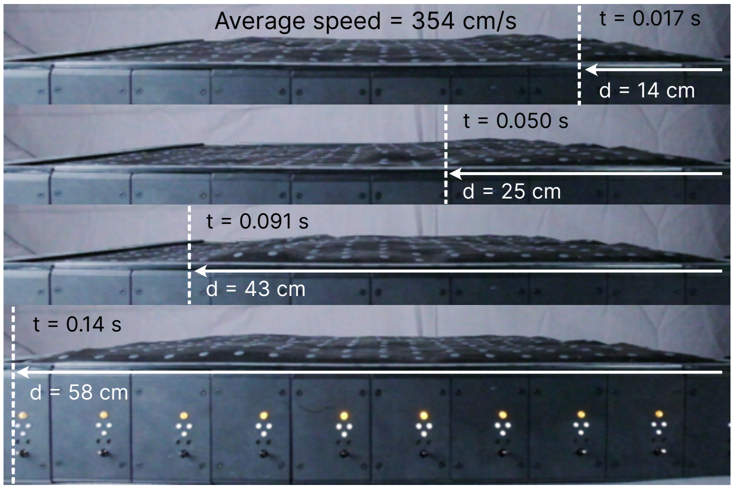

Figure 4.4: High frequency actuation enables transverse waves to travel 'across' the sTISSUE surface with a measured speed of 354 cm/s. These transverse waves can be used to manipulate objects and transfer energy.

dynamic surface motion in our model shape display. Using the motion capture displacement data as the output and the regulated (closed loop) voltage as the input, we characterized the open loop frequency response of all 100 HASEL actuators within sTISSUE. On average the actuators can vibrate at the millimeter scale at up to 40 Hz, with a bandwidth of 20 Hz for actuation above 1 mm (Fig. 4.3F). This high-speed motion enables the sTISSUE to generate transverse traveling waves with speeds up to 354 cm/s (Fig. 4.4).

4.2.3 Distributed displacement and force sensing

In addition to high-speed actuation, sTISSUE contains sensors embedded in each cell which enable distributed displacement and force sensing across the entire material. Just as each HASEL actuator transduces voltage to displacement, the magnetic block and magnetometer combination transduces displacement to magnetic flux (Fig. 4.5A). When the HASEL actuator expands, the magnetic block is lifted, and the magnetometer registers a change in magnetic flux density. The sensors in each 10-cell module are daisy-chained together using a single SPI connection with the SCU. The SCU collects the 10 sensor measurements in sequence and transmits the data to the central sTISSUE computer via USB. The entire 10x10 sensor array is sampled by the sTISSUE computer at 600 Hz. A third-order polynomial mapping

$$\hat{z} = p_3 B_z^3 + p_2 B_z^2 + p_1 B_z + p_0 \tag{4.3}$$

maps from the raw magnetometer sensor reading B_z (mG) to the estimated HASEL actuator displacement $\hat{z}$ (mm). A digital first-order 50 Hz low pass filter is added to the magnetic data sampled on the computer to reduce sensor noise. Because of variations in the magnetic flux density between sTISSUE cells, the coefficients $p_0, ..., p_3$ are unique to each cell. Using the motion capture system, we performed a calibration test to generate the polynomial coefficients for the displacement map on each cell (see Materials and Methods). The calibration remains accurate as long as the magnetic blocks on top of each HASEL actuator do not shift position. Compared to the true HASEL actuator displacement, the mapped displacement measurement from the magnetometer has an error within 0.3 mm (Fig. 4.5B). A frequency response characterization shows that the magnetometers maintain consistent accuracy at higher actuation frequencies (Fig. 4.5C).

In addition to displacement sensing, each cell is also capable of sensing force by utilizing both the magnetometer and voltage sensor embedded in the cell (Fig. 4.5D). When an external force f is applied to a cell while the actuator is active, the height of the HASEL actuator will decrease without a corresponding decrease in voltage. A 15-degree polynomial (Eq. (4.6)) maps from the measured voltage and this sensed height to estimate force (Fig. 4.5E).

When combined amongst all 100 cells, this forms a sensor array capable of distributed height mapping (Fig. 4.6A). It is able to sense rapid deformations with resolution limited only by the number of cells. This results in an additional capability of surface force measurement (Fig. 4.6B). Due to the soft and continuous nature of the sTISSUE, forces applied between two adjacent cells are sensed and averaged across the cells, enabling a continuous mapping from the discrete array. The force mapping uses the sensitivity of the magnetometers and voltage sensors, resulting in a 50 mN resolution (Fig. 4.7).

4.2.4 Surface shape control through feedback

We implemented closed loop feedback on the displacement of each sTISSUE cell using the magnetometer displacement mapping $\hat{z}$. Like our approach to closed loop feedback of HASEL actuator voltage, we first performed open loop system identification using a series of sinusoidal inputs (see

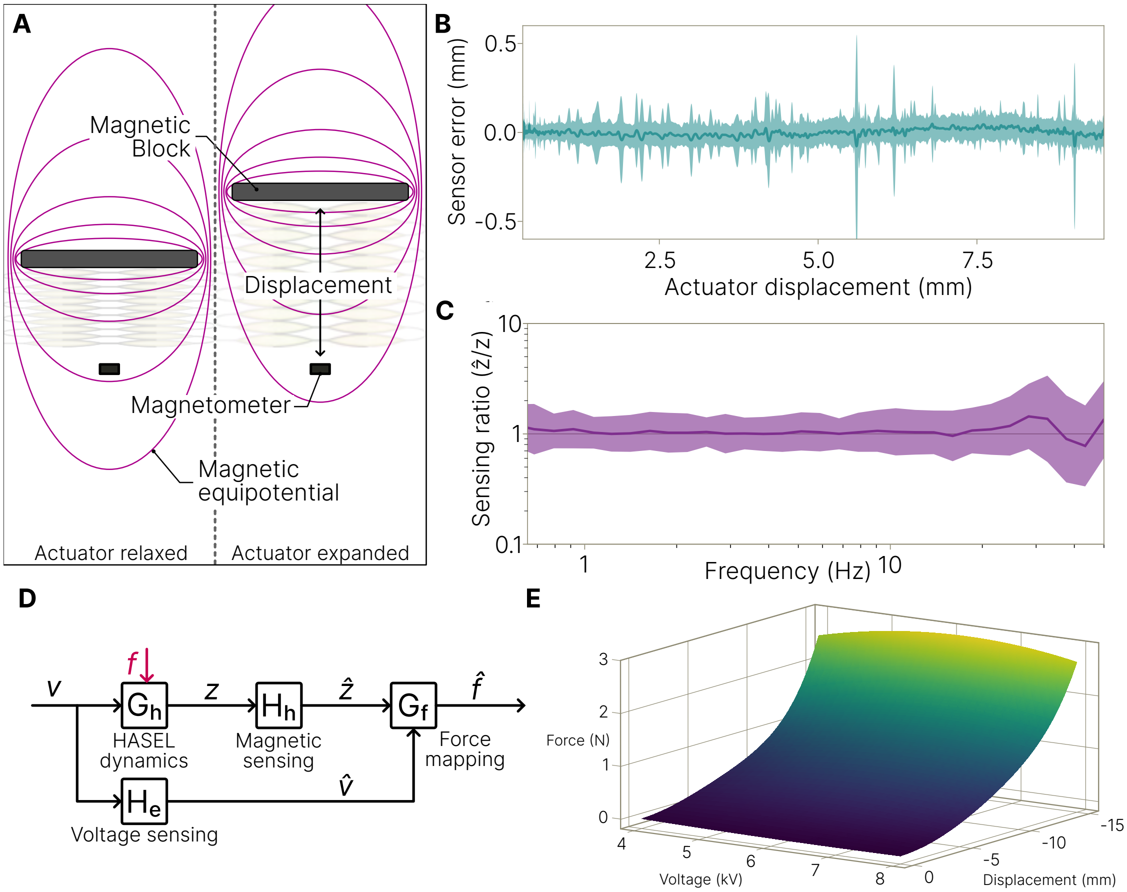

Figure 4.5: Embedded surface sensing on an sTISSUE cell. **(A)** Soft magnetic blocks on top of each actuator generate a magnetic field. Displacement of the actuators results in a change in magnetic flux density measured by the magnetometer. A third-order polynomial maps from the magnetic flux to displacement. **(B)** Mapping error between the measured and true actuator displacement across 100 cells. The shaded area is +/- 1 standard deviation, the solid line is the mean. The mean error is 0 mm with a standard deviation within 0.3 mm. True displacements are measured with a motion capture camera system (see Methods and Materials). **(C)** Frequency response ratio between the true and measured displacement of all 100 cells from sinusoidal actuator inputs. The shaded area is +/- 1 standard deviation, the solid line is the mean. The sensors reliably track cell motion up to 50 Hz. **(D)** By combining magnetic sensor and voltage sensor signals with a force mapping G_f, each cell can also measure applied force. **(E)** The 15th order polynomial G_f maps from displacement and voltage to an estimated force.

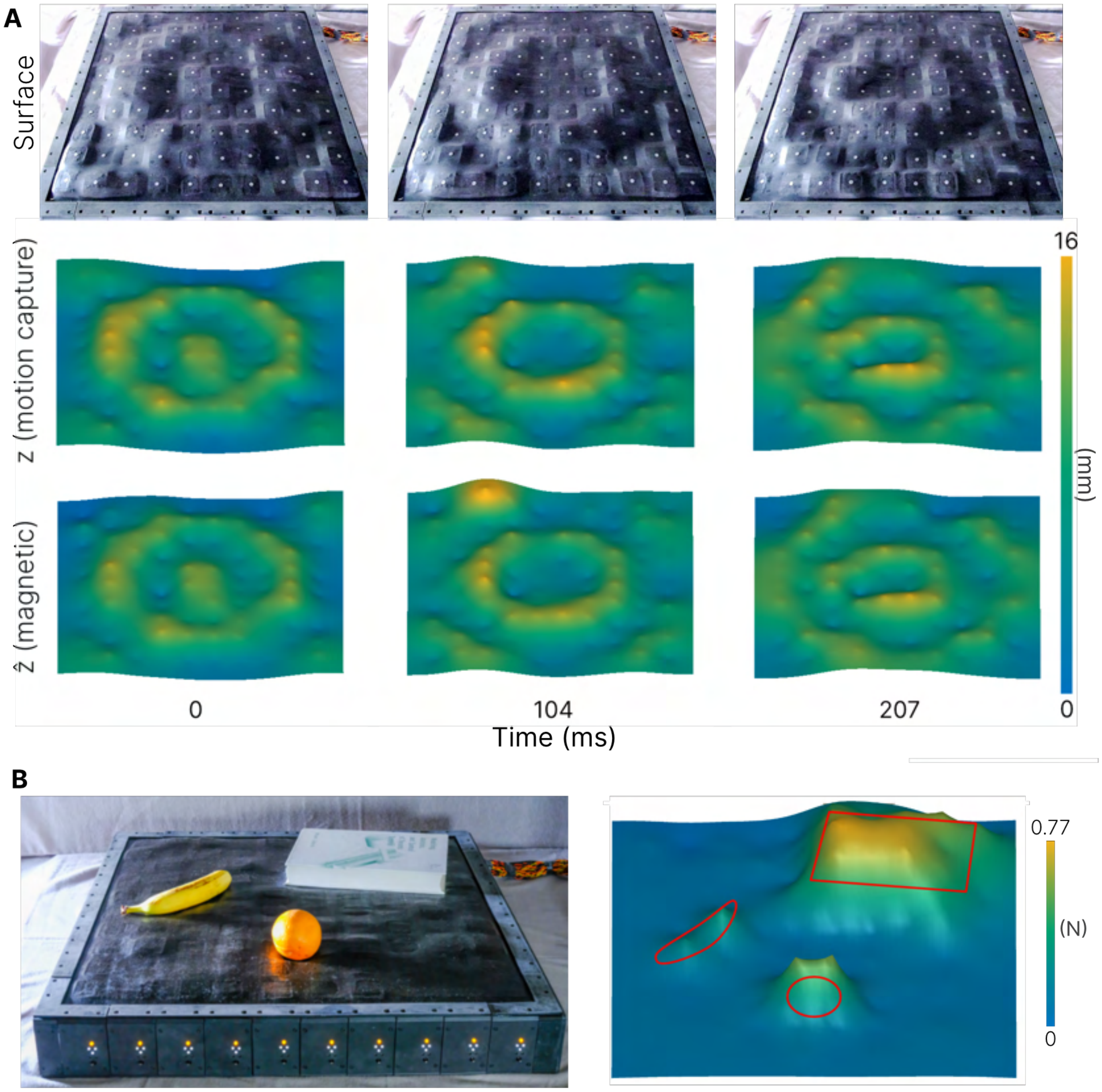

Figure 4.6: Embedded surface sensing using the full 10x10 sTISSUE array. **(A)** Time history comparing actual photographs with both the true and measured surface displacements for a 2 Hz surface ripple. **(B)** Force sensing demonstration. Objects placed on the surface are detected and mapped to estimated forces using the mapping in Fig. 4.5E.

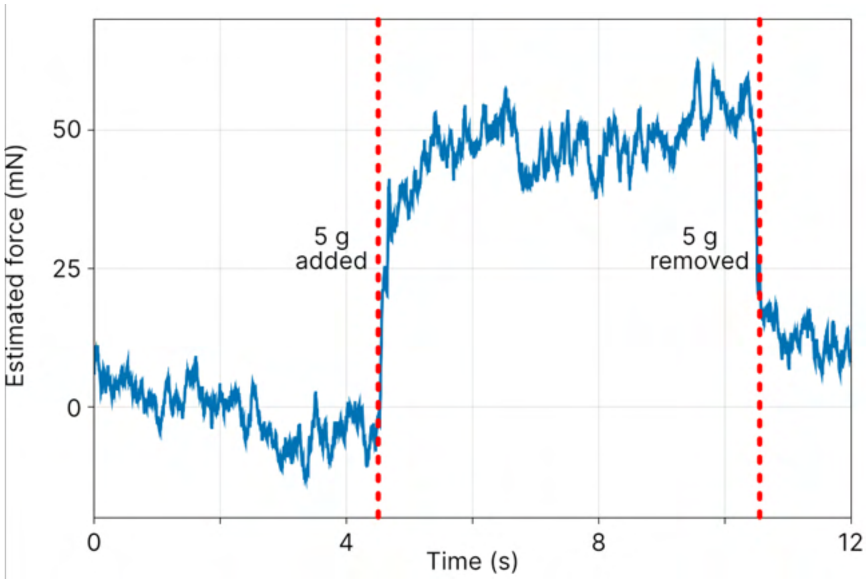

Figure 4.7: Force resolution of an sTISSUE cell. Using the 15-degree polynomial (Eq. (4.6)) to estimate the applied force, a single cell can easily detect a 5 g mass (50 mN force) applied to the surface.

Materials and Methods). In this case, we consider the inner loop HASEL actuator voltage regulator T_e as a fixed component of the open loop height transfer function (Fig. 4.8A). The input signals are thus voltage references v_r (kV) sent to the DCMU for the inner voltage loop, and the output signals are HASEL actuator heights h (mm) measured from the motion capture cameras. Given the voltage regulator dynamics have unity gain below 100 Hz (Fig. 4.3F), we assume $v = v_r$. The estimate of the open loop transfer function from HASEL actuator voltage v to displacement z (Fig. 4.8A) is

$$G_h(s) = 0.014 \frac{(24\pi)^2}{s^2 + 12\pi s + (24\pi)^2} \tag{4.4}$$

where π is the mathematical constant, giving a natural frequency of 12 Hz. Using the same loop shaping approach used to generate the inner voltage loop controller (see Methods and Materials), we designed a controller with zero steady-state error, <1% tracking error below 1 Hz, <10% error below 10 Hz, <20% error below 20 Hz, and disturbance rejection of 1/10 at 200 Hz. The controller was discretized using a ZOH at 200 Hz.

Unlike the inner loop voltage regulator, which is implemented directly on the DCU in each module, the outer loop displacement controller is implemented on the PC (Fig. 4.2C). From the

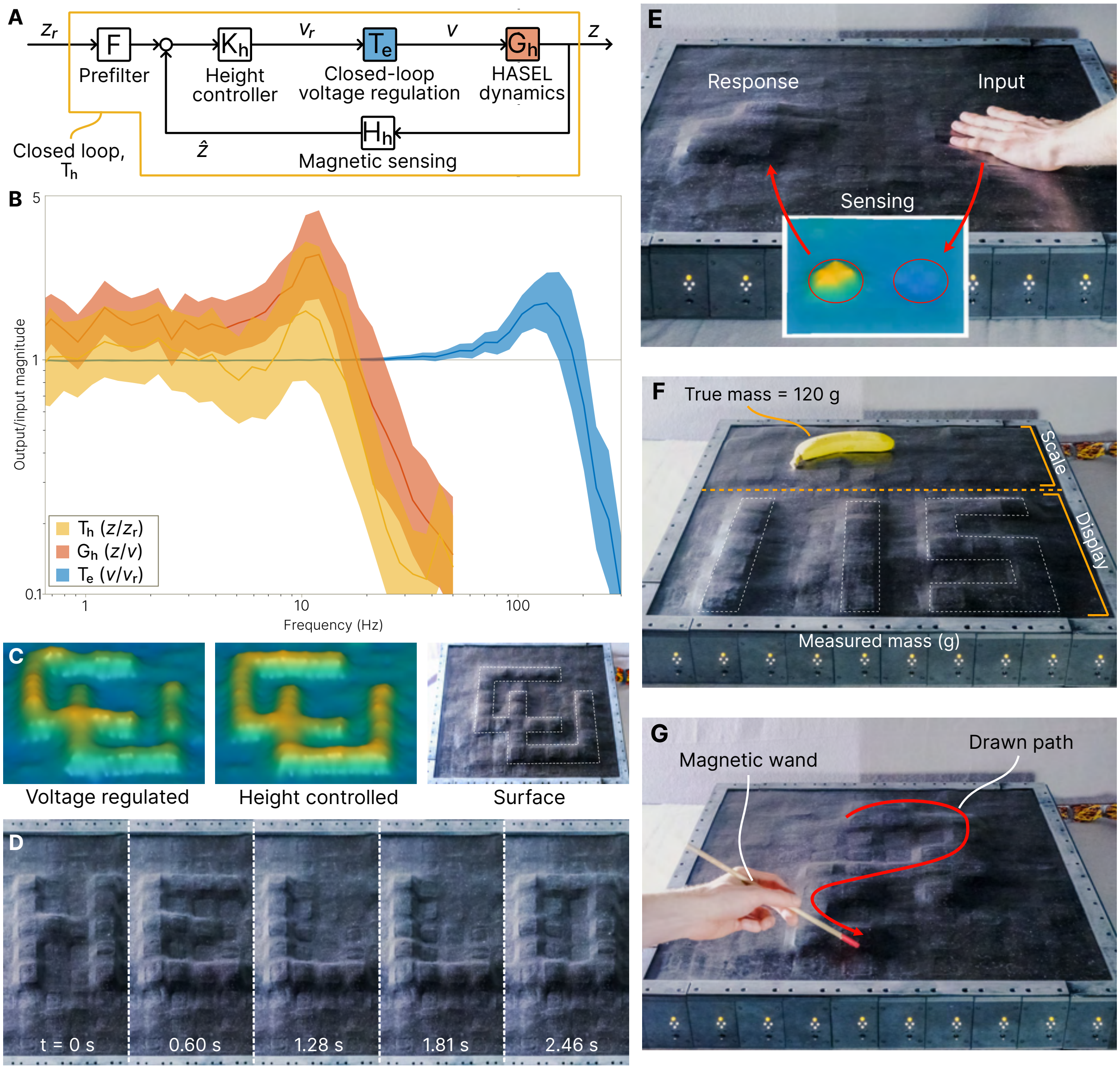

Figure 4.8: Closed loop control of sTISSUE. **(A)** Block diagram of the displacement dynamics and closed loop feedback of each cell. The closed loop voltage regulation Te is the loop in Fig. 4.3E. **(B)** Frequency response of the HASEL actuator dynamics, closed loop voltage regulation, and closed loop on displacement across 100 cells. The shaded area is +/- 1 standard deviation, the solid line is the mean value. The performance of the height controller is limited to 20 Hz due to the actuator dynamics. **(C)** Implementing the closed loop controller results in height uniformity across surface shapes compared to only voltage regulation. Here, the University of Colorado "CU" logo is plotted on the surface. **(D)** closed loop control enables an application of high-speed scrolling text across the sTISSUE surface. **(E)** Embedded sensing enables feedback from external stimuli. Here, displacements on one side of the array are converted to actuation on the other side. **(F)** Combining (D) and (E) results in an intelligent scale which can both sense forces and display the resulting estimated mass using displacement control. **(G)** The magnetic sensors also enable the use of peripheral devices, like a magnetic-tip wand which can draw shapes using active cell actuation.

PC, a user can input reference displacements z_r. The PC receives magnetometer readings from the SCU in each module, maps and filters the readings, generates an error $z_e = z_r - \hat{z}$, computes the desired voltage inputs v_r for each cell, and sends the voltage inputs to the DCU in each module where the inner loop voltage regulation occurs. The 100 separate displacement loops (one for each cell) run asynchronously and the control outputs are automatically grouped into the appropriate sets of 10 to be sent to each module via USB.

Using the embedded magnetic sensing in each cell for loop closure enables sTISSUE to achieve global displacement control with disturbance rejection. This not only rejects actuator disturbances like charge retention (Fig. 4.3B), but external disturbances applied to the sTISSUE surface. Comparison between the ground truth motion capture data and the magnetometers show that the sTISSUE surface can maintain static shapes with a mean cell displacement error within 0.3 mm (Fig. 4.8C). sTISSUE can also create dynamic, time-varying surfaces like scrolling text (Fig. 4.8D).

The embedded sensors also enable additional interactive functions using sTISSUE. The surface can apply force sensing to detect external stimulus and mirror the input as an actuator response (Fig. 4.8E). The text display ability and force sensing ability can be combined to create an interactive scale which displays an objects mass in real time (Fig. 4.8F). Because of the high frequency of both sensing and actuation, this allows sTISSUE to act as a high-refresh-rate force display. The magnetic sensors also enable use of peripheral devices. For example, the movement of a magnetic-tip wand will be detected across the sensor array, which can be converted into a topological height map – allowing a user to interactively draw on the sTISSUE surface (Fig. 4.8G).

Object manipulation with a peripheral sensor

Like other shape displays [107,110–112,120,122,175], our shape display built from sTISSUE is also capable of complex object manipulation on its surface. This is a unique ability of such devices to transform vertical actuator displacement into lateral motion of an object. Rolling spheroids is a useful demonstration of this ability with applications to manufacturing, object conveying, and sorting [122]. In comparison to rigid actuator arrays [122,164], the continuous soft surface layer of sTISSUE allows for object rolling without concern of gaps or discontinuities along the interface. In turn, this enables manipulation of objects with a diameter smaller than the cell diameter (6 cm). In addition, the natural compliance of the surface and its underlying actuators increases surface contact with objects, enabling greater traction and continuous spatial manipulation. The high bandwidth of the sTISSUE allows for rapid positional control and reaction to disturbances such as surface irregularities.

To demonstrate object manipulation on the sTISSUE we implemented a closed loop feedback algorithm (Fig. 4.9A) on the spatial position of a ball: $\boldsymbol{x}_{ball} = (x, y)$ with surface coordinates x and y ranging from 0 to 10 corresponding to each sTISSUE cell. The basis of this control is the local deformation of the surface at the ball's position. Using a 2D semicircle shape with a Gaussian side profile (an "arced Gaussian", Fig. 4.9B), a concave channel is created along which the ball can roll; deforming the surface creates a gradient which the ball rolls down to create motion. The algorithm and surface shape are further described in the Methods and Materials.

In addition to our model sTISSUE system – the 10x10 shape display – a 260 FPS USB color camera (2.9 mm Wide Angle, ELP) is placed 115 cm above the surface pointed downwards to image the entire sTISSUE surface. The camera is mounted to an aluminum (80/20 LLC) frame. The camera measures ball position and can identify multiple balls based on color. The external camera was used instead of the embedded force sensing to measure ball position. This was done because the force sensing modeling is quasi-static, so it is difficult to sense the ball position when the surface is actively deforming. We demonstrate positional control of a ball using sTISSUE surface deformation, first by moving a table tennis ball through a series of 4 waypoints, resulting in a square trajectory (Fig. 4.9C), and then by rolling three balls onto the surface and simultaneously sorting them into separate regions based on ball color (Fig. 4.9D). Each experiment was repeated 25 times.

For the square trajectory sequence, the ball trajectory over 25 trials is typically within 1/2 pixel of the desired trajectory, an error of 3 cm. The spread of trajectories has a width of about 1 pixel (Fig. 4.9E), which is the upper performance limit before the control problem becomes underactuated. Qualitatively, the set of trajectories maintains the desired square shape. For the color sorting experiment, the different-colored balls are all correctly sorted to their goal positions for all trials (Fig. 4.9F). Because each ball during each trial has an initial velocity on the surface, it is more susceptible to surface irregularities, resulting in a larger spread of trajectories than the single-ball experiment. The experimental methods are described in Materials and Methods.

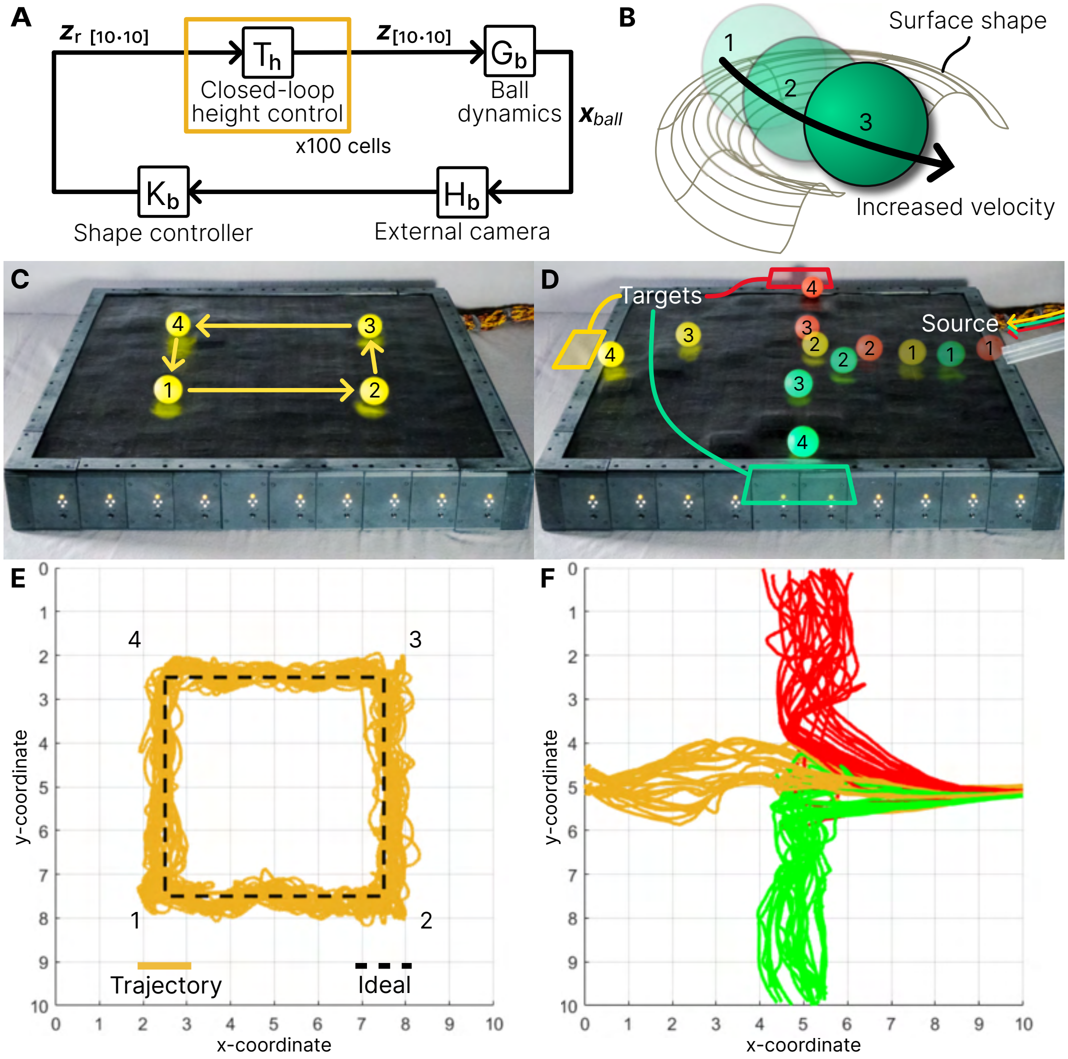

Figure 4.9: Object manipulation using sTISSUE. **(A)** closed loop control is achieved by integrating an external camera for ball detection and an algorithm to generate a driving surface shape (see Methods and Materials). The controller generates a 10x10 matrix of displacements which corresponds to the displacement of each cell in closed loop control. **(B)** Desired surface shape to induce ball motion. The direction of the surface shape opening dictates the ball direction. **(C)** Planned motion sequence for a single ball on the surface. **(D)** Planned motion sequence to sort three balls by color. **(E)** Trajectories of 25 trials for the single ball. Each trial reaches each waypoint in an ideal straight line. **(F)** Trajectories of 25 trials for sorting three balls by color.

4.3 Discussion

Here, we presented the design, performance quantification, and capabilities of a scalable electrostatic soft robotic material (sTISSUE) which integrates actuation, sensing, communication, and control. Specifically, we discussed the hierarchical design of both the hardware and control architectures

(Fig. 4.2) and how this structure reduces complexity. Sharing computation and power with multiple cells in each module decreases the number of HV amplifiers and microcontrollers required and allows for faster communication with the central PC. This is an ideal balance between having one microcontroller for each cell (more costly and computationally expensive) and having a single microcontroller for the entire 10x10 array (cheaper and simpler but with slower sensing and control due to the additional multiplexing and computation that would be required). In addition, the nested control structure with both voltage and displacement loops enables robustness in sTISSUE shape control because inner loop discrepancies can be handled by the outer loop.

This design allows the single sTISSUE cell to be repeated in a 10x10 array without an impact on performance. Multi-threaded software allows the central computer to asynchronously maintain two-way communication with all ten modules at 1200 Hz while simultaneously running displacement control loops, decision logic, parsing user input, and collecting data. Each SCU and DCU runs a loop frequency of 600 Hz. Overall, this means that the physical dynamics of the actuators and the optocoupler control system (Fig. 4.3C-D) are the slowest components of the material. From a control perspective, there is no additional complexity to controlling the displacement of all 100 cells compared to a single cell. The closed loop dynamics are also consistent between one and 100 cells (Fig. 4.8B).

sTISSUE is also robust to failures. On any given cell, a HASEL actuator can partially fail due to an electrostatic discharge (arcing), but the HV driver can still enable motion. If the actuator or driver fails completely, then this ‘dead pixel’ only impacts 1% of the overall surface motion of our model sTISSUE system and can easily be replaced. In addition, a magnetometer failure would prohibit use of the displacement feedback controller (Fig 5A), but a cell can still operate on voltage regulation alone (Fig 3E) to drive approximately accurate motion. At the module level, the failure of an SCU, DCU, or HV amplifier will only affect the cells in the given module instead of the entire material and can also be replaced. The only systems that can impact the entire sTISSUE material are the PC and the power supply, creating a robust soft robotic material.

The dynamic capabilities of sTISSUE enables the multifunctionality shown in Fig. 4.1 and Fig. 4.8. Coordinated motion of the actuators using feedback from the magnetic sensors enables rapid (30 Hz) motion which can interact on both small and large objects. The high actuation frequency and continuous surface skin enables vibrational outputs which can be used to interact

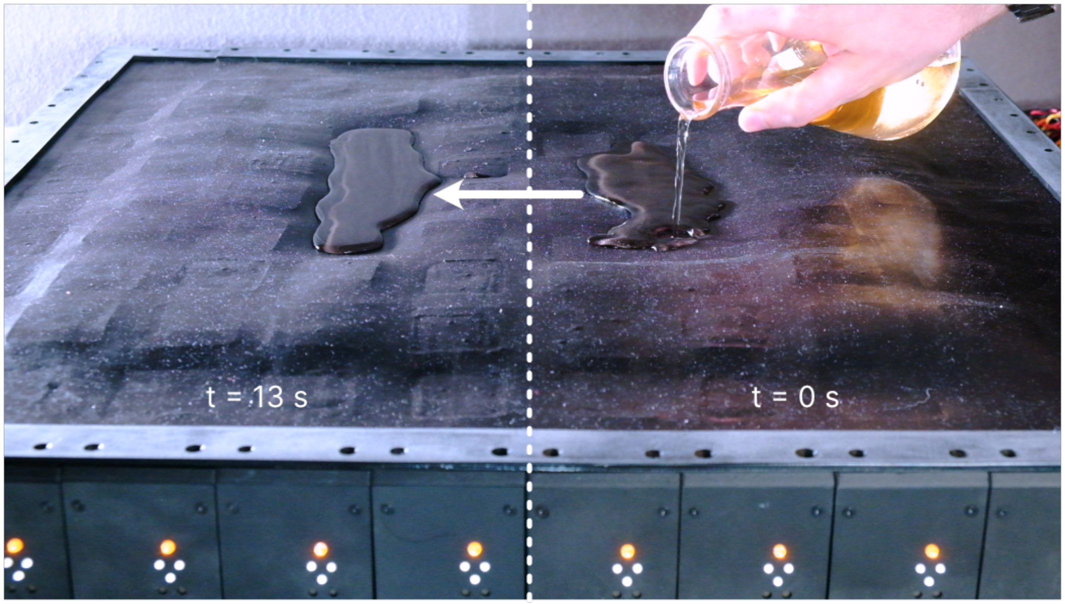

Figure 4.10: sTISSUE liquid manipulation. By creating a 'basin' in which a pool of water can rest, sTISSUE can move the liquid across the surface.

with liquids, capabilities normally not achievable with soft systems (Fig. 4.10). The sensor array also enables a wide variety of user and object interactions (Fig. 4.8). Because the sensors are capable of both displacement and force sensing, multiple functionalities are simultaneously possible such as an active scale (Fig. 4.8F), which combines an external force sensing and text display function. Such functions can also be implemented in local sections of sTISSUE – for instance, one 5x5 quadrant can be used to manipulate objects, another can sense and react to forces, a third quadrant can actuate the surface to a static shape, and the fourth can actuate a high frequency function. The distributed actuation, sensing, and control of sTISSUE allows these modalities to be implemented simultaneously (Fig. 4.1B).

4.3.1 Comparison with other actuator arrays

Designing a large scale smart robotic material is a significant challenge that requires trade-offs between performance, system integration, and scalability. Most systems presented in literature satisfy certain goals but at the expense of other desired characteristics. There have been a wide range of actuating arrays with various sizes and diverse applications. Tables 4.1-4.2 broadly summarize two types of actuator arrays with a comparable displacement (stroke) to sTISSUE actuators: macro-scale (cm-range max stroke) and meso-scale (0.1 to 10 mm max stroke).

Table 4.1: Comparison of sTISSUE technical characteristics with other systems in literature. The 10x10 sTISSUE array demonstrates high bandwidth, moderate stroke, and a large number of actuators. Bandwidth for some systems is reported as -3 dB output/input; for other works, only the maximum frequency achieved is reported. DE: dielectric elastomer, LCE: liquid crystal elastomer, IPMC: ionic polymer-metal composite, SMP: shape memory polymer.

	Technical characteristics				
Source	**Actuation**	**Number of actuators**	**Cell dimension (mm)**	**Bandwidth (Hz)**	**Max stroke (mm)**
This work	HASEL	100	60 x 60 x 90	20	12
[176, 177]	Pneumatic	12	15	∼1	8
[107]	Pneumatic	216	52 x 52 x 115	∼1	20
[178]	Pneumatic jamming	12	∼40 x ∼40	0.5	∼32
[179]	DE	12	2.4 x 2.4 x 9	60	-
[110]	DE	16	∼60 x ∼60	< 2	∼13
[172]	DE	9	∼5 x ∼5	∼250	3
[167]	DE	16	23 x 23 x 13	∼3	∼0.5
[113]	LCE	48	∼20	< 0.1	-
[166]	DE	6	5 x 5 x 2	∼4	0.33
[180]	IPMC	25	-	∼1	0.15
[181]	Pneumatic	6	2.5 x 2.5 x 52	∼30	∼0.6
[165]	SMP-pneumatic	768	4 x 4 x 2	< 0.1	2
[182]	IMPC	144	1 x 1	< 1	∼0.5
[183]	Combustion	9	3 x 3 x ∼2	10	3-5
[122]	Motor	900	3 x 3 x 1100	∼10	100
[184]	Motor	18	∼100 x ∼100	-	-
[185]	Hydrogel	4320	0.3 x 0.3	< 1	0.5
[164]	Motor	288	4.85 x 4.85 x 273	-	50

Table 4.2: Comparison of sTISSUE features with other systems in literature. While various works combine multiple features together, only sTISSUE integrates all five of the highlighted features into a single system.

	Features				
Source	**Soft**	**Driver integration**	**Embedded state sensing**	**Closed loop control**	**Scalability**
This work	✓	✓	✓	✓	✓
[176, 177]	✓		✓	✓	
[107]	✓			✓	✓
[178]	✓			✓	✓
[179]	✓				✓
[110]	✓				✓
[172]	✓		✓		✓
[167]	✓		✓		
[113]	✓				✓
[166]	✓				
[180]	✓				
[181]	✓				
[165]	✓				✓
[182]	✓				✓
[183]	✓				
[122]		✓		✓	✓
[184]		✓		✓	✓
[185]					✓
[164]		✓		✓	✓

Macro-scale actuator arrays [107, 110, 122, 164] focus on large-scale object manipulation with commercial applications like assembly lines conveyance or organize produce handling. Many existing systems are very bulky [122], requiring large and loud external components like pneumatic pumps [107], both of which make modularity and scalability a challenging task. For rigid motor-driven systems, integrating the motors and push pins results in a very tall device [164], some as tall as 1100 mm [122], while the sTISSUE integrates HV actuation and driving circuits in a 90 mm-tall package albeit with much smaller displacement.

On the other hand, meso-scale arrays are often tailored toward active braille displays or haptic feedback devices. Due to the nature of applications, these systems often demonstrate densely packed, individually addressable actuators. However, these systems are typically not portable [166, 167, 172, 176, 177] or fast [110, 165, 178, 179], often with actuator bandwidths in the 1 Hz range. Similar to most designs at the macro-scale, the existing meso-scale designs that can actuate above 10 Hz [172, 176, 177, 180] do not have integrated hardware, and only one [172] integrated an active sensing component. sTISSUE presents a significant step forward for soft robotic materials by increasing the DOF of multiple components – an increase in actuators, sensors, closed loop control, and corresponding bandwidth.

4.3.2 Limitations

While sTISSUE demonstrates high-speed actuation, sensing, and control, it possesses several limitations in its current form. The optocoupler and HV amplifier present a hardware limit on the charge rate of each HASEL actuator (Fig. 4.3D). This charge rate limitation, in addition to the natural dynamics of the folded HASEL actuator [121], limits the usable actuation bandwidth of sTISSUE to 30 Hz. The maximum displacement of each actuator also limits the possible surface shapes that can be created. However, additional displacement can be added by increasing the number of pouches within each HASEL actuator.

Another limitation of sTISSUE is the scalability of the sensor array in each 1x10 module. This stems from the SPI bus that is shared between the 10 sensors and the SCU (Fig. 4.11). Due to impedance mismatching between each sensor along the bus, the last sensor in the module (position 10) suffers from signal integrity noise. The error in data transfer necessitates the use of a filter on the last cell on each bus which slows down the responsiveness of feedback control for those cells.

With additional electromagnetic shielding to the SPI wiring or an alternative layout (multiple SPI busses), this issue could be resolved.

In general, the module-level circuitry can currently only support a maximum of 10 cells. In addition to the sensor signal integrity, dedicated pin use on the DCU and SCU limits the number of cells to 10. However, this can be addressed with pin multiplexing. Larger sTISSUE arrays beyond 10x10 will either require the use of additional modules or the implementation of the suggested improvements to expand the number of cells supported by each module. However, all other aspects of the robotic material such as communication, power, and control should be scalable to systems larger than 100 cells without any further improvement.

4.3.3 Potential applications and future work

The presented demonstrations, like object manipulation and surface control, suggest several potential applications of an sTISSUE-driven shape display. This system could be used for the dynamic sorting and conveyance of objects (Fig. 4.9), visual information display (Fig. 4.8), or interactive user device with applications in braille and haptic displays (Fig. 4.8). By interacting with liquids (Fig. 4.1, 4.10), an sTISSUE shape display can also serve as an intelligent liquid mixing and conveyance tool.

In the future, the sensor array could be improved by utilizing the three-axes capabilities of the magnetometer (currently only one measurement axis is used). Applying this additional sensor data into a sensing algorithm would enable new functions such as shear sensing along the surface and force localization [143]. This additional sensing modality could open new possibilities in reactivity and object manipulation.

In addition, modularity in cell-level integration allows for alternative geometries in actuation and sensing. For example, the parallelizable HV drivers can theoretically control any electrostatic actuator that operates between the 0-8 kV range such as a planar Peano-HASEL actuator [83]. The magnetometers also operate agnostic of the geometry of the actuator as long as actuator displacement results in a changing magnetic flux density. The ability to change the form of actuation and sensing opens new capabilities and applications for sTISSUE.

While we present sTISSUE using a planar shape display as a model device, numerous other geometries are possible with the same cell- and module-based hardware. One simple alternate topology is to alter the dimensions of the array; with simple rearrangement, a 2x50 or 1x100 sTISSUE conveyor can be created. By turning up opposite edges of the 10x10 array one can form a 3D sTISSUE cylinder. If the cells face inward, this topology could function as a peristaltic pumping device [176]; if the cells face outward, the sTISSUE cylinder could act as an intelligent self-propelled wheel [186]).

Entirely non-rectangular geometries are also possible for sTISSUE. Since there is no constraint on the physical dimensions or arrangement of cells (beyond minimum dimensions given by circuitry), any multitude of soft robot designs could be created with sTISSUE. For example, a biomimetic soft robot arm with antagonistic extension/flexion and pronation/supination actuator groups [187] could be supported by an sTISSUE module. With the existing hardware that supports 100 cells, sTISSUE could also form a 33-segment continuum manipulator [157] with independent control over each segment.

The system can also theoretically be scaled to a size larger than 100 cells by adding additional modules. Because each module operates independently, there is no increase in computational load at the single-cell level. Additional computation will be required on the PC, but with multithreaded communication and control software any negative impacts can be minimized. In addition, the current power supply, rated for 600 W, can be replaced with a higher wattage supply to accommodate additional power loads.

The overall result of sTISSUE is an intelligent, highly modular, scalable, self-actuating soft robotic material with embedded feedback and control. While we demonstrate several advanced capabilities and applications using sTISSUE as a 10x10 shape display, there are numerous other possibilities to use sTISSUE and its design philosophies to push the envelope of soft robotics.

4.4 Materials and methods

4.4.1 Hardware fabrication

The method of creating the folded HASEL actuators in this work follows the fabrication method of Mitchell et al. [88], and is the same process and materials discussed in Section 3.2.1. After the actuator is complete, a rigid circuit board is mounted to the actuator film using double-sided tape (Scotch); Conductive Carbon Glue (Pelco) is used to form a conductive bond between the film

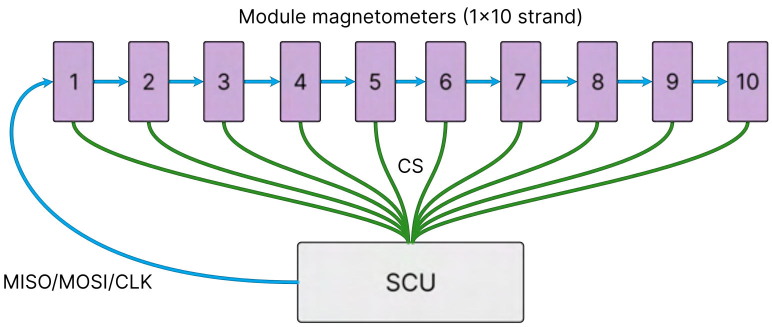

Figure 4.11: Magnetometer module topology. The MISO (Master In Slave Out), MOSI (Master Out Slave In), and CLK (Clock) signals are daisy chained between magnetometers; individual CS (Chip Select) signals run from each magnetometer to the SCU.

electrodes and the circuit board. The mounted board provides a conductive interface that mounts to the sTISSUE module hardware, connecting the HASEL actuator to the HV electronics. This process is repeated for all 100 actuators in the sTISSUE array.

The magnetic block is fabricated following a similar method to Hellebrekers et al. [148], and is the same process and materials discussed in Chapter 3. However, for this work, the mold size of each magnetic block is 42 mm x 42 mm x 4 mm. The process was repeated for all 100 magnetic blocks in the sTISSUE array.

A low cost, off-the-shelf 3-axis magnetometer (LIS3MDL, ST Electronics) on a breakout board (LIS3MDL Carrier, Pololu) was used for the magnetometer circuit. The SCU microcontroller (Teensy 4.0, PJRC) receives raw magnetic flux density data from the magnetometers via a four-wire SPI communication protocol (Fig. 4.11). The SPI clock speed was set to 1 MHz with SPI Mode 0. Since we only used the magnetic flux density measurement in one-dimension, no further calibration or algorithm was required to initialize and set-up the sensor.

The HV driver (Fig. 4.12) was commercially fabricated (PCBWay) with all surface-mount components soldered at the factory. The remaining fabrication was done by hand. Each optocoupler in the circuit consists of a low voltage infrared LED (L1IZ-0940000000000, Lumileds) and a HV opto-diode (OZ100SG, Voltage Multipliers, Inc.). To consistently align the LEDs with the photodiodes during assembly, we milled a 50x100 um slot into each photodiode, which fits over the surface-mounted LED. The two photodiodes and a HV resistor for the voltage divider were hand-soldered onto the driver board. Wires to connect the board to the HASEL actuator electrodes and

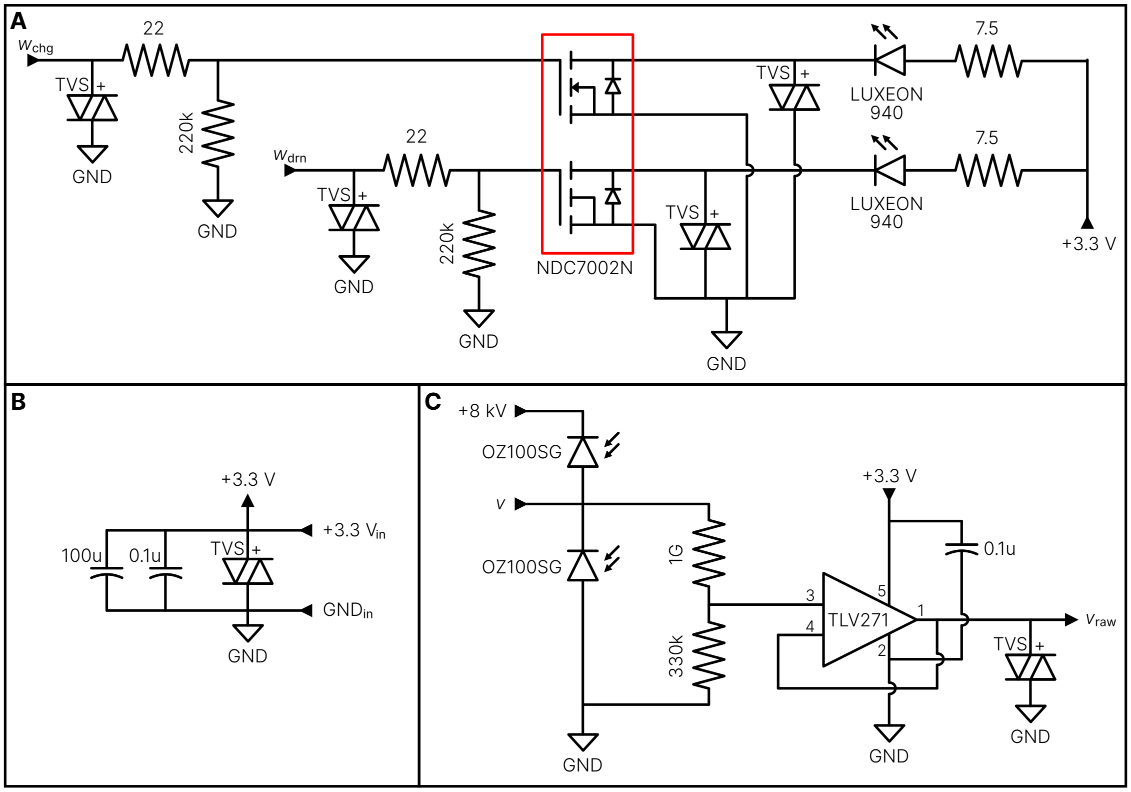

Figure 4.12: HV driver circuit schematic for a single HASEL actuator. **(A)** PWM control for the optocouplers. The infrared LEDs (LUXEON940) are optically coupled with the diodes in (C). TVS (transient voltage suppressor) diodes act as ’safety valves’ to discharge the circuit in the event of electrostatic discharge from the HV actuator. All resister values are in Ohms. **(B)** A TVS diode between the input 3.3 V and ground (GND) also helps discharge the circuit in the event of electrostatic discharge. **(C)** HV control in the circuit. The diodes (OZ100SG) receive the PWM signals from the LEDs in (A), enabling HV control of the HASEL actuator voltage v. A voltage divider driven by an op-amp (TLV271) lowers the HV signal to a scaled 3.3 V signal v_{raw} which is measured by the DCU.

to GND were also soldered by hand.

The HV components were potted in an insulating epoxy. Between the photodiode and LED, a transparent epoxy (Quickset Clear, Pratley) was used in order not to impede the function of the LED. After curing, the remaining HV components were encased in opaque epoxy (White Epoxy, Pratley).

To measure the charge rate of each HV driver in sTISSUE (Fig. 4.3D), we input a set of 16 PWM duty cycles for both w_{chg} and w_{drn}, linearly spaced from 0 – 100%. All 100 cells received the identical duty cycle simultaneously. For each duty cycle, we recorded the cell voltage as a function of time across all 100 cells. The charge rate (kV/s) was manually derived by subtracting

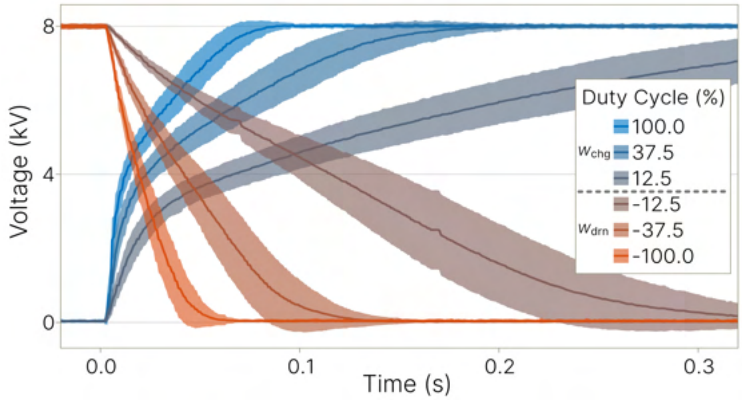

Figure 4.13: HASEL actuator voltage in each of 100 cells over time for various duty cycle %s given initial conditions 0 kV or 8 kV. Shaded areas denote +/- 1 standard deviation, the solid line denotes the mean of 100 cells. The standard deviation is smaller for higher duty cycles and is largest when draining at a low duty cycle.

the previous voltage value at each time step and dividing by the sample time (1/1200 s). The resulting data is shown in Fig. 4.3D. Additional charge/discharge time data is shown in Fig. 4.13.

The full 10x10 sTISSUE array is assembled by first assembling 10 independent modules. Each module is constructed from a series of structural components which integrate the various cell and module electronics. The structure of each module consists of a Delrin base and top plate plus 3D-printed (ColorFabb XT-CF20, Prusa MK3S) support pillars. Delrin front and side panels are also added to enclose the space. A capacitor bank of 13.2 nF is created for each module by soldering six 2.2 nF capacitors in parallel. The HV amplifier (10A24-P30, Advanced Energy), capacitor bank, DCU, SCU, and other components are placed on the base board (Fig. 4.2C) and secured with screws. The capacitor bank electrodes are connected to the HV amplifier power and ground lines. The 10 driver boards and magnetic sensor boards for each cell are screwed to the underside of the top plate. Power and communication cables are routed through the module cavity. The DCU and SCU boards were fabricated commercially (PCBWay). All electrical components were soldered by hand onto the boards.

The 1x10 modules are horizontally stacked next to each other to form the 10x10 array. On the left and right side (the 1st and 10th module), a delrin end support structure is added which helps secure the silicone skin on the top of the sTISSUE. Before full assembly, the power and ground cables are run perpendicular to each module and exit out a hole on one of the end support structures. USB cables from the DCU and SCU in each module are collected into 4 USB hubs.

Two of the hubs are daisy-chained to the remaining two, and the hub USB cables are also run out the hole in the end support structure towards the PC. The 10 modules are secured with threaded rods and nuts at the front, center, and back of each module. The power cables are plugged into a custom board which interfaces with the AC/DC power supply (ION SFX 650G, Corsair). The board connects the 3.3 V, 5 V, and 12 V wiring from the modules to the respective AC/DC outputs. For additional grounding, the ground rail of each module (from the HV amplifier) is run outside of the sTISSUE and connected directly to the building ground.

The silicone skin is fabricated by mixing 100 g part A and 100 g part B of EcoFlex 00-30 (Smooth On) with 3% by weight black Silc-Pig (Smooth On). The mixture is poured into a square frame mold on a tabletop with an area of 24.5 in x 24.5 in and left to settle to an average thickness of 550 m. To provide a matte smooth surface, we mix equal parts A and B of Psycho Paint (Smooth On), add 400% by weight of solvent (NOVOCS Matte, Smooth On), 3% by weight Silc-Pig, and spread the mixture evenly over the cured EcoFlex 00-30 surface. After drying, the silicone skin is peeled off the table and carefully stretched over the 10x10 sTISSUE array. Panels secured by screws along each edge of the array are used to secure the silicone in place.

4.4.2 Firmware and software

Both the SCU and DCU use a Cortex-M7 based microcontroller (Teensy 4.0, PJRC), programmed using the Arduino framework. Each microcontroller connects to the central PC over USB 2.0 as a HID device to ensure bounded latency communication.

The central communication and control code for the sTISSUE was implemented in Julia 1.7 [155], running on Ubuntu [21.04] (Canonical) using Linux Kernel 5.11. The code was divided between multiple functional units with information shared between each. This architecture is comparable to systems such as ROS [188], but with different design priorities. Individual functional units, such as control laws and SCU/DCU drivers, run as asynchronous tasks distributed across all 16 threads of the CPU (Ryzen 5800X, Advanced Micro Devices). Each task is scheduled at a set frequency (typically between 500 – 5000 Hz). Data is shared between tasks in a loss-tolerant, UDP-like manner using thread-safe shared memory. Data visualizations were rendered using Makie.jl [189]. For the ball manipulation experiments, Python [190] and the OpenCV [191] package were used to generate the ball position information from the USB camera.

4.4.3 Motion capture system

We used a 7-camera motion capture system (OptiTrack Prime 13W) surrounding the sTISSUE array to collect ground truth displacement data (Fig. 4.14). A circular retroreflective marker was placed in the center of each cell on top of the sTISSUE skin. With a tarp cover to initially hide the markers, the standard camera calibration was performed for the motion capture software (Motive, OptiTrack) using a wand (CS-W500, OptiTrack) and passive calibration square (CS-200, OptiTrack). A mean ray error below 0.5 mm and mean wand error below 0.2 mm are considered a successful calibration. The coordinates were set so that positive z-coordinate corresponds to an upward displacement of sTISSUE. The tarp was then removed and four markers in each corner of the 10x10 were used to recalibrate the camera ground plane, setting the average z-coordinate of the marker positions to 0. The marker data is streamed at 240 Hz through an ethernet connection to the sTISSUE PC.

4.4.4 Magnetometer calibration

To calibrate the magnetometer in each cell, the HASEL actuator in each cell was given an input voltage ramp from 0 kV to 8 kV over 8 seconds. We sampled the magnetometer reading and z-coordinate of the corresponding cell using motion capture data. The data were fed into a least-squares polynomial fitting function to generate the third-order polynomial coefficients for each cell. Because each HASEL actuator has a different displacement profile and each magnetic block is fabricated by hand, each cell has a unique polynomial fit.

However, because the sensor mapping was performed one cell at a time, inaccuracies are introduced when adjacent cells are actuated. This is because adjacent cells affect the strain on the sTISSUE skin, which changes the shape and corresponding magnetic flux of the magnetic block. To account for this, the estimated displacement $\hat{z}$ of a cell in position (i, j) in the array is modified by accounting for the proportional displacements of adjacent blocks:

$$\hat{z}_{(i,j)} = p_3 B_z^3 + p_2 B_z^2 + p_1 B_z + p_0 + \alpha \left(\hat{z}_{(i-1,j)} + \hat{z}_{(i,j-1)} + \hat{z}_{(i+1,j)} + \hat{z}_{(i,j+1)} \right) \tag{4.5}$$

The scaling factor $\alpha = 0.05$ was determined experimentally to give the best estimated displacement under all conditions. For edge cases (e.g. where $\hat{z}_{(i-1,j)}$ does not point to a valid cell), the

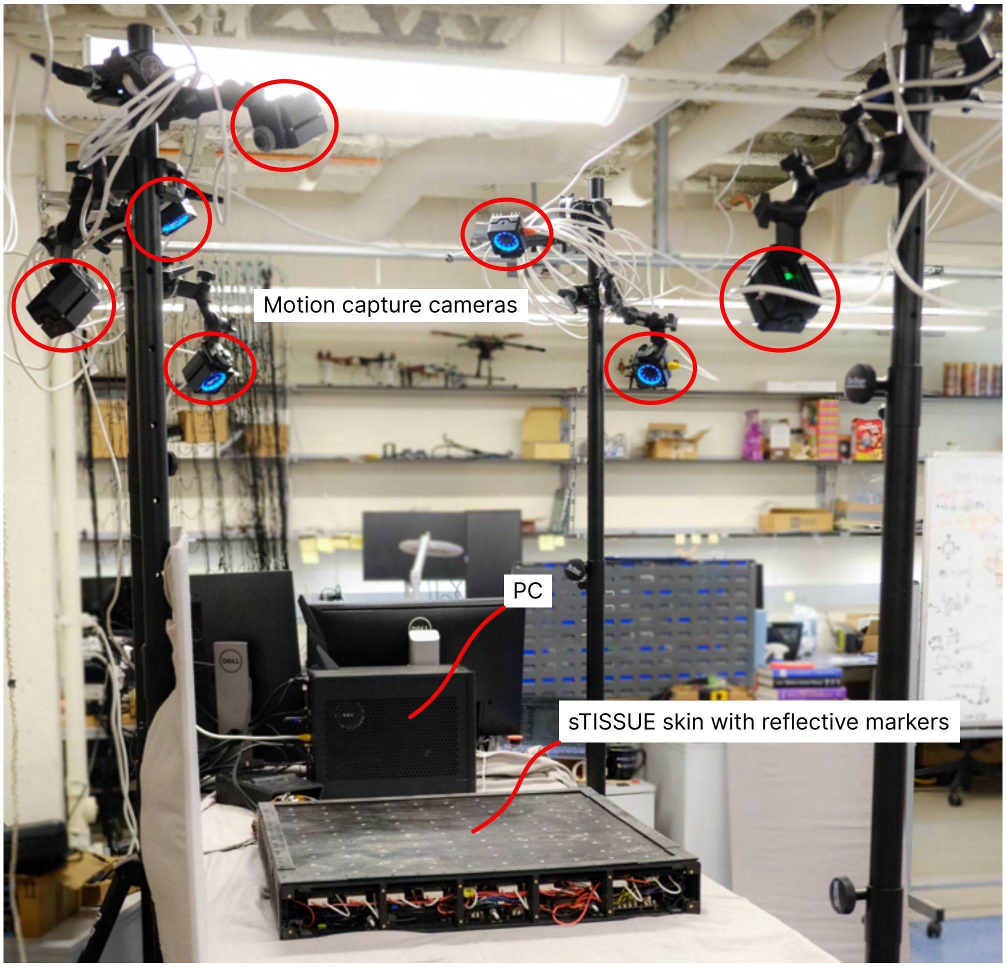

Figure 4.14: Seven-camera motion capture system used to collect sTISSUE displacement data. Each sTISSUE cell has a retro-reflective marker in its center which is detected by the motion capture software. Data is streamed to the PC via ethernet.

adjacent block value was set to 0 as there the influence of the edge surface is considered to be the 'neutral' case.

4.4.5 Force sensing calibration

A dynamic mechanical analyzer (DMA) (800E2, TestResources) was used to slowly apply incremental displacement to a HASEL actuator at a rate of 0.5 mm/s to represent a quasistatic applied force. Prior to adding the force, the actuator received a constant voltage of 4 kV and the baseline displacement was measured. The change in displacement and force were recorded from the DMA until a maximum of 25 N. This test was then repeated using constant input voltages of 5, 6, 7, and 8 kV and using three different actuators. The average data from all test actuators was used

Table 4.3: Polynomial fit parameters for magnetic force sensing.

Parameter	Value
p_0	1.854e-1
p_1	-6.493e-2
p_2	2.380e-1
p_3	4.649e-3
p_4	-9.134e-2
p_5	8.367e-3
p_6	7.572e-3
p_7	5.886e-4
p_8	3.042e-4
p_9	-8.167e-5
$p_1 0$	-2.290e-5
$p_1 1$	-5.642e-5
$p_1 2$	-1.710e-5
$p_1 3$	-1.266e-5
$p_1 4$	-7.245e-6

to determine the polynomial surface fit to map voltage and displacement to applied force. Using the MATLAB Curve Fitting toolbox (MathWorks), the data was used to generate a 15th-order polynomial fit which maps from the measured voltage $\hat{v}$ and displacement $\hat{z}$ to an estimated force $\hat{f}$:

$$\begin{aligned} \hat{f} = p_0 + p_1\hat{v} + p_2\hat{z} + p_3\hat{v}^2 + p_4\hat{v}\hat{z} + p_5\hat{z}^2 + p_6\hat{v}^2\hat{z} + p_7\hat{v}\hat{z}^2 \\ + p_8\hat{z}^3 + p_9\hat{v}^2\hat{z}^2 + p_1 0\hat{v}\hat{z}^3 + p_1 1\hat{z}^4 + p_1 2\hat{v}^2\hat{z}^3 + p_1 3\hat{v}\hat{z}^4 + p_1 4\hat{z}^5. \end{aligned} \tag{4.6}$$

The parameter values for Eq. (4.6) are listed in Table 4.3.

4.4.6 Closed loop voltage and displacement feedback

For both the voltage regulation loop (Fig. 4.3E) and displacement closed loop (Fig. 4.8A), we identified the system frequency response using a series of increasingly rapid sinusoidal inputs. For the voltage loop, we input a set of 32 sinusoidal PWM signals with input signal $w(t) = 0.1sin(2\pi f(t)t)$, with logarithmically spaced frequencies $f(t) = 0.6, 0.7339, ..., 245.6306, 300$ and time t from 0-15 s. To reduce control complexity, only one optocoupler in the HV driver was controlled at a time; the resulting relationship is

$$w_{chg}(t) = \begin{cases} w(t), & w(t) \geq 0 \\ 0, & otherwise \end{cases} \tag{4.7}$$

$$w_{drn}(t) = \begin{cases} abs(w(t)), & w(t) < 0 \\ 0, & otherwise \end{cases} \tag{4.8}$$

The resulting actuator voltage was measured with the voltage sensor by the DCU. This created the frequency response output/input relationship shown in Fig. 4.3F. Using this characterization, we designed a controller such that the open loop gain $G_e K_e$ would exceed 20 dB below 10 Hz (10% tracking error) and 14 dB below 20 Hz (20% tracking error). In addition, we determined that at 200 Hz, a 1/10 (-20 dB) open loop gain would guarantee acceptable disturbance rejection. These specifications resulted in the controller

$$K_e(s) = \frac{3e5}{s + 150} \tag{4.9}$$

which contains a single pole. Fig. 4.15 shows the loop shaping parameters and resultant open loop system $K_e G_e$. The closed loop bode plot (Fig. 4.3F) was generated by sending voltage commands $v_r(t) = 0.4sin(2\pi f(t)t) + 4$ in kV and measuring the response from the voltage sensor. This resulted in the $T_e = v/v_r$ frequency response (Fig. 4.3F). For the height feedback loop, using the voltage loop control as an inner closed loop, we similarly input a set of 32 sinusoidal voltage signals (where the voltage varies sinusoidally over time) with frequencies logarithmically spaced from 0.6 Hz to 50 Hz. The input signal here was $v_r(t) = 0.4sin(2\pi f(t)t) + 4$, with v_r in kV. The peak-to-peak amplitude of each sinusoid was 0.8 kV. We measured the resulting actuator displacement using the motion capture system.

This resulted in the frequency response output/input relationship shown in Fig. 4.8B. Magnetometer data was also simultaneously collected and used with the motion capture system to generate the magnetometer dynamics (Fig. 4.5C). As before, we used this characterization to design a controller such that the open loop gain $G_h K_h$ would exceed 26 dB below 10 Hz (5% tracking error) and 14 dB below 20 Hz (20% tracking error). We also set the 1/10 (-20 dB) disturbance rejection limit again at 300 Hz. These specifications resulted in the controller

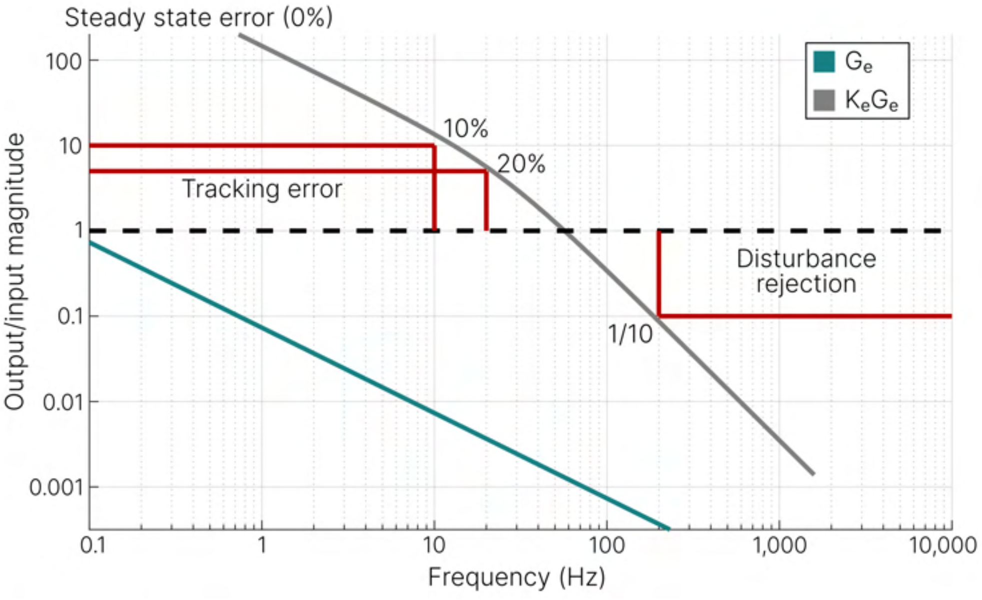

Figure 4.15: Loop shaping parameters for voltage regulation.

$$K_h(s) = \frac{30(s+70)}{s}. \tag{4.10}$$

The loop shaping parameters and resultant open loop system K_hG_h are shown in Fig. 4.16. This controller was discretized using a ZOH at 200 Hz, below the 600 Hz frequency of the inner voltage loop. We found that this discretization affected the expected performance of the controller, and to compensate adding a prefilter to the reference input with the form:

$$F(s) = (200/80)^2 \frac{(s+80)^2}{(s+200)^2} \tag{4.11}$$

which was also discretized with a ZOH at 200 Hz. The filter maintains an input gain of 1 at low frequencies, with higher frequency inputs being scaled to larger amplitudes. The closed loop frequency response (Fig. 4.8B) was generated by sending height commands $z_r(t) = 0.4sin(2\pi f(t)t) + 1.4$ at the same set of frequencies from 0.6-50 Hz and measuring the displacement response using the motion capture system to generate $T_h = z/z_r$.

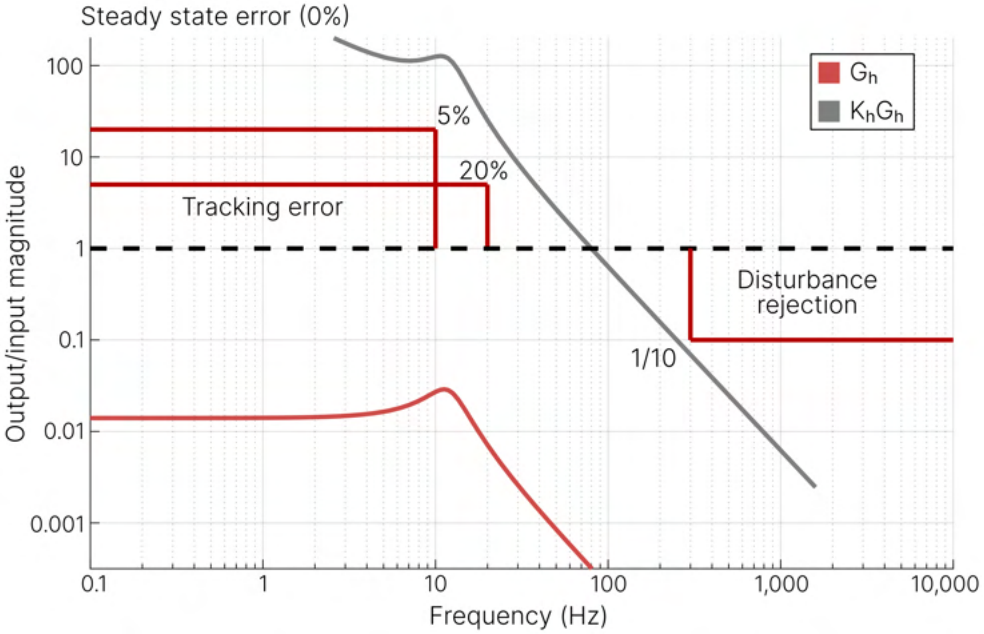

Figure 4.16: Loop shaping parameters for HASEL actuator displacement control.

4.4.7 Ball rolling algorithm and experimental setup

Given the position of the ball $\boldsymbol{x}_{ball} = (x, y)$ as well as a desired goal position x_{goal}, the initial positional error is calculated as

$$\boldsymbol{x}_{err} = \boldsymbol{x}_{goal} - \boldsymbol{x}_{ball} \tag{4.12}$$

with the normalized vector of the positional error denoted $\hat{\boldsymbol{x}}_{err}$. The ball position is captured from the USB camera at 260 Hz using a Python script and the OpenCV package. The position of the ball is computed by finding the centroid of a color mask on the camera frame. The velocity of the ball $\dot{\boldsymbol{x}}_{ball}$ is derived from the calculated position and 1/260 s sample time, and it is filtered with a five-sample moving average.

The center position of the driving shape (the arced Gaussian, Fig. 4.9B), $\boldsymbol{x}_{arc}$, is chosen such that the ball will roll down the surface towards $\boldsymbol{x}_{goal}$. This center position is calculated as

$$\boldsymbol{x}_{arc} = \boldsymbol{x}_{ball} - 0.7\hat{\boldsymbol{x}}_{err} + 0.2\dot{\boldsymbol{x}}_{ball} \tag{4.13}$$

This calculation uses the ball position as a starting point then corrects for the positional error

$\hat{\boldsymbol{x}}_{err}$ and estimated ball velocity $\dot{\boldsymbol{x}}_{ball}$. The center position $\boldsymbol{x}_{arc}$ at which to place the arced Gaussian must be chosen such that the generated shape puts the ball on a downward slope with a gradient towards the goal position $\boldsymbol{x}_{goal}$. The full closed loop algorithm runs at 52 Ha (Fig. 4.9B). The shape function over the surface $z_r(\boldsymbol{x})$ (mm) is determined by

$$z_r(\boldsymbol{x}) = 13exp\left(\frac{-(\|\boldsymbol{x}_{rel}\| - 1.2)^2}{2\sigma^2}\right) \tag{4.14}$$

where $\sigma = 0.6$ is the standard deviation of the Gaussian profile, $\|\cdot\|$ is the Euclidean norm, and $\boldsymbol{x}_{rel} = \boldsymbol{x} - \boldsymbol{x}_{arc}$ for $\boldsymbol{x} = (x, y)\forall x, y \in 0.5, 1.5, ..., 9.5$. $z_r(\boldsymbol{x})$ is a 10x10 matrix with each value being the reference displacement z_r corresponding to that cell's position in the sTISSUE array. Each cell uses z_r in closed loop feedback T_h (Fig. 4.9A).

Eq. (4.14) only holds true given the inner product $\langle \boldsymbol{x}_{arc} - \boldsymbol{x}_{ball}, \boldsymbol{x}_{rel} \rangle > -0.4$; in all other cases, $z_r(\boldsymbol{x}) = 0$. By making the surface shape non-zero only within the given angles (via inner product), an opening is created in the direction of the goal position that allows the ball to continue rolling towards the goal (Fig. 4.9B). The algorithm for a single ball is extended to control multiple balls on the surface by independently computing $z_r(\boldsymbol{x})$ for each ball. The actual set of reference displacements for the sTISSUE surface is then calculated as the maximum voltage at each cell from the set of $z_r(\boldsymbol{x})$.

For the single ball experiment (Fig. 4.9C), the ball navigates through a set of reference inputs $\{\boldsymbol{x}_{goal}\}$ defined as

$$\{\boldsymbol{x}_{goal}\} = \{(2.5, 7.5), (7.5, 7.5), (7.5, 2.5), (2.5, 2.5)\}. \tag{4.15}$$

The ball begins stationary at (2.5,2.5) with the first value in the set as its goal position, and advances to the next goal position only when $\boldsymbol{x}_{err} \leq 0.33$. As the algorithm controls the ball from goal to goal, position and velocity data are recorded by the PC. The set is run 25 times each using a standard table tennis ball as the controlled object.

In the second experiment (Fig. 4.9D), three standard table tennis balls of different colors - red, yellow, and green - are rolled down a ramp at position (10, 5) and onto the surface. The ramp is a constant incline and gives each ball the same initial conditions. The balls are rolled down the ramp in sequence to give some separation; the order of the balls (by color) does not matter. The

OpenCV code detects the position of each ball based on color and the algorithm sorts them to an edge position based on color: red to (5, 0), yellow to (0, 5), green to (5, 10) (Fig. 4.9D). This experiment was run 25 times and the ball positions and velocities were recorded by the PC.

4.5 Conclusion

In this chapter we presented the design, characterization, control, and applications of a soft robotic material driven by HASEL actuators and magnetic sensors. This work presents a significant advance for HASEL actuator-driven robots. The sTISSUE material has a variety of different functions including object manipulation, haptics, user interfaces, and more enabled through intelligent sensing of both displacement and force. The nested feedback structure on HASEL actuator voltage and displacement enables high-bandwidth, robust control. The integration of HV driving components and sensing directly into each sTISSUE cell make the material very compact, promoting future uses for untethered or tightly integrated robots. The existing form of the sTISSUE as a 10x10 shape display validates the concept of achieving greater functionality through higher DOF and supports the use of soft robotic materials to engender emergent properties and capabilities (like surface wave propagation, stimulus-response interactions, or peripheral wand-driven 'drawing').

Beyond the demonstrated shape display, sTISSUE can act as a scalable platform for designing a large variety of robot topologies, and can use different forms of electrostatic actuation and sensing without significant changes required in the hardware and software design. This opens numerous possibilities for future soft robot development using sTISSUE as the backbone to design new systems with a short amount of new effort. As discussed, such designs could utilize the existing 100 sTISSUE cells, or through modularity and scalability could employ even higher DOF in the future. The results demonstrated to date as well as the potential future applications are a promising step forward for both robotic materials and soft robots.

4.6 Acknowledgements and contributions

As the work presented in this chapter is the result of collaboration with multiple researchers, here I describe the contributions of each team member for clarity. The conceptualization of this work was done by Mark E. Rentschler, Sean Humbert, Nikolaus Correll, Christoph Keplinger, myself, Mantas

Naris, Vani Sundaram, Nicholas Kellaris, Eric Acome, Shane K. Mitchell, Khoi Ly, and Angella Volchko. The folded HASEL actuator design and material selection was performed by Eric Acome. The magnetic sensing mechanism for the HASEL actautors was designed and characterized by Vani Sundaram and Khoi Ly. The magnetometer circuit was designed by Vani Sundaram. The force sensing relationship was conceptualized and modeled by Vani Sundaram. The hardware layout of the sTISSUE 1x10 modules was performed by Mantas Naris. The design of the DCU, SCU, and associated other circuitry was done by Mantas Naris. The HV driver and sensor circuits were designed by Mantas Naris and Shane K. Mitchell, with additional improvements and testing done by myself and Angella Volchko. The implementation and use of the motion capture system was done by Mantas Naris, Vani Sundaram, Angella Volchko, and myself. The software for data collection and closed-loop control was written by Mantas Naris, myself, Vani Sundaram, and Angella Volchko. Data collection was performed by myself, Mantas Naris, and Vani Sundaram. Figure visualizations were created by myself and Mantas Naris.

In addition to the above, I performed the system identification and control design of the voltage regulator and displacement controller; implemented the global control algorithm for the 10x10 sTISSUE array; created and implemented the active feedback demonstration, the intelligent scale demonstration, the magnetic wand demonstration; and developed the dynamic ball rolling algorithm.

Chapter 5

Advanced control of soft robotic materials

While Chapter 4 discussed hardware and software developments to create advanced scalable electrostatic actuator systems like the sTISSUE, this chapter will focus on the implementation of control methods for such systems. In particular, this chapter describes a control method for the manipulation of objects on the sTISSUE surface using artificial potential field theory. This provides a more robust algorithm with additional capabilities not demonstrated in the ball-rolling algorithm in Chapter 4 and serves as a next step in developing soft robotic materials.

We begin by discussing current literature on this topic which serves as the motivation for this work. We also introduce the potential field theory which is applied to this problem. A general description of the algorithm and additional capabilities follows. We then describe the experimental setup, experimental results and analysis, and conclude with a discussion on alternative approaches and future improvements.

5.1 Introduction

Shape displays, shape-changing interfaces, or deformable surfaces are robotic systems which locally change their physical topology along discrete or continuous points of the surface [192, 193]. This is often embodied as height changes out of the plane of the originally flat surface. Some examples include inFORM [122], Wave-Handling [107], the sTISSUE array discussed in Chapter 4, as well as others in literature [110–112, 114, 164]. These deformable surfaces can be used for visual displays [164,194], teleoperation or haptic interaction [114,122,164,195], or for dynamic motion of objects on the surface [107,110–112,120,122,175]. A rolling ball is a classical application of object manipulation because it can be moved by locally changing the slope of the surface underneath the ball.

However, existing literature on effective closed loop control of such dynamic motion is lacking;

typically object manipulation is achieved either through open loop pre-programming [110], neural networks [112], or undisclosed software [107, 122]. Closed loop ball position control has been demonstrated [107, 112] but is slow and limited to single point position setting. This has also been demonstrated on the sTISSUE using preset shape changes which are locally controlled based on ball position as in Chapter 4. However, a robust, simple algorithm for total trajectory control of a ball on the surface is currently not present in literature.

We propose a closed loop algorithm for ball trajectory control on a deformable surface using artificial potential field (APF) theory. APFs, first proposed by O. Khatib as a means for robot navigation [196], have become widely popular in robotic control [197, 198]. APFs allow for built-in obstacle avoidance [199, 200], path planning [197, 201, 202], and multi-agent cooperation [203–205] with minimal mathematical setup. However, APFs are typically applied to systems with a controllable agent moving through its environment. We propose a novel APF application in which the environment, the shape-changing surface, is actively controlled to induce movement of passive agents (balls on the surface).

Our algorithm uses two separate potential fields (PFs) to control ball movement; the first is an attractive velocity gradient field which provides the desired ball velocity at each point along the surface, and the second is a repulsive potential energy field which is realized via deformation of the surface. Keeping each field composed of only attractive or repulsive terms prevents local dead-lock for positional control. The algorithm also easily extends to global trajectory control by shaping the velocity gradient APF to the desired trajectory. The control principles also extend to multiple balls, allowing multi-agent motion and shape formation control.

We first discuss the general dynamics and basic physical principles of a ball rolling along a surface, then utilize these principles to form our two-layer APF algorithm. We describe the mathematical basis of the algorithm and its implementation in code and in hardware using the sTISSUE shape display from Chapter 4. A method of performance quantification for this algorithm is introduced. Then, we perform trial experiments to validate four key capabilities of the algorithm: (1) ball positional control, (2) multi-agent interaction, (3) trajectory control, and finally (4) multi-agent formation control. Lastly, we discuss key results and conclusions of this work.

5.2 Potential field algorithm

5.2.1 Ball dynamics on a deforming surface

Before describing the implementation of potential fields for the control algorithm, we must describe the basic physical dynamics which govern the motion of a ball on a surface. The motion is driven by energy gradients and energy conversion. We define the position of the ball as $\boldsymbol{x}_{ball} \in \mathbb{R}^2$ which gives the (x,y) position of the ball. Brearley et al. showed that the deformation of a surface due to the ball's mass induces frictional energy losses [206]. A deformable surface is thus a dissipative system that requires energy input to maintain ball motion. The energy input comes in the form of potential energy via surface deformation. If the surface underneath the ball deforms upward, the ball's potential energy V increases following the classical physics equation

$$V_{ball} = Mgh_{ball} \tag{5.1}$$

with ball mass M, gravitational acceleration constant g, and change of ball height above the undeformed surface h_{ball}. The deformation of the surface is thus directly proportional to the ball's potential energy. The slope of the surface deformation also forms a gradient of the potential energy. If the ball rolls down the slope to the surrounding undeformed surface, the potential energy converts into both linear and rotational kinetic energy. The sum of kinetic energy T is thus

$$V_{ball} \rightarrow T_{ball} = \frac{1}{2}M\|\dot{\boldsymbol{x}}_{ball}\|^2 + \frac{1}{2}I(\|\dot{\boldsymbol{x}}_{ball}\|/r)^2 \tag{5.2}$$

where $\|\cdot\|$ denotes the 2-norm, I is the ball moment of inertia, and r is the ball radius. For this analysis, we assume that the ball is a hollow sphere with moment of inertia $I = (2/3)Mr^2$. The velocity $\dot{\boldsymbol{x}}_{ball}$ increases in the direction of the potential energy gradient:

$$\hat{\dot{\boldsymbol{x}}}_{ball} = -\frac{\nabla V_{ball}}{\|\nabla V_{ball}\|} \tag{5.3}$$

where $\hat{\dot{\boldsymbol{x}}}_{ball}$ indicates the normalized ball velocity. We also assume a no-slip condition between the ball and surface. This is the governing concept of rolling object manipulation on a deforming surface, and it has been the mathematical basis for existing motion control methods on shape-changing surfaces [107, 112]. We apply this as this basis for one of the artificial potential fields in our algorithm.

5.2.2 Artificial Potential Fields (APFs)

Our algorithm is divided into two potential fields: The first is a Kinetic APF (KPF) and the second is a Potential Energy PF (PPF). The KPF is part of the outer control loop which dictates ball velocity and therefore trajectory (position being integral of velocity), while the PPF is in the inner loop and controls active surface deformation to achieve the desired velocities of the KPF. Following Khatib [196], our general approach is to use the negative gradient of the potential field to ultimately control the state of the agent in its environment. In our case, we are controlling the velocity of a ball along a shape display surface. The steps of the algorithm are outlined in Figure 5.1.

KPF for positional control

We construct an APF based on kinetic energy whose gradient gives desired agent velocity. This potential field approach has been used in prior works [201,202] for mobile robots navigating through a traditional environment. For positional control (i.e. setting a target position/goal for the ball to roll to), we define the KPF as a simple quadratic attractor centered on the goal:

$$KPF = a_v \|\boldsymbol{x}_{ball} - \boldsymbol{x}_{goal}\|^2 \tag{5.4}$$

where a_v is a constant scaling factor and $\boldsymbol{x}_{goal}$ is the [x y] position of the goal. Taking the negative gradient of the KPF gives the desired ball velocity $\dot{\boldsymbol{x}}_{des}$:

$$\dot{\boldsymbol{x}}_{des} = -\nabla KPF = -2a_v(\boldsymbol{x}_{ball} - \boldsymbol{x}_{goal}). \tag{5.5}$$

The resulting velocity vector $\dot{\boldsymbol{x}}_{des}$ will always point towards the goal position and with a larger magnitude the further the ball is from the goal. This desired velocity determines the required velocity vector $\dot{\boldsymbol{x}}_{req}$:

$$\dot{\boldsymbol{x}}_{req} = \dot{\boldsymbol{x}}_{des} - \dot{\boldsymbol{x}}_{ball} \tag{5.6}$$

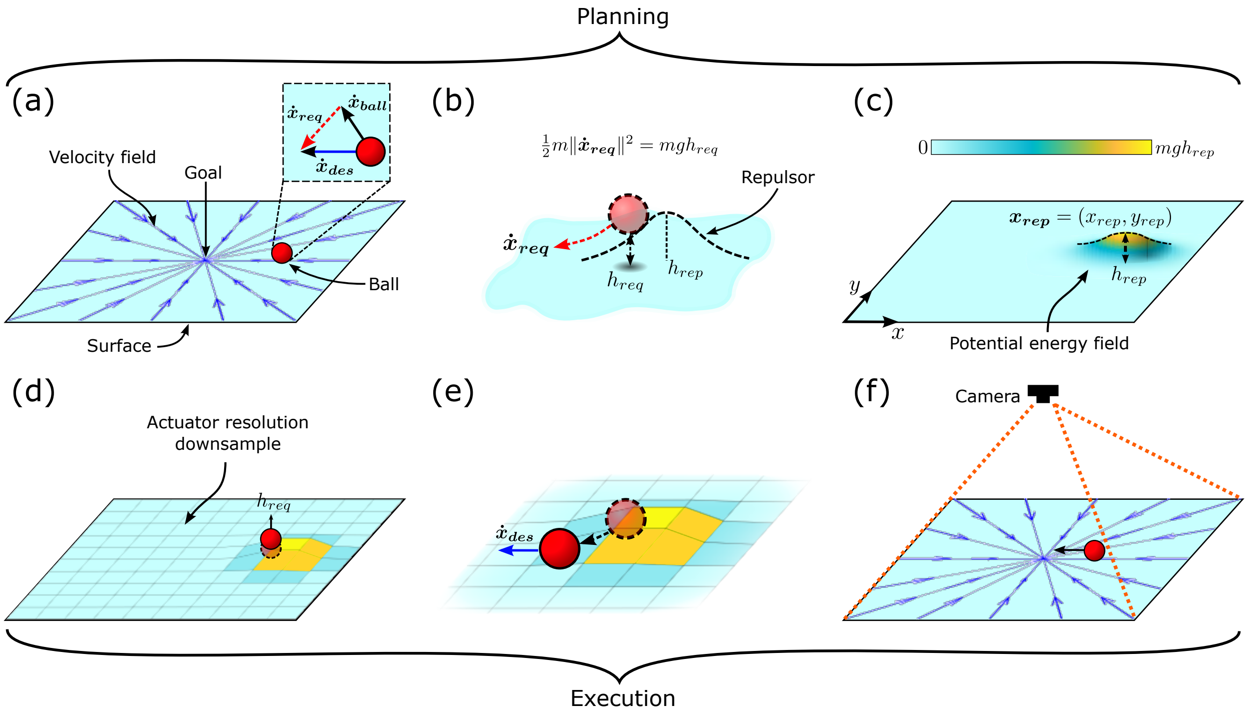

Figure 5.1: Steps of the two-layer APF algorithm. **(a)** The ball position and velocity vector field from the Velocity Artificial Potential Field (KPF) determine the desired velocity $\dot{\boldsymbol{x}}_{\boldsymbol{des}}$. Vector addition is used to find the required velocity $\dot{\boldsymbol{x}}_{\boldsymbol{req}}$. Varieties of the KPF are shown in Figure 5.2. **(b)** h_{req} is calculated using conservation of energy from Eq. (5.7). h_{req} is formed from the slope of a 2D Gaussian repulsive potential. **(c)** The position $\boldsymbol{x}_{\boldsymbol{rep}}$ and height h_{rep} of the repulsor are determined using Eqs. (5.9, 5.10), forming a global Potential Energy Potential Field (PPF). **(d)** The PPF on the surface is down-sampled to the surface actuator resolution. In this case, the surface is driven by a 10x10 actuator array. Actuating the surface according to the PPF lifts the ball by h_{req} **(e)** The ball rolls down the gradient of the repulsor. The velocity increases by $\dot{\boldsymbol{x}}_{\boldsymbol{req}}$, resulting in a total velocity vector $\dot{\boldsymbol{x}}_{\boldsymbol{des}}$. **(f)** The surface is returned to its undeformed shape. An overhead camera measures the new position and velocity of the ball. The algorithm can then be repeated starting from step **(a)**.

Adding the required velocity to the current velocity achieves the desired velocity for the KPF. The magnitude $\|\dot{\boldsymbol{x}}_{req}\|$ and normalized direction $\hat{\dot{\boldsymbol{x}}}_{req}$ of the required velocity vector are the inputs to the PPF.

PPF to generate velocity

The second PF used in our algorithm describes the desired potential energy across the deformable surface. It is formed by a single repulsive potential function in the form of a 2D Gaussian. Following the discussion in Section 5.2.1, the PPF represents both the energy input to the ball and the height map of the deformable surface. The repulsive potential function forms the 'hill' which causes the ball to gain potential energy, which can then be converted to kinetic energy to alter the ball's velocity to achieve $\dot{\boldsymbol{x}}_{des}$. Unlike the KPF, the PPF is not an artificial field; the energies of the field are realized via deformation of the shape display.

The PPF is inversely determined because the output velocity $\dot{\boldsymbol{x}}_{req}$ is already known via Eqs. (5.5, 5.6) and the repulsor magnitude and position required to produce $\dot{\boldsymbol{x}}_{req}$ must be calculated. Combining Eqs. (5.1, 5.2) gives the relationship between the desired height of the surface deformation and the resulting ball velocity $\dot{\boldsymbol{x}}_{req}$):

$$\begin{aligned} V_{ball} = Mgh_{req} &= \frac{1}{2}M\|\dot{\boldsymbol{x}}_{req}\|^2 + \frac{1}{2}I(\|\dot{\boldsymbol{x}}_{req}\|/r)^2 = T_{ball} \\ Mgh_{req} &= \frac{1}{2}M\|\dot{\boldsymbol{x}}_{req}\|^2 + \frac{2}{6}M\|\dot{\boldsymbol{x}}_{req}\|^2 \\ h_{req} &= \frac{5}{6g}\|\dot{\boldsymbol{x}}_{req}\|^2. \end{aligned} \tag{5.7}$$

Note that the mass of the ball is irrelevant for our algorithm. However, this analysis assumes no frictional energy losses, whereas on a deformable surface, higher mass corresponds to increased surface friction [206]. We now define the standard 2D Gaussian function as the PPF:

$$PPF(\boldsymbol{x}_{surf}) = h(\boldsymbol{x}_{surf}) = h_{rep}\text{exp}\left(\frac{-1}{2\sigma^2}\|\boldsymbol{x}_{surf} - \boldsymbol{x}_{rep}\|^2\right), \tag{5.8}$$

where $\boldsymbol{x}_{surf} \in \mathbb{R}^2$ spans the surface, h_{rep} is the peak height of the repulsor, σ^2 is the repulsor variance (equal in both dimensions), and $\boldsymbol{x}_{rep} \in \mathbb{R}^2$ is the repulsor peak position. We enforce the following relationship between the required height and the peak height of the repulsor on the surface:

$$h_{rep} = \frac{3}{2}h_{req}. \tag{5.9}$$

This ensures that the ball will be positioned below the peak height of the repulsor which enables the ball to follow the appropriate gradient. Using h_{req} and $\hat{\dot{x}}_{req}$ as inputs, we calculate the position of the repulsor $\boldsymbol{x}_{rep}$ via

$$\boldsymbol{x}_{rep} = \boldsymbol{x}_{ball} - \left[-2\sigma^2\text{ln}(h_{req}/13)\right]^{1/2}\hat{\dot{\boldsymbol{x}}}_{req} + \alpha\dot{\boldsymbol{x}}_{ball} \tag{5.10}$$

where α is a scaling factor. The repulsor position is firstly determined by the ball position, offset in the amount given by the $[\cdot]^{1/2}$ term so that the repulsor height at the ball position is the required height, i.e. $h(\boldsymbol{x}_{ball}) = h_{req}$. A second adjustment is made using the ball velocity $\dot{\boldsymbol{x}}_{ball}$ to account for time delay in the algorithm. For a ball traveling with high velocity, the repulsor position will be incorrect by the time the shape display actuates to the commanded topology; the velocity correction address this.

As previously discussed, the PPF forms the direct height map for the entire deformable surface. Since the PPF is formed by a single repulsor with small variance relative to the size of the surface, most of the surface maintains negligible deformation; only the localized repulsor will correspond to large changes in local surface height. Using this single repulsor as the ball driver is a more energy efficient than global approaches which rely on large swathes of surface deformation to control ball position [122].

5.2.3 Closed loop algorithm summary

Figure 5.1 outlines the algorithm. The full procedure is as follows:

Algorithm 1 Two-layer APF velocity control

```
while active do
    Get ball position $\boldsymbol{x}_{ball}$ and velocity $\dot{\boldsymbol{x}}_{ball}$
    Apply Eq. (5.5) to get KPF $\dot{\boldsymbol{x}}_{des}$
    Apply Eq. (5.6) to get $\dot{\boldsymbol{x}}_{req}$
    Get PPF magnitude $h_{rep}$ using Eqs. (5.7, 5.9)
    Get PPF position $x_{rep}$ with Eq. (5.10)
    Sample the shape display surface coordinates $\boldsymbol{x}_{surf}$
    Apply Eq. 5.8 to get pixel height across $\boldsymbol{x}_{surf}$
    Apply height commands to each actuator
    while height commands set do
        Local controllers maintain actuator heights
    end while
    Surface deformation increases $V_{ball}$
    Following Eqs. (5.2, 5.3), $V_{ball} \rightarrow T_{ball}$ in $\hat{\dot{\boldsymbol{x}}}_{ball}$
end while
```

A key assumption in this algorithm is that the energy conversion from potential to kinetic occurs in the same surface position. In reality, when the ball rolls down a surface gradient and converts potential energy to kinetic, the position of the ball is displaced from its origin. The result is that the new position of the ball corresponds to a different $\dot{\boldsymbol{x}}_{des}$ according to the KPF than the one originally controlled for; due to this, a near-constant error is introduced to the system because $\dot{\boldsymbol{x}}_{des}$ is always achieved at an offset position from the ball origin. This error scales with ball velocity; where the KPF magnitude is small the impact is reduced.

The two-layer APF algorithm is also free of APF dead-lock for positional control. Dead-lock occurs when the agent follows the negative gradient of the potential field into local minima instead of the desired global minimum [198]. By separating the attractive (velocity) and repulsive (height) features into separate potential fields, there are no local minima and thus dead-lock is avoided across the surface. Taking the gradient of the KPF, given in Eq. 5.5, and solving for all KPF minima

$$\begin{aligned} \dot{\boldsymbol{x}}_{des} = -\nabla KPF = 0 \\ -2a_v(\boldsymbol{x}_{ball} - \boldsymbol{x}_{goal}) = 0 \\ \boldsymbol{x}_{ball} = \boldsymbol{x}_{goal} \end{aligned} \tag{5.11}$$

shows that only a single global minimum exists for the KPF (at $\boldsymbol{x}_{ball} = \boldsymbol{x}_{goal}$); likewise, for the PPF constructed of a single repulsor,

$$\begin{aligned} -\nabla PPF(\boldsymbol{x}_{surf}) = 0 \\ -\nabla \left[h_{rep}\text{exp}\left(\frac{-1}{2\sigma^2} \|\boldsymbol{x}_{surf} - \boldsymbol{x}_{rep}\|^2 \right) \right] = 0 \\ \frac{1}{\sigma^2}(\boldsymbol{x}_{surf} - \boldsymbol{x}_{rep}) h_{rep}\text{exp}\left(\frac{-1}{2\sigma^2} \|\boldsymbol{x}_{surf} - \boldsymbol{x}_{rep}\|^2 \right) = 0 \\ \boldsymbol{x}_{surf} = \boldsymbol{x}_{rep} \end{aligned} \tag{5.12}$$

only a single global maximum exists (at $\boldsymbol{x}_{surf} = \boldsymbol{x}_{rep}$). Due to the trivial construction of both the KPF and PPF, this guarantees no algorithmic dead-lock.

5.2.4 Stability analysis

To analysis stability in a BIBO (bounded input bounded output) sense, we define the storage function at time t_0, $E(t_0)$, as

$$E(t_0) = V(t_0) + T(t_0) \tag{5.13}$$

where V and T are the total potential and kinetic energies of the ball on the surface, respectively. When the surface deforms according to the PPF function at some time t_k, we impart some potential energy into the storage function: $V(t_k) - V(t_0) = \Delta V(t_k) > 0$. $\Delta V(t_k)$ is bounded because the displacement of the shape display has a finite limit. We assume that this does not change the kinetic energy of the ball, i.e. $\Delta T(t_k) = 0$. The storage function becomes

$$\begin{aligned} E(t_k) &= \Delta V(t_k) + V(t_0) + \Delta T(t_k) + T(t_0) \\ &= \Delta V(t_k) + E(t_0). \end{aligned} \tag{5.14}$$

As the ball rolls down the PPF gradient, the increased potential energy is converted to kinetic energy. That is, at time t_{k+1},

$$\Delta T(t_{k+1}) = -\Delta V(t_{k+1}), \tag{5.15}$$

and

$$\begin{aligned} E(t_{k+1}) &= \Delta V(t_{k+1}) + V(t_k) + \Delta T(t_{k+1}) + T(t_k) \\ &= E(t_k). \end{aligned} \tag{5.16}$$

The energy conversion does not increase the overall energy of the system. As we have already discussed, a deformable surface without continued inputs is dissipative with respect to objects on the surface. We therefore expect that if no additional inputs are provided, $\dot{E}(t) < 0$ for $t > t_{k+1}$. Therefore, we find that this system is stable in the BIBO sense because for a bounded potential energy input, the output kinetic energy is always equal or smaller.

5.2.5 Multi-agent extension

The two-layer APF algorithm outlined in Section 5.2.2 can also be extended to control the velocity of multiple agents (balls) across the surface. Each ball independently follows the general algorithm, with the addition that the KPF contains repulsors of each other ball on the surface. In essence, the goal position remains the sole attractor in the KPF, but now other agents act as repulsors within the KPF. The repulsors in the KPF allow each agent on the surface to maintain distance separation from each other, preventing collisions or agents clumping together. Given this, Eq. (5.4) is modified to

$$KPF_n = a_{n,v}\|\boldsymbol{x}_{n,ball} - \boldsymbol{x}_{n,goal}\|^2 + \sum_{\substack{i=1 \\ i\neq n}}^{m} R(i) \tag{5.17}$$

for m total agents and current agent n. The repulsor $R(i)$ towards agent n from each other agent i is

$$R(i) = r_v \exp\left(\frac{-1}{2{\sigma_v}^2}\|\boldsymbol{x}_{n,ball} - \boldsymbol{x}_{i,ball}\|^2\right) \tag{5.18}$$

where r_v and ${\sigma_v}^2$ is the repulsor magnitude and variance. Taking the negative gradient of the KPF results in the new desired velocity of each agent, modified from Eq. (5.5):

$$\begin{aligned}\dot{\boldsymbol{x}}_{n,des} &= -\nabla KPF_n \\ &= -2a_{n,v}(\boldsymbol{x}_{n,ball} - \boldsymbol{x}_{n,goal}) \\ &\quad + \sum_{\substack{i=1 \\ i\neq n}}^{m} \frac{1}{{\sigma_v}^2}(\boldsymbol{x}_{n,ball} - \boldsymbol{x}_{i,ball})R(i).\end{aligned} \tag{5.19}$$

Note that the addition of the repulsor terms to the KPF can create instantaneous local minima which was not possible for the single agent version. However, actual dead-lock is not possible since the the repulsors are mutual between agents; local minima will be destroyed or move because each ball repels every other ball in contrast to a static obstacle which receives no repulsive force from a moving agent.

The $\dot{\boldsymbol{x}}_{n,des}$ for each agent n can then be used to calculate each $\dot{\boldsymbol{x}}_{n,req}$ following Eq. (5.6). Similarly, following Eqs. (5.7-5.10) one can derive the $h_{n,rep}$ and $\boldsymbol{x}_{n,rep}$ for each agent. These values from each agent are then input to Eq. (5.8) to obtain $PPF_n(\boldsymbol{x}_{surf})$ for each agent. The set of PPFs from all agents is

$$F(\boldsymbol{x}_{surf}) = \{PPF_n(\boldsymbol{x}_{surf}) | n = 1, ..., m\}, \tag{5.20}$$

and the global PPF applied to the surface is the maximum value from F at every point in $\boldsymbol{x}_{surf}$,

$$PPF_{global}(\boldsymbol{x}_{surf}) = \max(F(\boldsymbol{x}_{surf})). \tag{5.21}$$

Accordingly, if the PPFs of two or more agents overlap on $\boldsymbol{x}_{surf}$, the PPF with the largest magnitude at that location is used.

To summarize the multi-agent extension, given m agents on the surface with m independent goals, each individual agent will be controlled in velocity by a KPF with 1 attractor (goal) and $m - 1$ repulsors (other agents). Each repulsor is at the location of the other agents on the surface. Following the closed loop algorithm outline in Section 5.2.3 and modified via the equations in this section, m separate PPFs are generated which correspond to m surface height maps. The global height map applied to the deformable surface is generated by taking the maximum value of the set of m PPFs at each point along the surface.

5.2.6 Trajectory control

In Section 5.2.2 we described the basic APF algorithm which covers point-to-point control of an agent on the surface. In that case, the KPF is determined by a quadratic attractor between the agent position and the goal position. However, one can also directly specify the KPF such that the gradient is any desired vector field. Because the KPF gradient is a vector field of velocities, directly specifying the velocities controls the agent's position and trajectory over time. By replacing the KPF gradient in Eq. (5.5) with an arbitrary vector field, an agent on the surface will trace out the path of the vector field based on its initial state conditions (position, velocity). However, because the KPF can be arbitrarily modified there is no guarantee that no local minima exist; the vector field must be picked carefully to avoid dead-lock.

For example, given the vector field equation of a stable limit cycle with radius r, scaling factor γ, centered on $(0, 0)$

$$f\left(\begin{bmatrix} x \\ y \end{bmatrix}\right) = \gamma \begin{bmatrix} -y + x(r^2 - x^2 - y^2 - 1) \\ x + y(r^2 - x^2 - y^2 - 1) \end{bmatrix}, \tag{5.22}$$

the KPF gradient can be replaced to also provide a stable limit cycle of desired velocity. In this case, we offset the (x, y) positions by (x_c, y_c) to shift the center position of the limit cycle:

$$x_d = \boldsymbol{x}_{ball}(1) - x_c,\ y_d = \boldsymbol{x}_{ball}(2) - y_c. \tag{5.23}$$

Rather than an infinitesimally narrow stable orbit of the limit cycle, we also choose an inner radius r_i and outer radius r_o in which the KPF field is a stable orbit. The resulting equation for the desired velocity on the KPF is

$$\dot{\boldsymbol{x}}_{des} = \begin{cases} \gamma \begin{bmatrix} -x_d + x_d(v_i - 1) & x_d + y_d(v_i - 1) \end{bmatrix}, & v_i > 0 \\ \gamma \begin{bmatrix} -x_d + x_d(v_o - 1) & x_d + y_d(v_o - 1) \end{bmatrix}, & v_o < 0 \\ \gamma \begin{bmatrix} -y_d & x_d \end{bmatrix}, & otherwise \end{cases} \tag{5.24}$$

$$v_i = r_i^2 - x_d^2 - y_d^2$$

$$v_o = r_o^2 - x_d^2 - y_d^2$$

By control of the PPF the ball following the vector fields according to Eq. (5.24) will orbit around the center (x_c, y_c) at a radius between r_i and r_o. The speed of the orbit will be controlled by γ.

5.2.7 Formation control

Making a small addition to the multi-agent equations allows us to create simple multi-agent formations based on regular polygons. This can be done by adding an attractor located at the global centroid of the agents on the surface. Eq. (5.17) is modified by replacing the goal position $\boldsymbol{x}_{goal}$

with the centroid $\boldsymbol{x}_c$:

$$\boldsymbol{x}_c = \frac{1}{m} \sum_{i=1}^{m} \boldsymbol{x}_{i,ball}. \tag{5.25}$$

Eq. (5.17) thus becomes

$$KPF_n = c_v \|\boldsymbol{x}_{n,ball} - \boldsymbol{x}_c\|^2 + \sum_{\substack{i=1 \\ i \neq n}}^{m} R(i) \tag{5.26}$$

with scaling factor c_v applied to the centroid attractor. Similar techniques have been used in previous formation control works [207, 208].

For m agents in the shape of an m-sided regular polygon each agent experiences an attractive force in the KPF towards the centroid (center of the polygon) and $m - 1$ repulsive forces from the other agents. The off-center repulsive forces will cancel each other out in a regular polygon, resulting in a net repulsive force opposite the direction of the attractive force towards the centroid. At a certain distance from the centroid these forces result in a net zero force in the KPF, resulting in a minimum in the field and zero velocity vector in the gradient. Adjusting the scaling factor c_v controls the distance from the centroid at which the minimum occurs. This formation control can be thought of as utilizing the local minimum ”dead-lock” problem to our advantage; we purposefully create dead-lock in the multi-agent system to induce an overall geometry between the agents on the surface.

5.3 Experimental validation

Having described the mathematical approach of our two-layer APF algorithm, we implemented the algorithm on an actual shape-changing surface to validate its effectiveness and each of its use-cases (positional control, trajectory control, multi-agent control, and formation control).

5.3.1 Hardware

The shape-changing surface we use to validate the two-layer APF algorithm is the 10x10 sTISSUE array discussed in Chapter 4. sTISSUE uses a thin silicon skin (EcoFlex 00-30, Smooth-On) as the surface interface. The skin deforms locally according to the strains of each HASEL underneath

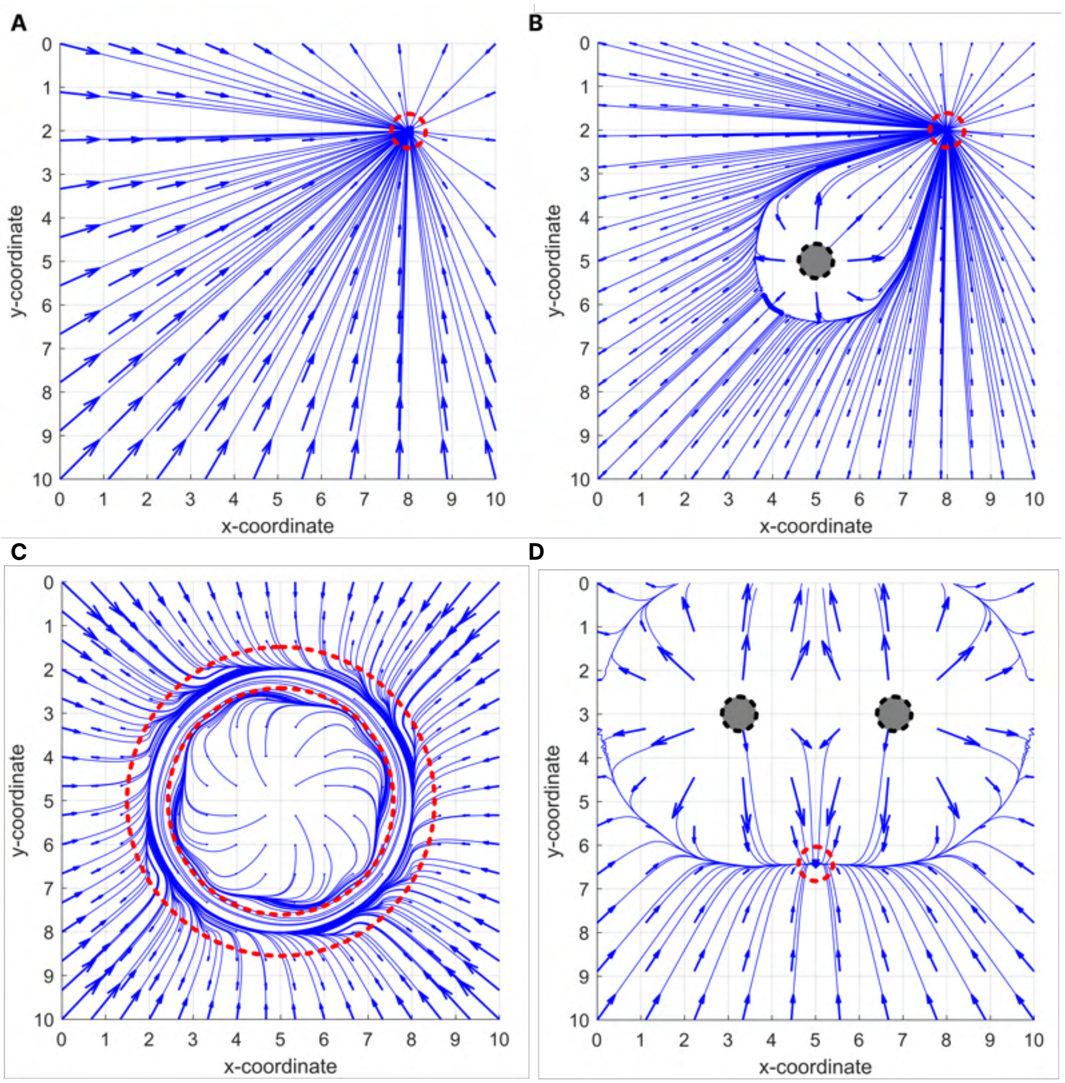

Figure 5.2: A sample of possible velocity vector fields on a surface spanning from (0,0) to (10,10). Arrows indicate velocity direction and magnitude, solid lines denote trajectories, and the dashed red circles denotes the KPF minimum region. **(A)** Simple attractor to a goal position at (8,2). **(B)** Multi-agent case with attractor to the goal at (8,2) and another agent (solid circle) acting as a repulsive force at (5,5) to the agent under consideration. **(C)** Trajectory specification using the equation of a limit cycle centered on (5,5). The dashed lines denote the stable region, which lies between a radius of 2.5 and 3.5 from the center. **(D)** Formation of three agents with the other two agents (solid circles) acting as repulsors to the agent under consideration. An attractor is positioned at the geometric centroid of the three agents; the KPF minimum occurs at the location resulting in an equilateral triangle formation.

it and creates a smooth surface topology without gaps. This forms the rolling and manipulation surface for our experimental validation.

A high speed USB color camera (2.9 mm Wide Angle, ELP) is placed 115 cm above the surface looking downwards. The camera captures image data of the entire sTISSUE surface at 260 fps. This is used to measure ball position as well as identify multiple balls based on color or size.

The sTISSUE PC streams data from the USB camera, runs the two-layer APF algorithm, and sends displacement reference commands to the 10 microcontrollers on the sTISSUE shape display. The microcontrollers are locally responsible for controlling the voltages and displacements of each HASEL actuator.

5.3.2 Algorithm and software implementation

The specific two-layer APF algorithm follows the mathematical equations and closed loop approach outlined in Section 5.2. We normalized all positions and velocities to the side length of a single pixel on the surface, approximately 6 cm. Therefore, a speed of 1 unit/s corresponds to 6 cm/s. We will also discuss ball diameter in terms of unit length. This allows the results to have physical meaning for other shape displays or systems where the pixel size and ball size may differ.

Using the hardware setup described in Section 5.3.1, we implemented the two-layer APF algorithm using the open source language Julia [155]. The Julia scripts which govern general communication between the computer and the MCU, as well as the C++ scripts which control the MCUs are taken directly from Chapter 4. The USB camera interfaces with the Julia code using a Python script and the OpenCV package [191]. OpenCV is used for color detection and blob detection of any balls within the image frame. The Python script sends ball position information to Julia via local UDP port structure. The velocity is differentiated using a weighted mean of the latest 10 ball position values and used in the KPF calculation with a 260 Hz update rate. The smoothed velocity derived from $\boldsymbol{x}_{ball}$ at sample time $[k]$ with sample frequency f_s (Hz) using a 10-sample weighted moving average is

$$\dot{\boldsymbol{x}}_{ball}[k] = \left(\boldsymbol{x}_{ball}[k] - \boldsymbol{x}_{ball}[k-1]\right) f_s \tag{5.27}$$

$$\dot{\boldsymbol{x}}_{ball,smth}[k] = \frac{\sum_{i=1}^{10} W[i]\dot{\boldsymbol{x}}_{ball}[k-(i-1)]}{\sum_{i=1}^{10} W[i]} \tag{5.28}$$

$$W = \begin{bmatrix} 1 & 0.917 & 0.833 & 0.75 & 0.667 & 0.584 & 0.5 & 0.417 & 0.334 & 0.25 \end{bmatrix}.$$

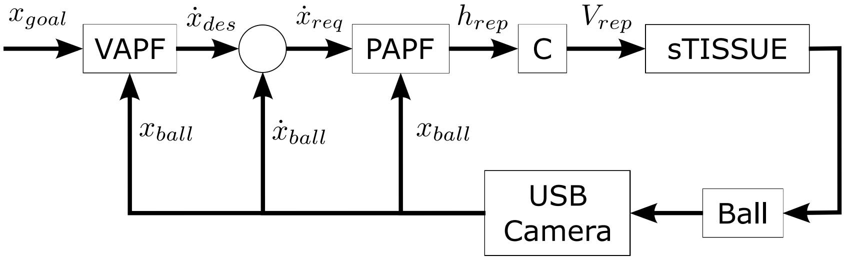

Figure 5.3: Block diagram for the two-layer APF control algorithm implemented on the sTISSUE. The overhead USB camera measures the ball's position x and velocity $\dot{x}$. The desired ball position x_{des} and x are used in the KPF to determine the instantaneous $\dot{x}_{des}$. This determines the velocity error $\dot{x}_{err}$, which is used in the PPF to compute the desired surface topology to induce ball motion. The desired topology is sent as a matrix of reference voltages to the MCUs in the sTISSUE. Upon executing the voltage commands, the surface deforms, causing the ball to move.

Because the weighted mean introduces a lag in the sensor measurement, the PPF is calculated at a 26 Hz rate. This is a sufficient loop frequency to control object motion without excessive lag. The sTISSUE closed loop frequency is 200 Hz, well above the PPF frequency.

The closed loop block diagram describing the application of the algorithm is in Fig. 5.3.

5.3.3 Performance quantification

To validate the success of the two-layer APF algorithm on the sTISSUE, we first define quantifiable measures of success. The dynamic motion of a ball rolling on a deformable surface is both spatial and temporal. Our algorithm also includes several aspects such as goal setting, velocity control, and trajectory specification which we examine separately. This section describes our methodology in quantifying the performance of the algorithm in controlling ball motion on a deformable surface and lays out the tests we performed whose results are discussed in Section 5.4.

Step inputs

In single-input-single-output control systems, a step input response is often used to characterize the controller in terms of the overshoot, rise time, and settling time of the controlled state. We extend this concept to our control scheme by introducing a KPF with a uniform, constant velocity gradient. Our 'step' input takes the form of a transition from a uniform zero velocity gradient to a uniform constant velocity gradient

$$\dot{\boldsymbol{x}}_{des} = \boldsymbol{0} \rightarrow v\hat{\boldsymbol{e}} \tag{5.29}$$

where v is the scalar speed $\hat{\boldsymbol{e}}$ is the unit direction vector of the uniform velocity field. For example, $\hat{\boldsymbol{e}} = (1, 0)$ corresponds to a uniform velocity field along the x-axis of the shape-changing surface. This field can thus be applied in different directions to evaluate the step response of the algorithm under all conditions. It is expected that the ball dynamics are different for off-axis directions because the shape of each actuator is square; a deformed HASEL actuator therefore does not produce uniform surface deformation in all directions.

With this in mind, we evaluated the step response of the algorithm under 5 directions and 74 speeds with the speed and direction vector specified by

$$\begin{aligned} &v = \{2, 3, 4, 5, 6, 7, 8\}\ unit/s \\ &\hat{\boldsymbol{e}} = \left\{\left(cos\left(n\frac{\pi}{8}\right), sin\left(n\frac{\pi}{8}\right)\right) | n = 0, 1, ..., 4\right\}. \end{aligned} \tag{5.30}$$

Following Eq (5.29), each test began with a motionless ball on the surface with uniform zero velocity field. The non-zero field was input to the system, and as the ball moved its position and velocity were recorded along with time data. A standard table tennis ball was used for directional tests. For each of the tests, the ball was intentionally placed in different locations on the surface to test the algorithm's spatial robustness. For each direction n, 6 trials were performed using a constant speed $v = 4$ for each n. Likewise, for each speed v, 6 trials were performed using a constant direction $n = 0$ for each v.

The speed test data was processed by measuring the 10-90% rise time of the ball velocity from 0 to the target velocity v for each trial and each speed. The direction data was processed by first subtracting the start position of each trial, such that each trial began at (0,0). We then normalized the data in time, re-sampled to 501 points for each trial, and calculated the mean position of the 6 trials over time. Finally, the positions were normalized to a unit circle.

Positional control testing for single and multiple agents

Beyond characterizing the general algorithm performance using the step input fields, we also sought to qualitatively evaluate the positional control of the algorithm for both a single and multi-agent scenario.

For the single agent case, we positioned the ball at a starting location of (2,8) on the surface with the KPF set to a goal position of (8,2). As the ball traveled along the surface we recorded position and time data. The test was terminated after the ball reached the goal position. This was repeated 10 times. Fig. 5.2A shows the velocity field created in this experiment.

For the multi agent case, we followed Eqs. (5.17)-(5.21). We again positioned the ball at a starting location of (2,8) on the surface with the KPF set to a goal position of (8,2). However, we also added a static (non-moving) ball at position (5,5). Following the rules of the algorithm, this is treated as a repulsor within the KPF and will thus affect the trajectory of the ball as it moves towards the goal position. As the ball traveled along the surface we recorded position and time data. The test was terminated after the ball reached the goal position. This was also repeated 10 times. Fig. 5.2B shows the velocity field created in this experiment.

Limit cycle trajectory analysis

We are also interested in quantifying the performance of the algorithm in rolling the ball along curved trajectories without the need to specify a particular goal position.

We decided to test the algorithm's ability to follow the limit cycle KPF laid out in Eq. (5.24). The shape display pixel size plays an especially important role in the performance of this experiment. Tightly curved trajectories with a small radius of curvature necessarily contain more degrees of arc across a single pixel on the shape display compared to broadly curved trajectories. These tightly curved trajectories are therefore harder to maintain given the reduced number of actuators at play. To provide sufficient control authority, we set $r_i = 2.5$ and $r_o = 2.5$ in Eq. (5.24). The orbit is centered at $x_c = 5, x_d = 5$, the center of the 10x10 sTISSUE surface. Fig. 5.2C shows the velocity field created in this experiment.

To evaluate the performance of the trajectory control, we placed the ball in a starting position within the stable orbit (between 2.5-3.5 radius from the center) and activated the APF algorithm. As the ball moved across the surface we recorded position and time data. We recorded this data during a total of 20 orbits along the limit cycle taken across 4 experimental trials.

Table 5.1 lists the parameter values used in the above experiments using the equations in Section 5.2. Due to the limited actuation height of each pixel on the sTISSUE shape display, we limited

Table 5.1: Algorithm parameter values for sTISSUE

Equation	Parameter	Value
(5.5)	a_v	1.5
(5.8)	σ^2	0.5625
(5.10)	α	0.25
(5.17)	$a_{n,v}$	1.5
(5.18)	r_v	100
(5.18)	${\sigma_v}^2$	0.25
(5.24)	γ	1

h_{req} to a maximum value of 10 mm.

Multi-agent formation control with three agents

Lastly, we wished to test the formation capabilities of the multi-agent algorithm. This was done in a three-agent system which corresponds to an equilateral triangle formation; one agent at each vertex. Following Eqs. (5.25)-(5.26), we set up the three agents such that the KPF of each agent is an attractor towards the geometric centroid, with repulsors added at the positions of the other agents. Fig. 5.2D shows an example velocity field which would be generated by this experiment. The resultant formation is an equilateral triangle with area 6.25 pixel^2 and a side length of 3.8 pixel.

We performed a total of seven trials where we positioned each agent near a different corner of the sTISSUE, ran the APF algorithm, and observed the position of the agents over time. Time and position of each agent was recorded over each trial.

To quantify the performance of the formation control, we evaluated both the mean side (of all three sides) and mean area over time of the triangle formed by the three agents. If all three sides are the correct length, then the desired equilateral triangle formation has been achieved. The area value provide additional confirmation and also helps evaluate the overall formation performance.

For the formation controller, some values from Table 5.1 were modified to obtain the desired formation shape. Table 5.2 lists the parameter values used for the formation control experiments.

Table 5.2: Algorithm parameters for formation control

Equation	Parameter	Value
(5.18)	r_v	150
(5.18)	${\sigma_v}^2$	1.96
(5.26)	c_v	1.5

5.4 Results

5.4.1 Uniform field step inputs

Fig. 5.4 shows the quantified performance of the algorithm in generating ball motion. The median 10-90% rise times for all tested target speeds were below 1 s. For speeds below 8 pixel/s (48 cm/s on sTISSUE) the median rise times were below 0.5 s. This shows a rapid ability to control ball velocity using surface deformation. While these tests were performed with the ball initially static, they can yield predictions toward the positional control abilities of the algorithm. Because there is some rise time in changing velocity, typically between 0.2-1 s, that means that overshoot is possible in positional control. When the ball moves beyond its goal position, the velocity rise time causes a delayed response in reversing the velocity of the ball back to the goal. However, the results overall still indicate high-speed control capabilities. The consistency is also very good for target speeds between 5-6 pixel/s, with only a 0.1 s difference between the 25th and 75th percentiles of rise time.

For the directional performance, the results similarly show the accuracy of the APF algorithm (Fig. 5.4B). The mean trajectories of all trials show that the algorithm was able to keep the ball moving in the commanded directly with only slight deviation. An important result to note is that the performances of the $n = 1, 2, 3$ directions, which are directions not orthogonal to the edges of the square sTISSUE actuators, exhibit a similar accuracy as the results from the orthogonal directions ($n = 0, 4$). This shows that there is negligible impact of the shape of the actuators/pixels on the surface in terms of the algorithm's performance in directing the ball in the accurate direction. This is in spite of the inaccuracies in the shape topology which comes from downsampling a circular 2D Gaussian curve to square actuators at a low sampling resolution.

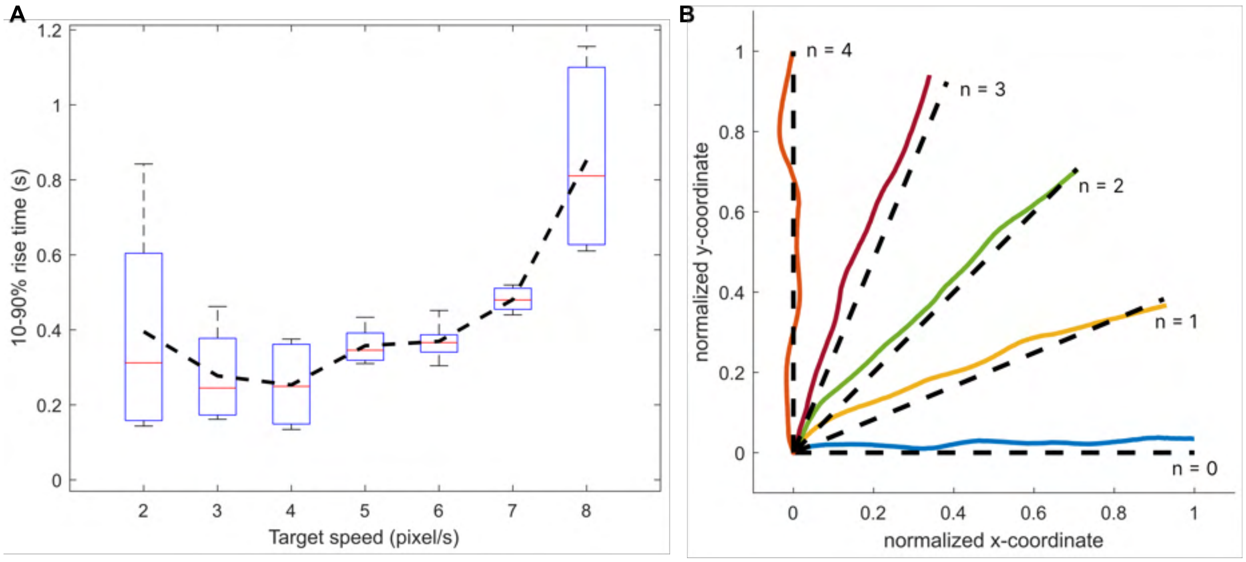

Figure 5.4: "Step response" results for uniform velocity fields. **(A)** The rise time to reach the target speed (from initial speed = 0) was typically less than 1 s. The box plot shows the median value in red, the 25 and 75 percentiles in blue, and outliers in black. The dashed black line indicates the mean rise time for each speed. $v = 4$ (equivalent to 24 cm/s on the sTISSUE) had both the lowest median and mean rise time of about 0.26 s. As the target speed increased, the rise time also increased and became less consistent across trials. **(B)** Mean trajectory across 6 trials for each direction. The results indicate the algorithm is able to drive the ball appropriately in each direction. However there is a slight tendency for the trajectories to move in the positive y-coordinate direction (n = 4).

5.4.2 Positional control

Positional control results for a single agent are shown in Fig. 5.5B. The ball was able to successfully navigate towards the goal across all 10 trials. Each trial is very consistent despite minor variations in the initial ball position. The spread of trajectories over the 10 trials is also very narrow; the difference between the outermost trajectories is roughly the same diameter as each pixel, which is the predicted upper performance limit. Some overshoot near the goal position is also observed; in these cases, the ball velocity was too high despite the commanded velocity magnitudes decreasing closer to the goal (Fig. 5.5A), resulting in an overshoot and then a correction back towards the goal. However, this only occurred in half of the trials.

When the additional agent is added to form a multi-agent system, the results are impacted in the same way that the KPF predicts (Fig. 5.6A). Because the second agent acts as a repulsor in the KPF, the velocity vectors are turned away from the agent as they would be from an obstacle;

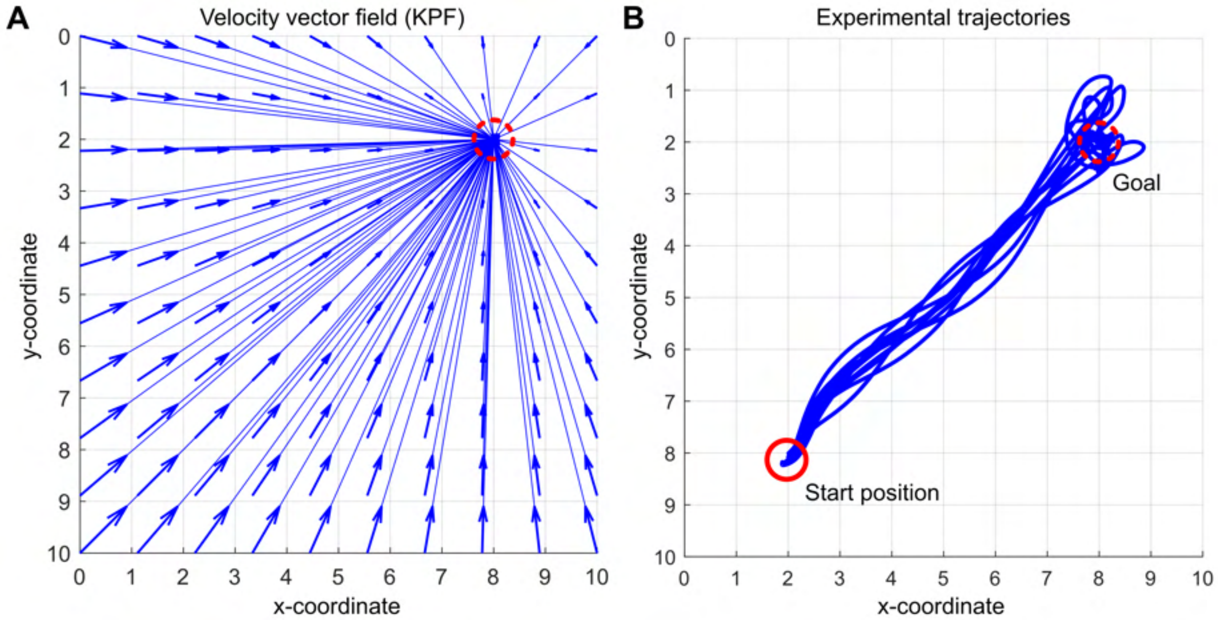

Figure 5.5: Experimental results for positional control of a single ball. **(A)** Velocity vector field used in the algorithm to direct the ball toward the goal position (8,2). **(B)** Trajectories over 10 trials using (2,8) as the starting ball position. Only slight deviations in the ball trajectory occur between trials. Some overshoot at the goal position is observed, but the algorithm enables the shape display to loop the ball back towards the goal.

as a result, all 10 trials show the trajectories veering from the straight-line path exhibited in Fig. 5.5 and instead avoiding the agent in the center position. This shows effective implementation of the multi-agent system as it can be used to avoid collisions between agents. The trajectories for this experiment exhibit a much wider spread and variability when compared to the single agent system, but the positional control KPF is just as effective in enabling the ball to reach the goal position.

5.4.3 Trajectory control

The algorithm demonstrates the ability to control the ball via global KPF specification. Instead of setting a particular goal position or requiring a parameterized time equation (i.e. where the goal position is a function of time), the KPF can be calculated through any desired set of equations. For the stable limit cycle equations which we tested, the algorithm enabled the ball to maintain its stable orbit according to the specified vector field (Fig. 5.7A).

The general trend shows the agent tracing out the desired trajectory over a period of 20 or-

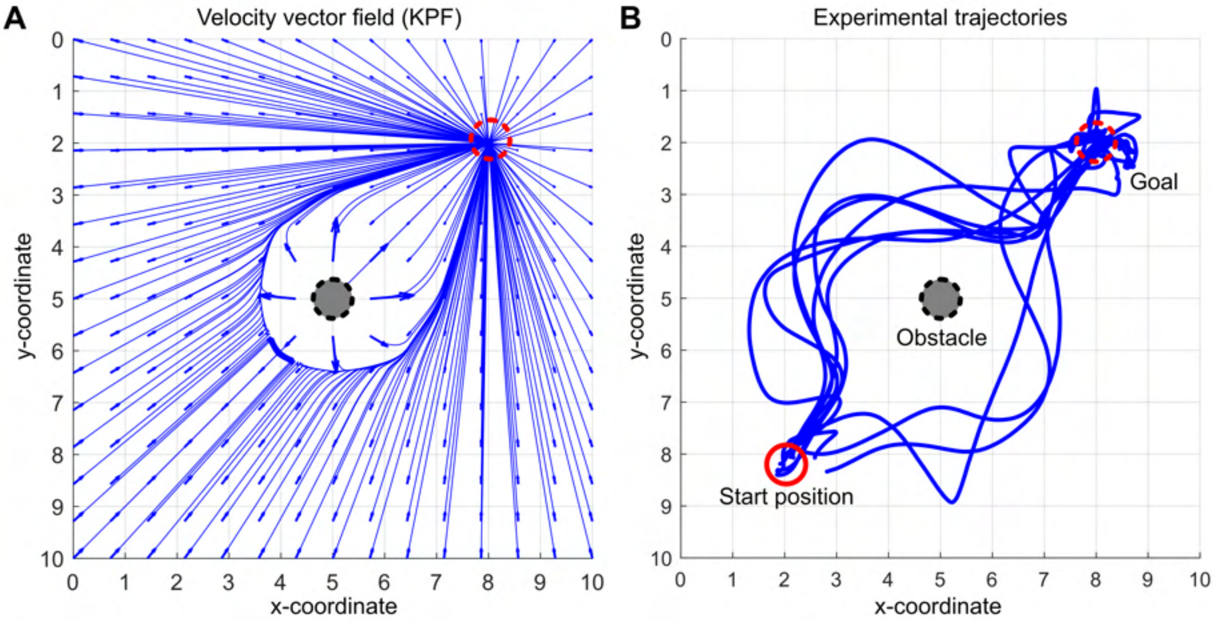

Figure 5.6: Experimental results for positional control with another agent (an obstacle) present on the surface. **(A)** Velocity vector field used in the algorithm to direct the ball toward the goal position (8,2) with a second static agent at (5,5). **(B)** Trajectories over 10 trials using (2,8) as the starting ball position. The repulsive APF field from the second agent drives the ball around the obstacle while still reaching the goal position. The exact initial conditions dictate whether the ball avoids the obstacle towards the left or right side.

bits/cycles. However, the radius of the ball trajectory is oscillatory within the stable region. This is likely due to the magnitude of the velocity vectors within the stable region being smaller than the magnitudes outside of the region. The larger magnitudes result in an increased tendency to overshoot the desired velocity, resulting in an oscillatory trajectory instead of the ideally circular one. This also increases the variability and spread of trajectories beyond the stable region; i.e., the trace of orbits has a diameter greater than 1 pixel.

5.4.4 Formation control

Formation control of three agents is shown in Fig. 5.8. This demonstration shows that multi-agent formation control is achievable with the algorithm; the results show the triangle formed by the three ball positions has the desired area and side lengths, which corresponds to the desired triangle shape. The results tend to be oscillatory just like the limit cycle results in Fig. 5.7; similar to that scenario, this is due to the overshoot caused by the algorithm. This is also amplified by a "rubber-band" effect created by the formation control algorithm: since the attractor for each agent

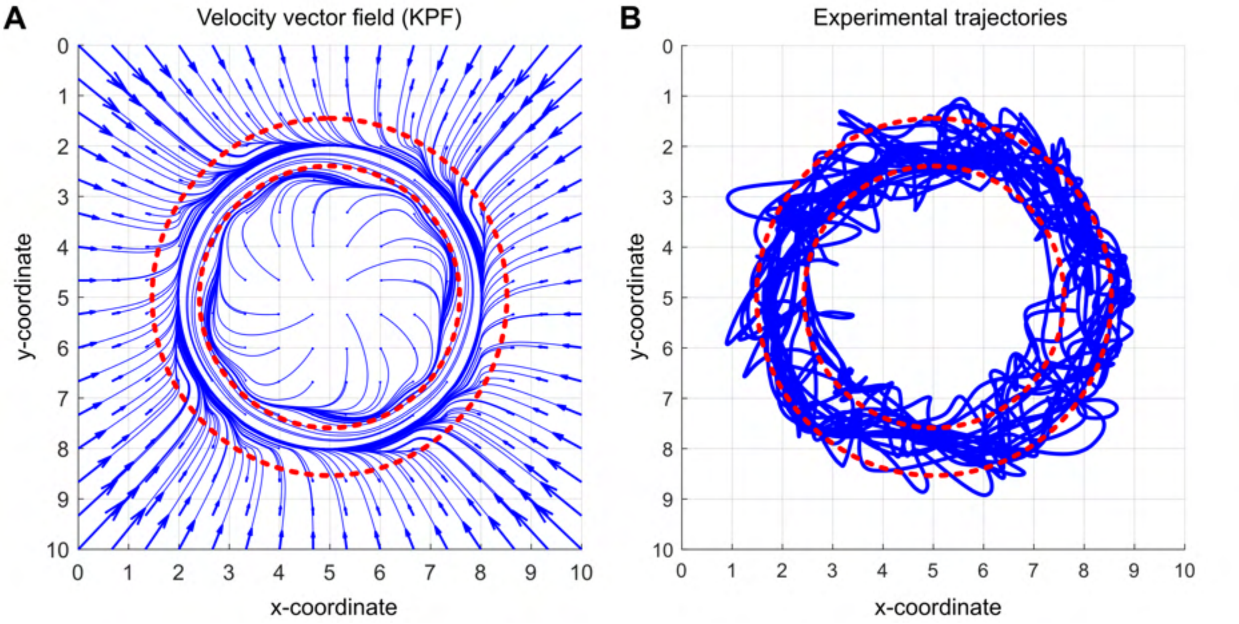

Figure 5.7: Experimental results for global trajectory control in the form of a stable limit cycle. **(A)** Velocity vector field of the stable limit cycle with a region of stability between radius 2.5 and 3.5, centered on (5,5). **(B)** Trajectories of 20 cycles around the limit cycle following the KPF. The ball is generally able to be kept within the stable region; any deviations outside of the orbit are returned. Over a period of 20 cycles, this also experimentally validates the stability of the algorithm in a Lyapunov sense.

is the geometric centroid of all agents, the deviation of an agent away from its position will move the centroid and thus ”pull” the other agents in that direction.

Formation control can also be combined with the other demonstrated KPFs. For example, instead of all agents following the formation-based KPF (i.e. other agents are repulsors, centroid is an attractor), one of the agents in the group can follow a positional control KPF. In this scenario, the agent in question will ’ignore’ the other agents on the surface, instead following the simple attractor to reach the goal position. Meanwhile, the other agents in the system will maintain formation control and move with the positional-controlled agent in the desired formation. This approach solves the aforementioned ”rubber-banding” problem, as one of the agents becomes unaffected by changes in the geometric centroid of the formation. The positional-controlled agent could also instead follow a trajectory-based KPF or other KPFs, enabling spatial and pose control of the formation.

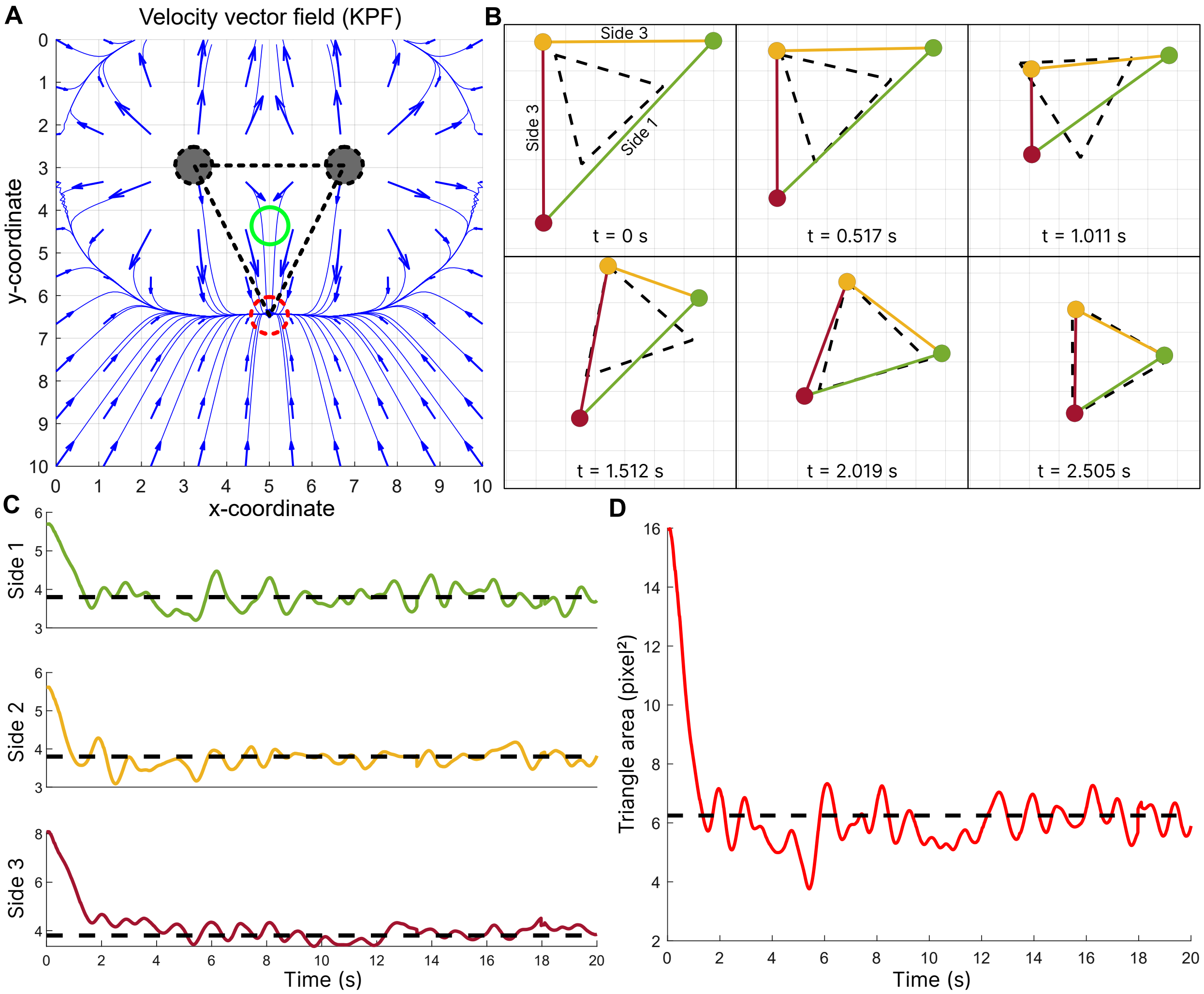

Figure 5.8: Formation control using three agents to form an equilateral triangle. **(A)** Velocity field created by summing the repulsive forces from two agents (solid gray circles) and the attractive force toward the centroid (green circle). The zero velocity position (KPF minimum) occurs at the vertex of the equilateral triangle. **(B)** Snapshots of the shape formed by the 3 balls (dashed line triangle) versus the target formation (solid line triangle) for a single trial. The target shape is achieved in 2.5 seconds. **(C)** Mean triangle side length (pixel) over time across seven trials. The target side length for the triangle is 3.8 pixel on each side. Just as with the triangle area, the algorithm is able to stabilize around the desired triangle side length for all three sides, forming an equilateral triangle of the desired size. **(D)** Mean triangle area over time across seven trials. The target area for the equilateral triangle is 6.25 pixel^2. The algorithm is able to achieve and maintain stability around the equilibrium area.

5.5 Discussion

In this chapter we've described and demonstrated a two-layer potential field algorithm to manipulate the position, velocities, and trajectories of balls on the surface of the sTISSUE array. The key component of the algorithm is the conversion from a velocity vector field to a potential energy field realized via deformation of the shape display. In particular, we present four distinct capabilities which stem from the base algorithm: (1) positional control of a ball with no dead-lock, (2) global trajectory control of a ball, (3) multi-agent/multi-ball simultaneous control and avoidance, and (4) formation control of a multi-agent system.

Our experimental results verify the success of the algorithm in achieving all four capabilities. We achieve a rapid velocity control with step response rise times on the order of 0.5 seconds as well as directional control which is accurate regardless of the orientation of the field to the grid of shape display pixels. We also validated the ability to control the position of a ball with and without a second agent on the surface, the ability to control the global trajectory of the ball with reasonable precision, and the ability to control formations of multiple balls interacting on the shape display.

5.5.1 Future experiments and improvements

While the exhibited results indicate that the algorithm and implementation is successful, there are other experiments that could further evaluate the performance as well as many improvements that could enhance the speed and accuracy of the system.

The formation control in particular is an interesting application which can be explored in the future. Initial next steps are to test interactions with additional agents, like a five-agent system (Fig. 5.9). Then, alternative formation control approaches may be conceived using the KPF as the basis. The shape display and ball system can potentially serve as a model to test algorithms for other, more complicated spatial formations (like spacecraft/satellite formations or submersible robotic formations).

In addition, there are other approaches to improve the performance of the algorithm on shape displays like sTISSUE, which feature uneven surfaces and actuation. The topology variability across the surface results in a constant input of disturbances into the motion of the ball when compared to rolling across a perfectly flat surface. Some approaches to address this problem include an adaptive

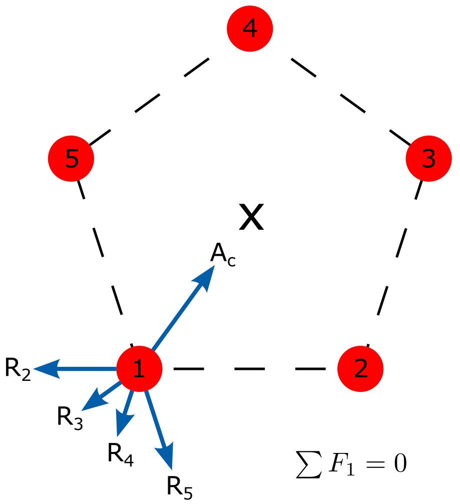

Figure 5.9: Formation shape control of a five-agent system. Agent #1 experiences repulsive forces from Agents #2-5 and an attractive force toward the geometric centroid. The equilibrium position exists at the vertex of the polygon. While this work only demonstrates formation control using up to three agents, future work could expand on these concepts for interactions with many more agents in different ways.

control scheme [209], where the algorithm parameters (e.g. a_v, α, etc.) are tuned in real-time to account for surface disturbances. Another approach could be dynamic mode decomposition (DMD) [210] control using data of the ball moving across the surface in different regions and directions. Using this data, a spatial DMD controller might be derived which accounts for the various disturbances in each region of the shape display. Since the unevenness of the surface is general static/consistent, these disturbances can be accurately mapped through trial data before implementing the algorithm, resulting in much greater velocity tracking for the ball. Lastly, machine learning approaches [211] could also be used as another data-driven control mode to generate the appropriate PPF. These strategies could also be used for other control algorithms implemented on robotic materials such as sTISSUE.

5.5.2 Alternative repulsor approaches

While we present a complete analysis and performance quantification of the two-layer APF algorithm using a 2D Gaussian function to build the PPF, other PPF forms can also be implemented. Here we discuss alternative approaches as well as their strengths and weaknesses when compared to the 2D Gaussian repulsor. Note that we merely present these as other approaches which could be implemented in future work; no quantification of the efficacy of these approaches is provided.

"Trough" repulsor

A "trough"-shaped repulsor is built such that the PPF (and thus the shape display surface) forms a valley from the ball position to the goal. The walls of the valley must be at least the diameter of the ball, allowing the ball to roll within this channel. The shape keeps the ball trajectory stable because a greater amount of energy is required to roll up the walls of the trough. The surface rises from behind the ball to propagate the ball forward through the trough.

This approach has a greater guarantee of trajectory stability because the trough traces out a valley along the entire trajectory, keeping the ball more centered on the desired path. However, it is much less energy efficient compared to the 2D Gaussian because the majority of the surface must be active to form the trough. Because HASEL actuators only expand and cannot contract, the trough must be formed by expanding all of the HASEL actuators on the side walls of the trough. In addition, good velocity tracking to the KPF is also not guaranteed as the ball can freely move forward on the trajectory formed by the trough. Lastly, the trough approach does not work as well with multiple balls on the surface because the troughs formed from each ball may intersect each other and produce unwanted interactions.

"Inverted Gaussian" attractor

Another repulsor approach is an inverted 2D Gaussian. In our algorithm, we present a PPF repulsor which "sticks out" from a flat surface; it acts as a source of potential energy. The inverted Gaussian is a potential energy sink which "sinks into" the surface. In this case it is appropriate to call it an attractor rather than a repulsor because the key surface feature has a lower potential energy than its surroundings.

The result is much greater stability for the ball trajectory. The rising walls of the inverted Gaussian keep the ball contained within the sink; any deviation from the desired trajectory will tend back towards the center (compared to the upright 2D Gaussian where a deviation will move the ball further away from the desired position). However, the stability of this shape may inhibit multi-agent control because the 'sink' which drives one agent may easily trap another agent if it is too close. Once the two agents are in close proximity it becomes more challenging to separate them using this PPF.

This PPF shape also requires the largest amount of energy of the proposed methods since the majority of actuators on the surface are active. However, for shape displays in which the actuators begin in an "expanded" form and contract via application of power, this PPF would be similarly efficient to the positive Gaussian we use, and would come with the additional stability benefits.

"Arced Gaussian" repulsor

The last alternative repulsor approach is an arc segment with a Gaussian cross-section, shown in Fig. 4.9B of Chapter 4. Like the inverted Gaussian and trough repulsor, the arced Gaussian enforces greater stability of the ball trajectory. However, the arc shape may introduce additional disturbances between agents in a multi-agent system, which is why it was not chosen for this algorithm.

5.6 Conclusions

In this work we proposed a new application of artificial potential fields (APFs) in the realm of shape-display object manipulation and demonstrated its efficacy on the sTISSUE array from Chapter 4. Using a two-layer APF algorithm which keeps attractive and repulsive fields separate, we designed a dead-lock-free system for point-to-point control of a ball rolling across the surface and extended this concept to trajectory control and multi-agent systems. The algorithm and its potential applications were validated using the sTISSUE robotic material. The results show that the two-layer APF algorithm accurately controls single ball and multi-ball position on the surface, controls global trajectories such as stable limit cycles, and enables multi-agent formation control in the form of an equilateral triangle formation. This research provides a promising approach to global object manipulation with shape displays and also suggests new applications for artificial potential fields for robotic materials like sTISSUE. In the future, this work could enable industrial-scale shape-display object manipulation for manufacturing or assembly processes. For applications within robotic materials, this work shows that artificial potential field theory for global control and trajectory synthesis is a promising approach to coordinate the control of each individual cell.

5.7 Acknowledgements and contributions

As the work presented in this chapter is the result of collaboration with multiple researchers, here I describe the contributions of each team member for clarity. For contributions related to the use of the sTISSUE material, please see Chapter 4. The conceptualization of this work was done by myself, Sean Humbert, and Mark E. Rentschler. Software used in data collection and closed-loop control was written by myself and Mantas Naris.

In addition to the above, I created the two-layer PF algorithm and its multiple capabilities, performed all data collection and data visualization, and all mathematical modeling described in this chapter.

Chapter 6

Conclusions

6.1 Results to date

In this thesis I have described several contributions to the development and control of soft robotic materials driven by HASEL actuators. In Chapter 2, I showed how nonlinear foldable HASEL actuators can be modeled using simple linear frequency response tests. I demonstrated that the dynamic response of a folded HASEL actuator is approximately separate from its static response and that the dynamics are consistent between copies of actuators. Using this model, I designed a dual-mode PID controller for real-time closed loop feedback control. An elastomeric strain sensor was integrated onto the actuator to enable compact closed loop control which achieved step responses with faster rise times and settling times compared to the open loop. Using this actuator model and dual-mode controller, more complex robotic systems driven by foldable HASEL actuators can be controlled. In the broader context, this work serves as a basis for the future development, control, and analysis of high-DOF soft robots in Chapters 3 and 4.

Chapter 3 expands from the single-actuator-sensor system to a system driven by multiple HASEL actuators with feedback from multiple sensors. Using a new magnetic sensing mechanism for HASEL actuators described by Sundaram et al. [153] and the system identification techniques described in Chapter 2, I derived a controller for a folded HASEL actuator using the integrated magnetic sensor for closed loop feedback. I demonstrated multi-sensor, multi-actuator control of a deforming platform built from six sets of HASEL actuators and magnetic sensors. I also implemented a new kinematics approach for end-effector estimation to enable greater control over the system's end-effector. This demonstrates potential approaches for developing and controlling multi-actuator soft robots and highlights the advantage of magnetic-based sensing compared to the capacitive-based sensors in Chapter 2.

The concepts presented thus far were fully realized in the development of sTISSUE, a soft robotic material combining actuation, sensing, and control, which was presented in Chapter 4. Following the design philosophy of robotic materials, sTISSUE uses a hierarchical structure with a basic "cell" that is repeated in a structural matrix to enable higher functionality through structure and organization. Each cell contains a folded HASEL actuator, magnetic sensor from Sundaram et al. [153], and a driving circuit to control the actuator voltage. Higher levels of the hierarchy distribute power and control signals among the cells, with the highest level being the global control scheme implemented on a central computer. I designed a voltage regulation algorithm to control the voltage of HASEL actuators from the driving circuit, and used loop shaping techniques to design a displacement feedback controller using the magnetic sensing mechanism. The inner voltage regulation loop on each cell has a bandwidth of 200 Hz and the outer displacement feedback loop a bandwidth of 20 Hz, although 30 Hz motion is demonstrated. A 10x10 grid of 100 sTISSUE cells was used to construct an intelligent soft shape display. Using the sensor feedback and high actuation frequency, I demonstrated multiple applications and functionalities of sTISSUE. This soft robotic material shows exciting promise in the development of more advanced soft robots as well as new advances in research. In the context of the broader soft robotics field, sTISSUE is the first step towards intelligent soft robotic materials which can bring soft robot functionality closer to biology.

Using the sTISSUE shape display as a test platform, Chapter 5 describes the creation of a novel control algorithm to further enhance the object manipulation capabilities of robotic materials. I applied two artificial potential field layers to enable closed loop velocity control of balls on shape displays without dead-lock for a single ball case. The algorithm is extended to velocity control of multiple balls including basic shape formations between balls. I demonstrated positional control and global trajectory control of a ball on the surface using the sTISSUE shape display. I also experimentally validated the algorithm performance including stability and robustness. This novel technique promotes further object manipulation work on shape displays and robotic materials in general, and could be applied to other existing shape displays as well. The work also promotes sTISSUE as a useful robotic material for scientific research and for industrial applications in object conveyance.

All of these contributions show the promise of robots developed with hydraulically amplified self-healing electrostatic actuators, as well as the promise of soft robotic materials as a whole. Robotic materials like sTISSUE will no doubt generate excitement in the robotics community, which may result in further research in these areas. Further improvement of these robotic materials can lead to the creation of advanced soft robots with real-world capabilities and applications.

6.2 Immediate next steps

Based on the work presented in this thesis and the shortcomings present (described in each relevant chapter), there are a few immediate next steps that can be implemented. The first is the design of alternate-topology robots using sTISSUE. While Chapter 4 presents a shape display driven by sTISSUE, we leave alternate designs to future work. The current hardware and software could be adapted to a variety of geometries, for example a cylindrical device with each cell pointed inwards, forming a "peristaltic" device. Other 3D devices like a deforming cube or sphere could also be implemented. The only hardware changes required are in the support structure of the modules (Chapter 4 presents a 1x10 planar sTISSUE module with a rigid Delrin backing; this could be replaced without altering any circuitry or software).

sTISSUE can also be extended to entirely different morphologies, particularly by changing the geometry of actuation. For example, a soft robotic arm or bipedal leg system could be constructed with sTISSUE. To do so, the linearly expanding folded HASEL actuators could be replaced by contracting Peano-HASEL actuators [78] which can act as antagonistic muscle pairs in the robotic limb [95]. Because the operating voltages and other characteristics are similar to the folded HASEL actuators used in the current sTISSUE design, it can be easy to change to an alternate form of actuation without changing the HV drivers. Because we have already demonstrated an sTISSUE system using up to 100 actuators and sensors, there are no constraints on the number of artificial muscles or DOF that could be designed into the robot limb. The sTISSUE-driven robotic limb could incorporate multiple motions like pronation/supination in addition to arm flexion and extension [187, 212, 213]. This is only one example which highlights the potential applications and next steps for soft robotic materials.

With these new morphologies developed, alternate control approaches can also be devised. The potential field approach demonstrated in Chapter 5 can also be applied to robotic manipulators like our proposed robotic sTISSUE limb [214]. Alternative approaches like those mentioned in Chapter

5 (dynamic mode decomposition, adaptive control, and machine learning) can also be applied to sTISSUE-driven devices. Most likely, control will be implemented through a combination of methods at a variety of scales (single cell, module level, and device level).

6.3 Future potential and challenges

While this thesis describes significant progress in the development of soft robotic systems using HASEL actuators, many grander challenges must still be overcome before even more complex systems can be built. Addressing these challenges will push electrostatic soft actuators and robotic materials to the forefront of the scientific field and eventually promote their use in a broad range of applications in our society.

Despite the best efforts of robotics researchers, even simple biological organisms possess many more capabilities and greater intelligence than today's state-of-the-art robots of the same size and weight. This technological gap is not only explained by the miniaturization of actuation, sensing, and control which takes place at a cellular level within biology (when compared to robotic systems), but is also explained by the hierarchical organization of the cells, as well as through embodied intelligence and emergent properties that arise by their arrangement [106]. This is why intelligent robotic materials, which draw inspiration from this natural design philosophy, hold promise in helping soft robots become closer in scope and functionality to these biological systems.

If soft robotic materials can become more tightly integrated and miniaturized compared to the current state of the art (such as sTISSUE, with a 6 cm x 6 cm x 9 cm cell size), greater functionality and capabilities are possible. As a whole, the miniaturization of soft robotic materials infers the miniaturization of actuator arrays, sensor arrays, as well as computation and control circuitry. Additional challenges include shielding of the high voltage systems from low voltage electronics within such a system, the development of more robust interfaces between soft and rigid components, and control design to drive the robotic cells both at the individual- and device-level scales. This approach is not dissimilar from the biological control organization of cells, tissues, organs, and organisms.

Addressing these challenges requires advancements on several fronts; materials science breakthroughs are required to advance the efficiency of high voltage systems, the force and strain outputs of HASEL actuators, and the resolution and sensitivity of state sensors; mechanical design breakthroughs are necessary to improve the actuation bandwidth of HASEL actuators and improve integration between soft and rigid components; control breakthroughs are necessary to coordinate global motion of robotic materials with 100s of actuators and sensors; and manufacturing breakthroughs are needed to enable the rapid and consistent production of actuators, sensors, and circuitry at an ever-decreasing size.

Like many scientific pursuits, these goals are ever advancing; as robotic materials continue to miniaturize or become more complex, continual breakthroughs are required to make such systems even more tightly integrated, more efficient, and more functional. The developments outlined in this thesis are only one step in that direction. Perhaps with increased scientific interest and interdisciplinary cooperation among robotics experts, electrostatic soft robotic materials may one day enable life-like robots which can outperform the biological systems that inspired their creation.

Bibliography

[1] J. Wallén, *The history of the industrial robot.* Linköping University Electronic Press, 2008.

[2] C. Dirican, "The impacts of robotics, artificial intelligence on business and economics," *Procedia-Social and Behavioral Sciences*, vol. 195, pp. 564–573, 2015.

[3] J. Hudson, *The Robot Revolution.* Edward Elgar Publishing, 2019.

[4] G. Dogangil, B. L. Davies, and F. Rodriguez y Baena, "A review of medical robotics for minimally invasive soft tissue surgery," *Proceedings of the Institution of Mechanical Engineers, Part H: Journal of Engineering in Medicine*, vol. 224, no. 5, pp. 653–679, 2010.

[5] G. M. Whitesides, "Soft Robotics," *Angewandte Chemie International Edition*, vol. 57, no. 16, pp. 4258–4273, 2018.

[6] M. Calisti, G. Picardi, and C. Laschi, "Fundamentals of soft robot locomotion," *Journal of The Royal Society Interface*, vol. 14, no. 130, 2017.

[7] N. Elango and A. A. M. Faudzi, "A review article: investigations on soft materials for soft robot manipulations," *The International Journal of Advanced Manufacturing Technology*, vol. 80, no. 5, pp. 1027–1037, 2015.

[8] S. Kim, C. Laschi, and B. Trimmer, "Soft robotics: a bioinspired evolution in robotics," *Trends in Biotechnology*, vol. 31, no. 5, pp. 287–294, 2013.

[9] C. Lee, M. Kim, Y. J. Kim, N. Hong, S. Ryu, H. J. Kim, and S. Kim, "Soft robot review," *International Journal of Control, Automation and Systems*, vol. 15, no. 1, pp. 3–15, 2017.

[10] B. Mazzolai, F. Carpi, K. Suzumori, M. Cianchetti, T. Speck, S. K. Smoukov, I. Burgert, T. Keplinger, G. Siqueira, F. Vanneste, *et al.*, "Roadmap on soft robotics: multifunctionality, adaptability and growth without borders," *Multifunctional Materials*, 2022.

[11] D. Trivedi, C. D. Rahn, W. M. Kier, and I. D. Walker, "Soft robotics: Biological inspiration, state of the art, and future research," *Applied Bionics and Biomechanics*, vol. 5, no. 3, pp. 99–117, 2008.

[12] M. Cianchetti, C. Laschi, A. Menciassi, and P. Dario, "Biomedical applications of soft robotics," *Nature Reviews Materials*, vol. 3, no. 6, pp. 143–153, 2018.

[13] E. T. Roche, M. A. Horvath, I. Wamala, A. Alazmani, S.-E. Song, W. Whyte, Z. Machaidze, C. J. Payne, J. C. Weaver, G. Fishbein, J. Kuubler, N. V. Vasilyev, D. J. Mooney, F. A. Pigula, and C. J. Walsh, "Soft Robotic Sleeve Restores Heart Function," *Science Translational Medicine*, vol. 9, no. 373, 2017. Art. no. eaaf3925.

[14] X. Yang, C. An, S. Liu, T. Cheng, V. Bunpetch, Y. Liu, S. Dong, S. Li, X. Zou, T. Li, H. Ouyang, Z. Wu, and W. Yang, "Soft Artificial Bladder Detrusor," *Advanced Healthcare Materials*, vol. 7, no. 6, pp. 1–9, 2018.

[15] A. De Greef, P. Lambert, and A. Delchambre, "Towards flexible medical instruments: Review of flexible fluidic actuators," *Precision engineering*, vol. 33, no. 4, pp. 311–321, 2009.

[16] P. Maeder-York, T. Clites, E. Boggs, R. Neff, P. Polygerinos, D. Holland, L. Stirling, K. Galloway, C. Wee, and C. Walsh, "Biologically inspired soft robot for thumb rehabilitation," *Journal of Medical Devices*, vol. 8, no. 2, 2014.

[17] H. Wang, R. Zhang, W. Chen, X. Wang, and R. Pfeifer, "A cable-driven soft robot surgical system for cardiothoracic endoscopic surgery: preclinical tests in animals," *Surgical Endoscopy*, vol. 31, no. 8, pp. 3152–3158, 2017.

[18] H. Abidi, G. Gerboni, M. Brancadoro, J. Fras, A. Diodato, M. Cianchetti, H. Wurdemann, K. Althoefer, and A. Menciassi, "Highly dexterous 2-module soft robot for intra-organ navigation in minimally invasive surgery," *The International Journal of Medical Robotics and Computer Assisted Surgery*, vol. 14, no. 1, 2018.

[19] T. Q. Trung and N. E. Lee, "Flexible and Stretchable Physical Sensor Integrated Platforms for Wearable Human-Activity Monitoring and Personal Healthcare," *Advanced Materials*, vol. 28, no. 22, pp. 4338–4372, 2016.

[20] C. T. O'Neill, N. S. Phipps, L. Cappello, S. Paganoni, and C. J. Walsh, "A soft wearable robot for the shoulder: Design, characterization, and preliminary testing," in *2017 International Conference on Rehabilitation Robotics (ICORR)*, (London, United Kingdom), pp. 1672–1678, July 2017.

[21] H. In, B. B. Kang, M. Sin, and K.-J. Cho, "Exo-glove: A wearable robot for the hand with a soft tendon routing system," *IEEE Robotics and Automation Magazine*, vol. 22, no. 1, pp. 97–105, 2015.

[22] S. Park and S. Jayaraman, "Enhancing the quality of life through wearable technology," *IEEE Engineering in medicine and biology magazine*, vol. 22, no. 3, pp. 41–48, 2003.

[23] D. Rus and M. T. Tolley, "Design, fabrication and control of soft robots," *Nature*, vol. 521, no. 7553, pp. 467–475, 2015.

[24] N. Tsagarakis, M. Laffranchi, B. Vanderborght, and D. Caldwell, "A compact soft actuator unit for small scale human friendly robots," in *IEEE International Conference on Robotics and Automation*, (Kobe, Japan), pp. 4356–4362, May 2009.

[25] P. Polygerinos, N. Correll, S. A. Morin, B. Mosadegh, C. D. Onal, K. Petersen, M. Cianchetti, M. T. Tolley, and R. F. Shepherd, "Soft robotics: Review of fluid-driven intrinsically soft devices; manufacturing, sensing, control, and applications in human-robot interaction," *Advanced Engineering Materials*, vol. 19, no. 12, 2017.

[26] A. Bicchi, G. Tonietti, and E. Piaggio, "Design, realization and control of soft robot arms for intrinsically safe interaction with humans," in *Proc. IARP/RAS Workshop on Technical Challenges for Dependable Robots in Human Environments*, (Nagoya University, Japan), pp. 79–87, June 2002.

[27] M. T. Tolley, R. F. Shepherd, B. Mosadegh, K. C. Galloway, M. Wehner, M. Karpelson, R. J. Wood, and G. M. Whitesides, "A resilient, untethered soft robot," *Soft robotics*, vol. 1, no. 3, 2014.

[28] C. Laschi, B. Mazzolai, and M. Cianchetti, "Soft robotics: Technologies and systems pushing the boundaries of robot abilities," *Science Robotics*, vol. 1, no. 1, 2016.

[29] R. A. Bilodeau and R. K. Kramer, "Self-healing and damage resilience for soft robotics: a review," *Frontiers in Robotics and AI*, vol. 4, 2017.

[30] U. Gupta, L. Qin, Y. Wang, H. Godaba, and J. Zhu, "Soft robots based on dielectric elastomer actuators: a review," *Smart Materials and Structures*, vol. 28, no. 10, 2019.

[31] Z. Shen, J. Na, and Z. Wang, "A biomimetic underwater soft robot inspired by cephalopod mollusc," *IEEE Robotics and Automation Letters*, vol. 2, no. 4, pp. 2217–2223, 2017.

[32] M. Cianchetti, M. Calisti, L. Margheri, M. Kuba, and C. Laschi, "Bioinspired locomotion and grasping in water: the soft eight-arm octopus robot," *Bioinspiration and Biomimetics*, vol. 10, no. 3, 2015.

[33] R. F. Shepherd, F. Ilievski, W. Choi, S. A. Morin, A. A. Stokes, A. D. Mazzeo, X. Chen, M. Wang, and G. M. Whitesides, "Multigait soft robot," *Proceedings of the National Academy of Sciences of the United States of America*, vol. 108, no. 51, pp. 20400–20403, 2011.

[34] E. W. Hawkes, L. H. Blumenschein, J. D. Greer, and A. M. Okamura, "A soft robot that navigates its environment through growth," *Science Robotics*, vol. 2, no. 8, pp. 1–8, 2017.

[35] N. D. Naclerio, A. Karsai, M. Murray-Cooper, Y. Ozkan-Aydin, E. Aydin, D. I. Goldman, and E. W. Hawkes, "Controlling subterranean forces enables a fast, steerable, burrowing soft robot," *Science Robotics*, vol. 6, no. 55, pp. 1–12, 2021.

[36] C. Wright, A. Johnson, A. Peck, Z. McCord, A. Naaktgeboren, P. Gianfortoni, M. Gonzalez-Rivero, R. Hatton, and H. Choset, "Design of a modular snake robot," in *2007 IEEE/RSJ International Conference on Intelligent Robots and Systems*, (San Diego, California), pp. 2609–2614, October 2007.

[37] A. D. Marchese, C. D. Onal, and D. Rus, "Autonomous Soft Robotic Fish Capable of Escape Maneuvers Using Fluidic Elastomer Actuators," *Soft Robotics*, vol. 1, no. 1, pp. 75–87, 2014.

[38] J. Shintake, V. Cacucciolo, H. Shea, and D. Floreano, "Soft biomimetic fish robot made of dielectric elastomer actuators," *Soft Robotics*, vol. 5, no. 4, pp. 466–474, 2018.

[39] L. Shui, L. Zhu, Z. Yang, Y. Liu, and X. Chen, “Energy efficiency of mobile soft robots,” *Soft Matter*, vol. 13, no. 44, pp. 8223–8233, 2017.

[40] C. Laschi, M. Cianchetti, B. Mazzolai, L. Margheri, M. Follador, and P. Dario, “Soft robot arm inspired by the octopus,” *Advanced Robotics*, vol. 26, no. 7, pp. 709–727, 2012.

[41] W. McMahan, B. A. Jones, and I. D. Walker, “Design and implementation of a multi-section continuum robot: Air-octor,” in *2005 IEEE/RSJ International Conference on Intelligent Robots and Systems*, (Edmonton, AB, Canada), pp. 2578–2585, August 2005.

[42] Z. Wang, Y. Torigoe, and S. Hirai, “A prestressed soft gripper: design, modeling, fabrication, and tests for food handling,” *IEEE Robotics and Automation Letters*, vol. 2, no. 4, pp. 1909–1916, 2017.

[43] K. C. Galloway, K. P. Becker, B. Phillips, J. Kirby, S. Licht, D. Tchernov, R. J. Wood, and D. F. Gruber, “Soft Robotic Grippers for Biological Sampling on Deep Reefs,” *Soft Robotics*, vol. 3, no. 1, pp. 23–33, 2016.

[44] P. Polygerinos, Z. Wang, K. C. Galloway, R. J. Wood, and C. J. Walsh, “Soft robotic glove for combined assistance and at-home rehabilitation,” *Robotics and Autonomous Systems*, vol. 73, pp. 135–143, 2015.

[45] S. M. Mirvakili and I. W. Hunter, “Artificial Muscles: Mechanisms, Applications, and Challenges,” *Advanced Materials*, vol. 30, no. 6, pp. 1–28, 2018.

[46] X. Ke, J. Jang, Z. Chai, H. Yong, J. Zhu, H. Chen, C. F. Guo, H. Ding, and Z. Wu, “Stiffness preprogrammable soft bending pneumatic actuators for high-efficient, conformal operation,” *Soft Robotics*, vol. 9, no. 3, pp. 613–624, 2021.

[47] A. D. Marchese, R. K. Katzschmann, and D. Rus, “A recipe for soft fluidic elastomer robots,” *Soft robotics*, vol. 2, no. 1, pp. 7–25, 2015.

[48] O. Ivlev, “Soft fluidic actuators of rotary type for safe physical human-machine interaction,” in *2009 IEEE International Conference on Rehabilitation Robotics*, (Kyoto, Japan), pp. 1–5, June 2009.

[49] T. Helps and J. Rossiter, "Proprioceptive flexible fluidic actuators using conductive working fluids," *Soft robotics*, vol. 5, no. 2, pp. 175–189, 2018.

[50] P. Boyraz, G. Runge, and A. Raatz, "An overview of novel actuators for soft robotics," in *Actuators*, vol. 7, p. 48, Multidisciplinary Digital Publishing Institute, 2018.

[51] M. Zhu, T. N. Do, E. Hawkes, and Y. Visell, "Fluidic fabric muscle sheets for wearable and soft robotics," *Soft robotics*, vol. 7, no. 2, pp. 179–197, 2020.

[52] A. Villoslada, A. Flores, D. Copaci, D. Blanco, and L. Moreno, "High-displacement flexible shape memory alloy actuator for soft wearable robots," *Robotics and Autonomous Systems*, vol. 73, pp. 91–101, 2015.

[53] I. Apsite, S. Salehi, and L. Ionov, "Materials for smart soft actuator systems," *Chemical Reviews*, vol. 122, no. 1, pp. 1349–1415, 2022.

[54] X. Cao, M. Zhang, Z. Zhang, Y. Xu, Y. Xiao, and T. Li, "Review of soft linear actuator and the design of a dielectric elastomer linear actuator," *Acta Mechanica Solida Sinica*, vol. 32, no. 5, pp. 566–579, 2019.

[55] H. Rodrigue, W. Wei, B. Bhandari, and S.-H. Ahn, "Fabrication of wrist-like sma-based actuator by double smart soft composite casting," *Smart Materials and Structures*, vol. 24, no. 12, 2015.

[56] J. M. Jani, M. Leary, A. Subic, and M. A. Gibson, "A review of shape memory alloy research, applications and opportunities," *Materials & Design (1980-2015)*, vol. 56, pp. 1078–1113, 2014.

[57] N. El-Atab, R. B. Mishra, F. Al-Modaf, L. Joharji, A. A. Alsharif, H. Alamoudi, M. Diaz, N. Qaiser, and M. M. Hussain, "Soft actuators for soft robotic applications: a review," *Advanced Intelligent Systems*, vol. 2, no. 10, 2020.

[58] A. O'Halloran, F. O'Malley, and P. McHugh, "A review on dielectric elastomer actuators, technology, applications, and challenges," *Journal of Applied Physics*, vol. 104, no. 7, p. 9, 2008.

[59] P. Brochu and Q. Pei, "Dielectric elastomers for actuators and artificial muscles," *Macromolecular Rapid Communications*, vol. 31, pp. 10–36, 2010.

[60] G. Y. Gu, J. Zhu, L. M. Zhu, and X. Zhu, "A survey on dielectric elastomer actuators for soft robots," *Bioinspiration and Biomimetics*, vol. 12, no. 1, 2017.

[61] Y. Guo, L. Liu, Y. Liu, and J. Leng, "Review of dielectric elastomer actuators and their applications in soft robots," *Advanced Intelligent Systems*, vol. 3, 2021.

[62] E. Leroy, R. Hinchet, and H. Shea, "Multimode hydraulically amplified electrostatic actuators for wearable haptics," *Advanced Materials*, vol. 32, no. 36, 2020.

[63] E. Acome, S. K. Mitchell, T. G. Morrissey, M. B. Emmett, C. Benjamin, M. King, M. Radakovitz, and C. Keplinger, "Hydraulically amplified self-healing electrostatic actuators with muscle-like performance," *Science*, vol. 359, no. 6371, pp. 61–65, 2018.

[64] N. Kellaris, V. Gopaluni Venkata, G. M. Smith, S. K. Mitchell, and C. Keplinger, "Peano-HASEL actuators: Muscle-mimetic, electrohydraulic transducers that linearly contract on activation," *Science Robotics*, vol. 3, no. 14, 2018. Art. no. eaar3276.

[65] R. Pelrine, P. Sommer-Larsen, R. D. Kornbluh, R. Heydt, G. Kofod, Q. Pei, and P. Gravesen, "Applications of dielectric elastomer actuators," in *Smart Structures and Materials 2001: Electroactive Polymer Actuators and Devices*, vol. 4329, pp. 335–349, SPIE, 2001.

[66] F. Carpi, C. Salaris, and D. De Rossi, "Folded dielectric elastomer actuators," *Smart Materials and Structures*, vol. 16, no. 2, 2007.

[67] Y. Tian, J. Liu, W. Wu, X. Liang, M. Pan, C. Bowen, Y. Jiang, J. Sun, T. McNally, D. Wu, *et al.*, "Peano-hydraulically amplified self-healing electrostatic actuators based on a novel bilayer polymer shell for enhanced strain, load, and rotary motion," *Advanced Intelligent Systems*, vol. 4, no. 5, 2022.

[68] J. He, Z. Chen, Y. Xiao, X. Cao, J. Mao, J. Zhao, X. Gao, T. Li, and Y. Luo, "Intrinsically anisotropic dielectric elastomer fiber actuators," *ACS Materials Letters*, vol. 4, pp. 472–479, 2022.

[69] J. Walker, T. Zidek, C. Harbel, S. Yoon, F. S. Strickland, S. Kumar, and M. Shin, "Soft robotics: a review of recent developments of pneumatic soft actuators," in *Actuators*, vol. 9, Multidisciplinary Digital Publishing Institute, 2020.

[70] S. Hoang, K. Karydis, P. Brisk, and W. H. Grover, "A pneumatic random-access memory for controlling soft robots," *Plos one*, vol. 16, no. 7, 2021.

[71] N. W. Bartlett, K. P. Becker, and R. J. Wood, "A fluidic demultiplexer for controlling large arrays of soft actuators," *Soft matter*, vol. 16, no. 25, pp. 5871–5877, 2020.

[72] L. Yao, R. Niiyama, J. Ou, S. Follmer, C. Della Silva, and H. Ishii, "Pneui: pneumatically actuated soft composite materials for shape changing interfaces," in *Proceedings of the 26th Annual ACM Symposium on User Interface Software and Technology*, (St. Andrews Scotland, United Kingdom), pp. 13–22, October 2013.

[73] M. T. Tolley, R. F. Shepherd, M. Karpelson, N. W. Bartlett, K. C. Galloway, M. Wehner, R. Nunes, G. M. Whitesides, and R. J. Wood, "An untethered jumping soft robot," in *2014 IEEE/RSJ International Conference on Intelligent Robots and Systems*, (Chicago, Illinois), pp. 561–566, September 2014.

[74] C. Jin, J. Zhang, Z. Xu, I. Trase, S. Huang, L. Dong, Z. Liu, S. E. Usherwood, J. X. Zhang, and Z. Chen, "Tunable, flexible, and resilient robots driven by an electrostatic actuator," *Advanced Intelligent Systems*, vol. 2, no. 3, 2020.

[75] I.-D. Sîrbu, G. Moretti, S. Dirè, L. Fambri, R. Vertechy, D. Meniglio, and M. Fontana, "Electrostatic actuator for tactile display based on hydraulically coupled dielectric fluids and soft structures," in *Electroactive Polymer Actuators and Devices (EAPAD) XXI*, vol. 10966, (Denver, Colorado), pp. 334–339, March 2019.

[76] R. Zengerle, A. Richter, and H. Sandmaier, "A micro membrane pump with electrostatic actuation," in *[1992] Proceedings IEEE Micro Electro Mechanical Systems*, (Travemunde, Germany), pp. 19–24, IEEE, February 1992.

[77] R. S. Diteesawat, T. Helps, M. Taghavi, and J. Rossiter, "Electro-pneumatic pumps for soft robotics," *Science robotics*, vol. 6, no. 51, 2021.

[78] X. Wang, S. K. Mitchell, E. H. Rumley, P. Rothemund, and C. Keplinger, "High-Strain Peano-HASEL Actuators," *Advanced Functional Materials*, vol. 30, no. 7, 2020.

[79] T. Wang, J. Zhang, Y. Li, J. Hong, and M. Y. Wang, "Electrostatic layer jamming variable stiffness for soft robotics," *IEEE/ASME Transactions on Mechatronics*, vol. 24, no. 2, pp. 424–433, 2019.

[80] J. P. Wissman, A. K. Ikei, K. Sampath, and C. A. Rohde, "Hydraulically amplified self-healing electrostatic (hasel) inspired actuators," *arXiv preprint arXiv:2102.13039*, 2021.

[81] X. Cheng, M. Yu, J. Ma, B. Li, Y. Zhang, P. Wang, and Z. Jiao, "An entirely soft varifocal lens based on an electro-hydraulic actuator," *Smart Materials and Structures*, vol. 29, no. 4, 2020.

[82] T. Wang, Y. Zhang, Z. Chen, and S. Zhu, "Parameter identification and model-based nonlinear robust control of fluidic soft bending actuators," *IEEE/ASME Transactions on Mechatronics*, vol. 24, no. 3, pp. 1346–1355, 2019.

[83] N. Kellaris, V. G. Venkata, P. Rothemund, and C. Keplinger, "An analytical model for the design of Peano-HASEL actuators with drastically improved performance," *Extreme Mechanics Letters*, vol. 29, 2019. Art. no. 100449.

[84] W.-B. Li, W.-M. Zhang, H.-X. Zou, Z.-K. Peng, and G. Meng, "A fast rolling soft robot driven by dielectric elastomer," *IEEE/ASME Transactions on Mechatronics*, vol. 23, no. 4, pp. 1630–1640, 2018.

[85] J. Cao, L. Qin, J. Liu, Q. Ren, C. C. Foo, H. Wang, H. P. Lee, and J. Zhu, "Untethered soft robot capable of stable locomotion using soft electrostatic actuators," *Extreme Mechanics Letters*, vol. 21, pp. 9–16, 2018.

[86] X. Ji, X. Liu, V. Cacucciolo, M. Imboden, Y. Civet, A. El Haitami, S. Cantin, Y. Perriard, and H. Shea, "An autonomous untethered fast soft robotic insect driven by low-voltage dielectric elastomer actuators," *Science Robotics*, vol. 4, no. 37, 2019.

[87] S. Kirkman, P. Rothemund, E. Acome, and C. Keplinger, "Electromechanics of planar hasel actuators," *Extreme Mechanics Letters*, vol. 48, 2021.

[88] S. K. Mitchell, X. Wang, E. Acome, T. Martin, K. Ly, N. Kellaris, V. G. Venkata, and C. Keplinger, “An Easy-to-Implement Toolkit to Create Versatile and High-Performance HASEL Actuators for Untethered Soft Robots,” *Advanced Science*, vol. 6, 2019. Art. no. 1900178.

[89] S. J. A. Koh, C. Keplinger, R. Kalteis, C.-C. Foo, R. Baumgartner, S. Bauer, and Z. Suo, “High-performance electromechanical transduction using laterally-constrained dielectric elastomers part I: Actuation processes,” *Journal of the Mechanics and Physics of Solids*, vol. 105, pp. 81–94, 2017.

[90] N. Kellaris, P. Rothemund, Y. Zeng, S. K. Mitchell, G. M. Smith, K. Jayaram, and C. Keplinger, “Spider-Inspired Electrohydraulic Actuators for Fast, Soft-Actuated Joints,” *Advanced Science*, vol. 8, no. 14, pp. 1–16, 2021.

[91] C. Schunk, L. Pearson, E. Acome, T. G. Morrissey, N. Correll, C. Keplinger, M. E. Rentschler, and J. S. Humbert, “System Identification and Closed-Loop Control of a Hydraulically Amplified Self-Healing Electrostatic (HASEL) Actuator,” in *IEEE International Conference on Intelligent Robots and Systems*, (Madrid, Spain), pp. 6417–6423, October 2018.

[92] K. Ly, N. Kellaris, D. McMorris, B. K. Johnson, E. Acome, V. Sundaram, M. Naris, J. S. Humbert, M. E. Rentschler, C. Keplinger, *et al.*, “Miniaturized circuitry for capacitive self-sensing and closed-loop control of soft electrostatic transducers,” *Soft Robotics*, vol. 8, no. 6, pp. 673–686, 2021.

[93] P. Rothemund, N. Kellaris, S. K. Mitchell, E. Acome, and C. Keplinger, “Hasel artificial muscles for a new generation of lifelike robots—recent progress and future opportunities,” *Advanced Materials*, vol. 33, no. 19, 2021.

[94] Z. Yoder, N. Kellaris, C. Chase-Markopoulou, D. Ricken, S. K. Mitchell, M. B. Emmett, R. F. Weir, J. Segil, and C. Keplinger, “Design of a High-Speed Prosthetic Finger Driven by Peano-HASEL Actuators,” *Frontiers in Robotics and AI*, vol. 7, no. November, pp. 1–17, 2020.

[95] A. Volchko, S. K. Mitchell, T. G. Morrissey, and J. S. Humbert, “Model-based data-driven system identification and controller synthesis framework for precise control of siso and miso hasel-powered robotic systems,” in *2022 IEEE 5th International Conference on Soft Robotics (RoboSoft)*, (Edinburgh Scotland, United Kingdom), pp. 209–216, IEEE, April 2022.

[96] C. Christianson, C. Bayag, G. Li, S. Jadhav, A. Giri, C. Agba, T. Li, and M. T. Tolley, “Jellyfish-inspired soft robot driven by fluid electrode dielectric organic robotic actuators,” *Frontiers in Robotics and AI*, vol. 6, p. 126, 2019.

[97] Y. Wang, U. Gupta, J. Zhu, P. Li, D. Du, L. Zhang, J. Ouyang, J. Liu, and C. C. Foo, “Bio-inspired soft robot driven by transparent artificial muscle,” in *2019 IEEE International Conference on Robotics and Biomimetics (ROBIO)*, (Dali, Yunnan, China), pp. 1959–1964, December 2019.

[98] J. Liang, Y. Wu, J. K. Yim, H. Chen, Z. Miao, H. Liu, Y. Liu, Y. Liu, D. Wang, W. Qiu, *et al.*, “Electrostatic footpads enable agile insect-scale soft robots with trajectory control,” *Science Robotics*, vol. 6, no. 55, 2021.

[99] T. A. Gisby, B. M. O’Brien, S. Q. Xie, E. P. Calius, and I. A. Anderson, “Closed loop control of dielectric elastomer actuators,” in *Electroactive Polymer Actuators and Devices (EAPAD) 2011*, vol. 7976, (San Diego, California), April 2011.

[100] G. Rizzello, D. Naso, A. York, and S. Seelecke, “Closed loop control of dielectric elastomer actuators based on self-sensing displacement feedback,” *Smart Materials and Structures*, vol. 25, no. 3, 2016.

[101] T. A. Gisby, E. P. Calius, S. Xie, and I. A. Anderson, “An adaptive control method for dielectric elastomer devices,” in *Electroactive Polymer Actuators and Devices (EAPAD) 2008*, vol. 6927, (San Diego, California), March 2008.

[102] R. L. Truby, “Designing soft robots as robotic materials,” *Accounts of Materials Research*, vol. 2, no. 10, pp. 854–857, 2021.

[103] G. Stewart and D. A. Cooley, *The skeletal and muscular systems.* Infobase Publishing, 2009.

[104] N. A. Campbell, J. B. Reece, and L. G. Mitchell, *Biology.* Benjamin Cummings, 1999.

[105] R. Pfeifer, M. Lungarella, and F. Iida, "Self-organization, embodiment, and biologically inspired robotics," *science*, vol. 318, no. 5853, pp. 1088–1093, 2007.

[106] M. Cianchetti, "Embodied intelligence in soft robotics through hardware multifunctionality," *Frontiers in Robotics and AI*, p. 366, 2021.

[107] "Wave-handling," brochure no. 54817, Festo, 2013. accessed July 11, 2022.

[108] W. Carrigan, P. Nuthi, C. Pande, C. P. Nothnagle, and M. B. J. Wijesundara, "A pressure modulating sensorized soft actuator array for pressure ulcer prevention," in *International Design Engineering Technical Conferences and Computers and Information in Engineering Conference*, vol. 58158, (Las Vegas, Nevada), September 2017.

[109] B. Mosadegh, A. D. Mazzeo, R. F. Shepherd, S. A. Morin, U. Gupta, I. Z. Sani, D. Lai, S. Takayama, and G. M. Whitesides, "Control of soft machines using actuators operated by a braille display," *Lab on a Chip*, vol. 14, no. 1, pp. 189–199, 2014.

[110] T. Wang, J. Zhang, J. Hong, and M. Y. Wang, "Dielectric elastomer actuators for soft wave-handling systems," *Soft robotics*, vol. 4, no. 1, pp. 61–69, 2017.

[111] A. De Acutis, L. Calabrese, A. Bau, V. Tincani, N. M. Pugno, A. Bicchi, and D. E. De Rossi, "Design and proof of concept for multi degree of freedom hydrostatically coupled dielectric elastomer actuators with roto-translational kinematics for object handling," *Smart Materials and Structures*, vol. 27, no. 7, 2018.

[112] R. Hashem, B. Smith, D. Browne, W. Xu, and M. Stommel, "Control of a soft-bodied xy peristaltic table for delicate sorting," in *2016 IEEE 14th International Workshop on Advanced Motion Control (AMC)*, (Auckland, New Zealand), pp. 358–363, April 2016.

[113] K. Liu, F. Hacker, and C. Daraio, "Robotic surfaces with reversible, spatiotemporal control for shape morphing and object manipulation," *Science Robotics*, vol. 6, no. 53, 2021.

[114] M. Coelho and J. Zigelbaum, "Shape-changing interfaces," *Personal and Ubiquitous Computing*, vol. 15, no. 2, pp. 161–173, 2011.

[115] P. M. Khin, J. H. Low, W. W. Lee, S. L. Kukreja, H. L. Ren, N. V. Thakor, and C.-H. Yeow, “Soft haptics using soft actuator and soft sensor,” in *2016 6th IEEE International Conference on Biomedical Robotics and Biomechatronics (BioRob)*, (Singapore), pp. 1272–1276, June 2016.

[116] H. Phung, P. T. Hoang, C. T. Nguyen, T. D. Nguyen, H. Jung, U. Kim, and H. R. Choi, “Interactive haptic display based on soft actuator and soft sensor,” in *2017 IEEE/RSJ International Conference on Intelligent Robots and Systems (IROS)*, (Vancouver, Canada), pp. 886–891, September 2017.

[117] H. Zhao, A. M. Hussain, A. Israr, D. M. Vogt, M. Duduta, D. R. Clarke, and R. J. Wood, “A wearable soft haptic communicator based on dielectric elastomer actuators,” *Soft robotics*, vol. 7, no. 4, pp. 451–461, 2020.

[118] Z. Deng, M. Stommel, and W. Xu, “A novel soft machine table for manipulation of delicate objects inspired by caterpillar locomotion,” *IEEE/ASME Transactions on Mechatronics*, vol. 21, no. 3, pp. 1702–1710, 2016.

[119] K. P. Becker, Y. Chen, and R. J. Wood, “Mechanically programmable dip molding of high aspect ratio soft actuator arrays,” *Advanced Functional Materials*, vol. 30, no. 12, 2020.

[120] M. Stommel and W. Xu, “Optimal, efficient sequential control of a soft-bodied, peristaltic sorting table,” *IEEE Transactions on Automation Science and Engineering*, vol. 13, no. 2, pp. 858–867, 2015.

[121] B. K. Johnson, V. Sundaram, M. Naris, E. Acome, K. Ly, N. Correll, C. Keplinger, J. S. Humbert, and M. E. Rentschler, “Identification and control of a nonlinear soft actuator and sensor system,” *IEEE Robotics and Automation Letters*, vol. 5, no. 3, pp. 3783–3790, 2020. Reprinted with permission, ©2020 IEEE.

[122] S. Follmer, D. Leithinger, A. Olwal, A. Hogge, and H. Ishii, “inform: dynamic physical affordances and constraints through shape and object actuation.,” in *Proceedings of the 26th annual ACM symposium on User interface Software and Technology*, vol. 13, (St. Andrews Scotland, United Kingdom), pp. 417–426, October 2013.

[123] N. Correll, P. Dutta, R. Han, and K. Pister, "New directions: Wireless robotic materials," in *15th ACM Conference on Embedded Networked Sensor Systems (SenSys)*, (Delft, The Netherlands), pp. 1–6, November 2017.

[124] M. A. McEvoy and N. Correll, "Materials that couple sensing, actuation, computation, and communication," *Science*, vol. 347, no. 6228, 2015.

[125] S. C. Goldstein, J. D. Campbell, and T. C. Mowry, "Programmable matter," *IEEE Computer*, vol. 38, no. 6, pp. 99–101, 2005.

[126] L. Jing, K. Li, H. Yang, and P.-Y. Chen, "Recent advances in integration of 2d materials with soft matter for multifunctional robotic materials," *Materials Horizons*, vol. 7, no. 1, pp. 54–70, 2020.

[127] B. T. Kirby, M. Ashley-Rollman, and S. C. Goldstein, "Blinky blocks: a physical ensemble programming platform," in *CHI'11 extended abstracts on human factors in computing systems*, (Vancouver, BC, Canada), pp. 1111–1116, May 2011.

[128] K. Gilpin, A. Knaian, and D. Rus, "Robot pebbles: One centimeter modules for programmable matter through self-disassembly," in *2010 IEEE International Conference on Robotics and Automation*, (Anchorage, Alaska), pp. 2485–2492, IEEE, May 2010.

[129] H. Profita, N. Farrow, and N. Correll, "Flutter: An exploration of an assistive garment using distributed sensing, computation and actuation," in *Proceedings of the Ninth International Conference on Tangible, Embedded, and Embodied Interaction*, (Stanford, California), pp. 359–362, January 2015.

[130] C. S. Haines, M. D. Lima, N. Li, G. M. Spinks, J. Foroughi, M. J. D. W., S. H. Kim, S. Fang, M. Jung de Andrade, *et al.*, "Artificial Muscles from Fishing Line and Sewing Thread," *Science*, vol. 343, no. 6173, pp. 868–872, 2014.

[131] F. Sassa and K. Hayashi, "Flexible Thermal Actuator Film for Monolithic Soft Micro Robot Process," in *Proc. IEEE Sensors*, (New Delhi, India), October 2018.

[132] J. C. Case, E. L. White, and R. K. Kramer, "Soft material characterization for robotic applications," *Soft Robotics*, vol. 2, no. 2, pp. 80–87, 2015.

[133] C. Keplinger, M. Kaltenbrunner, N. Arnold, and S. Bauer, "Capacitive extensometry for transient strain analysis of dielectric elastomer actuators," *Applied Physics Letters*, vol. 92, no. 19, 2008. Art. no. 192903.

[134] D. J. Lipomi, M. Vosgueritchian, B. C.-K. Tee, S. L. Hellstrom, J. A. Lee, C. H. Fox, and Z. Bao, "Skin-like pressure and strain sensors based on transparent elastic films of carbon nanotubes," *Nature Nanotechnology*, vol. 6, pp. 788–792, 2011.

[135] M. Amjadi, K. U. Kyung, I. Park, and M. Sitti, "Stretchable, Skin-Mountable, and Wearable Strain Sensors and Their Potential Applications: A Review," *Advanced Functional Materials*, vol. 26, no. 11, pp. 1678–1698, 2016.

[136] L. Ljung, *System Identification: Theory for the User*. Upper Saddle River, NJ: Prentice-Hall, 1999.

[137] X. Rui, M. Ke, Q. Feng, and W. Zhen-Lei, "Online wavelet denoising via a moving window," *Acta Automatica Sinica*, vol. 33, no. 9, pp. 897–901, 2007.

[138] R. S. Stanković and B. J. Falkowski, "The haar wavelet transform: its status and achievements," *Computers & Electrical Engineering*, vol. 29, no. 1, pp. 25–44, 2003.

[139] N. Farrow and N. Correll, "A soft pneumatic actuator that can sense grasp and touch," in *2015 IEEE/RSJ International Conference on Intelligent Robots and Systems (IROS)*, (Hamburg, Germany), pp. 2317–2323, September 2015.

[140] S. A. Manzano, P. Xu, K. Ly, R. Shepherd, and N. Correll, "High-bandwidth nonlinear control for soft actuators with recursive network models," *arXiv preprint arXiv:2101.01139*, 2021.

[141] J. Lenz and S. Edelstein, "Magnetic sensors and their applications," *IEEE Sensors journal*, vol. 6, no. 3, pp. 631–649, 2006.

[142] J. J. Clark, "A magnetic field based compliance matching sensor for high resolution, high compliance tactile sensing," in *Proceedings. 1988 IEEE International Conference on Robotics and Automation*, (Philadelphia, Pennsylvania), pp. 772–777, April 1988.

[143] T. Paulino, P. Ribeiro, M. Neto, S. Cardoso, A. Schmitz, J. Santos-Victor, A. Bernardino, and L. Jamone, “Low-cost 3-axis soft tactile sensors for the human-friendly robot vizzy,” in *2017 IEEE international conference on robotics and automation (ICRA)*, (Singapore), pp. 966–971, May 2017.

[144] M. H. bin Rosle, R. Kojima, Z. Wang, and S. Hirai, “Soft fingertip with tactile sensation for detecting grasping orientation of thin object,” in *2018 IEEE International Conference on Robotics and Biomimetics (ROBIO)*, (Kuala Lumpur, Malaysia), pp. 1304–1309, December 2018.

[145] L. Jamone, L. Natale, G. Metta, and G. Sandini, “Highly sensitive soft tactile sensors for an anthropomorphic robotic hand,” *IEEE sensors Journal*, vol. 15, no. 8, pp. 4226–4233, 2015.

[146] H. Wang, G. De Boer, J. Kow, A. Alazmani, M. Ghajari, R. Hewson, and P. Culmer, “Design methodology for magnetic field-based soft tri-axis tactile sensors,” *Sensors*, vol. 16, no. 9, 2016.

[147] Y. Yan, Z. Hu, Z. Yang, W. Yuan, C. Song, J. Pan, and Y. Shen, “Soft magnetic skin for super-resolution tactile sensing with force self-decoupling,” *Science Robotics*, vol. 6, no. 51, 2021.

[148] T. Hellebrekers, O. Kroemer, and C. Majidi, “Soft magnetic skin for continuous deformation sensing,” *Advanced Intelligent Systems*, vol. 1, no. 4, 2019.

[149] A. S. Almansouri, N. A. Alsharif, M. A. Khan, L. Swanepoel, A. Kaidarova, K. N. Salama, and J. Kosel, “An imperceptible magnetic skin,” *Advanced Materials Technologies*, vol. 4, no. 10, 2019.

[150] M. Luo, E. H. Skorina, W. Tao, F. Chen, S. Ozel, Y. Sun, and C. D. Onal, “Toward modular soft robotics: Proprioceptive curvature sensing and sliding-mode control of soft bidirectional bending modules,” *Soft robotics*, vol. 4, no. 2, pp. 117–125, 2017.

[151] H. Mirzanejad and M. Agheli, “Soft force sensor made of magnetic powder blended with silicone rubber,” *Sensors and Actuators A: Physical*, vol. 293, pp. 108–118, 2019.

[152] S. Wu, W. Hu, Q. Ze, M. Sitti, and R. Zhao, "Multifunctional magnetic soft composites: a review," *Multifunctional materials*, vol. 3, no. 4, 2020.

[153] V. Sundaram, K. Ly, B. K. Johnson, M. Naris, M. Anderson, J. S. Humbert, N. Correll, and M. E. Rentschler, "Embedded magnetic sensing for feedback control of soft hasel actuator," *IEEE Transactions on Robotics*, 2022. accepted (preprint), reproduced with permission.

[154] S. Schlatter, P. Illenberger, and S. Rosset, "Peta-pico-voltron: An open-source high voltage power supply," *HardwareX*, vol. 4, 2018.

[155] J. Bezanson, A. Edelman, S. Karpinski, and V. B. Shah, "Julia: A fresh approach to numerical computing," *SIAM review*, vol. 59, no. 1, pp. 65–98, 2017.

[156] M. Rolf and J. J. Steil, "Constant curvature continuum kinematics as fast approximate model for the bionic handling assistant," in *2012 IEEE/RSJ International Conference on Intelligent Robots and Systems*, (Vilamoura, Portugal), pp. 3440–3446, October 2012.

[157] I. D. Walker, "Continuous backbone "continuum" robot manipulators," *International Scholarly Research Notices*, vol. 2013, 2013.

[158] K. Cao, R. Kang, D. T. Branson III, S. Geng, Z. Song, and J. S. Dai, "Workspace analysis of tendon-driven continuum robots based on mechanical interference identification," *Journal of Mechanical Design*, vol. 139, no. 6, 2017.

[159] A. Chawla, C. Frazelle, and I. Walker, "A comparison of constant curvature forward kinematics for multisection continuum manipulators," in *2018 Second IEEE International Conference on Robotic Computing (IRC)*, (Laguna Hills, California), pp. 217–223, January 2018.

[160] B. A. Jones and I. D. Walker, "Kinematics for multisection continuum robots," *IEEE Transactions on Robotics*, vol. 22, no. 1, pp. 43–55, 2006.

[161] R. J. Webster III and B. A. Jones, "Design and kinematic modeling of constant curvature continuum robots: A review," *The International Journal of Robotics Research*, vol. 29, no. 13, pp. 1661–1683, 2010.

[162] T. Li, G. Li, Y. Liang, T. Cheng, J. Dai, X. Yang, B. Liu, Z. Zeng, Z. Huang, Y. Luo, *et al.*, "Fast-moving soft electronic fish," *Science advances*, vol. 3, no. 4, 2017.

[163] M. Rogóż, H. Zeng, C. Xuan, D. S. Wiersma, and P. Wasylczyk, "Light-driven soft robot mimics caterpillar locomotion in natural scale," *Advanced Optical Materials*, vol. 4, no. 11, pp. 1689–1694, 2016.

[164] A. F. Siu, E. J. Gonzalez, S. Yuan, J. B. Ginsberg, and S. Follmer, "Shapeshift: 2d spatial manipulation and self-actuation of tabletop shape displays for tangible and haptic interaction," in *Proceedings of the 2018 CHI Conference on Human Factors in Computing Systems*, (Montreal, QC, Canada), pp. 1–13, April 2018.

[165] N. Besse, S. Rosset, J. J. Zarate, and H. Shea, "Flexible active skin: large reconfigurable arrays of individually addressed shape memory polymer actuators," *Advanced Materials Technologies*, vol. 2, no. 10, 2017.

[166] H. S. Lee, H. Phung, D.-H. Lee, U. K. Kim, C. T. Nguyen, H. Moon, J. C. Koo, H. R. Choi, *et al.*, "Design analysis and fabrication of arrayed tactile display based on dielectric elastomer actuator," *Sensors and Actuators A: Physical*, vol. 205, pp. 191–198, 2014.

[167] H. Phung, P. T. Hoang, H. Jung, T. D. Nguyen, C. T. Nguyen, and H. R. Choi, "Haptic display responsive to touch driven by soft actuator and soft sensor," *IEEE/ASME Transactions on Mechatronics*, vol. 26, no. 5, pp. 2495–2505, 2020.

[168] S. Kang, J. Lee, S. Lee, S. Kim, J.-K. Kim, H. Algadi, S. Al-Sayari, D.-E. Kim, D. Kim, and T. Lee, "Highly sensitive pressure sensor based on bioinspired porous structure for real-time tactile sensing," *Advanced Electronic Materials*, vol. 2, no. 12, 2016.

[169] S. C. B. Mannsfeld, B. C. K. Tee, R. M. Stoltenberg, C. V. Chen, S. Barman, B. V. O. Muir, A. N. Sokolov, C. Reese, and Z. Bao, "Highly sensitive flexible pressure sensors with microstructured rubber dielectric layers," *Nature Materials*, vol. 9, no. 10, pp. 859–864, 2010.

[170] N. Day, J. Penaloza, V. J. Santos, and M. D. Killpack, "Scalable fabric tactile sensor arrays for soft bodies," *Journal of Micromechanics and Microengineering*, vol. 28, no. 6, 2018.

[171] L. Shu, T. Hua, Y. Wang, Q. Li, D. D. Feng, and X. Tao, "In-shoe plantar pressure measurement and analysis system based on fabric pressure sensing array," *IEEE Transactions on information technology in biomedicine*, vol. 14, no. 3, pp. 767–775, 2010.

[172] M. Matysek, P. Lotz, T. Winterstein, and H. F. Schlaak, "Dielectric elastomer actuators for tactile displays," in *World Haptics 2009-Third Joint EuroHaptics conference and Symposium on Haptic Interfaces for Virtual Environment and Teleoperator Systems*, (Washington D.C.), pp. 290–295, March 2009.

[173] Y. Shao, S. Ma, S. H. Yoon, Y. Visell, and J. Holbery, "Surfaceflow: Large area haptic display via compliant liquid dielectric actuators," in *2020 IEEE Haptics Symposium (HAPTICS)*, (Washington D.C.), pp. 815–820, March 2020.

[174] N. H. Chuc, N. H. L. Vuong, D. S. Kim, H. P. Moon, J. C. Koo, Y. K. Lee, J.-D. Nam, and H. R. Choi, "Fabrication and control of rectilinear artificial muscle actuator," *IEEE/ASME Transactions on Mechatronics*, vol. 16, no. 1, pp. 167–176, 2010.

[175] P. Schoessler, D. Windham, D. Leithinger, S. Follmer, and H. Ishii, "Kinetic blocks: Actuated constructive assembly for interaction and display," in *Proceedings of the 28th Annual ACM Symposium on User Interface Software and Technology*, (Charlotte, North Carolina), pp. 341–349, November 2015.

[176] S. Dirven, F. Chen, W. Xu, J. E. Bronlund, J. Allen, and L. K. Cheng, "Design and characterization of a peristaltic actuator inspired by esophageal swallowing," *IEEE/ASME Transactions on Mechatronics*, vol. 19, no. 4, pp. 1234–1242, 2013.

[177] S. Din, W. Xu, L. K. Cheng, and S. Dirven, "A stretchable array of electronic receptors for esophageal swallowing robot for biomimetic simulations of bolus transport," *IEEE Sensors Journal*, vol. 18, no. 13, pp. 5497–5506, 2018.

[178] A. A. Stanley, K. Hata, and A. M. Okamura, "Closed-loop shape control of a haptic jamming deformable surface," in *2016 IEEE International Conference on Robotics and Automation (ICRA)*, (Stockholm, Sweden), pp. 2718–2724, May 2016.

[179] S. Lee, K. Jung, J. Koo, S. Lee, H. Choi, J. Jeon, J. Nam, and H. Choi, "Braille display device using soft actuator," in *Smart Structures and Materials 2004: Electroactive Polymer Actuators and Devices (EAPAD)*, vol. 5385, pp. 368–379, SPIE, 2004.

[180] G.-H. Feng and S.-Y. Hou, "A digital tactile actuator array with normal and shear contact force controllability for refreshable braille display application," in *2015 Transducers-2015 18th International Conference on Solid-State Sensors, Actuators and Microsystems (TRANSDUCERS)*, (Anchorage, Alaska), pp. 835–838, June 2015.

[181] X. Wu, S.-H. Kim, H. Zhu, C.-H. Ji, and M. G. Allen, "A refreshable braille cell based on pneumatic microbubble actuators," *Journal of Microelectromechanical Systems*, vol. 21, no. 4, pp. 908–916, 2012.

[182] Y. Kato, T. Sekitani, M. Takamiya, M. Doi, K. Asaka, T. Sakurai, and T. Someya, "Sheet-type braille displays by integrating organic field-effect transistors and polymeric actuators," *IEEE Transactions on Electron Devices*, vol. 54, no. 2, pp. 202–209, 2007.

[183] R. H. Heisser, C. A. Aubin, O. Peretz, N. Kincaid, H. S. An, E. M. Fisher, S. Sobhani, P. Pepiot, A. D. Gat, and R. F. Shepherd, "Valveless microliter combustion for densely packed arrays of powerful soft actuators," *Proceedings of the National Academy of Sciences*, vol. 118, no. 39, 2021.

[184] J. E. Luntz, W. Messner, and H. Choset, "Distributed manipulation using discrete actuator arrays," *The International Journal of Robotics Research*, vol. 20, no. 7, pp. 553–583, 2001.

[185] G. Paschew and A. Richter, "High-resolution tactile display operated by an integrated 'smart hydrogel' actuator array," in *Electroactive Polymer Actuators and Devices (EAPAD) 2010*, vol. 7642, (San Diego, California), pp. 856–863, April 2010.

[186] K. Ly, J. V. Mayekar, S. Aguasvivas, C. Keplinger, M. E. Rentschler, and N. Correll, "Electro-hydraulic rolling soft wheel: Design, hybrid dynamic modeling, and model predictive control," *IEEE Transactions on Robotics*, pp. 1–20, 2022. paper published online before print.

[187] Y.-S. Seo, S. J. Cho, J.-Y. Lee, C. Park, U. Kim, S. Lee, B. Kim, C. Park, and S.-H. Song, "Human-mimetic soft robot joint for shock absorption through joint dislocation," *Bioinspiration and biomimetics*, vol. 15, no. 1, 2019.

[188] M. Quigley, K. Conley, B. Gerkey, J. Faust, T. Foote, J. Leibs, R. Wheeler, A. Y. Ng, *et al.*, "Ros: an open-source robot operating system," in *ICRA workshop on open source software*, vol. 3, (Kobe, Japan), p. 5, 2009.

[189] S. Danisch and J. Krumbiegel, "Makie. jl: Flexible high-performance data visualization for julia," *Journal of Open Source Software*, vol. 6, no. 65, 2021.

[190] M. F. Sanner, "Python: a programming language for software integration and development," *Journal of Molecular Graphics and Modelling*, vol. 17, no. 1, pp. 57–61, 1999.

[191] G. Bradski and A. Kaehler, "Opencv," *Dr. Dobb's Journal of Software Tools*, vol. 3, p. 120, 2000.

[192] M. K. Rasmussen, E. W. Pedersen, M. G. Petersen, and K. Hornbæk, "Shape-changing interfaces: a review of the design space and open research questions," in *Proceedings of the CHI Conference on Human Factors in Computing Systems*, (Austin, Texas), pp. 735–744, May 2012.

[193] J. Alexander, A. Roudaut, J. Steimle, K. Hornbæk, M. Bruns Alonso, S. Follmer, and T. Merritt, "Grand challenges in shape-changing interface research," in *Proceedings of the 2018 CHI Conference on Human Factors in Computing Systems*, (Montreal, Canada), pp. 1–14, April 2018.

[194] D. Leithinger, S. Follmer, A. Olwal, and H. Ishii, "Shape displays: Spatial interaction with dynamic physical form," *IEEE computer graphics and applications*, vol. 35, no. 5, pp. 5–11, 2015.

[195] K. Nakagaki, D. Fitzgerald, Z. Ma, L. Vink, D. Levine, and H. Ishii, "inforce: Bi-directional 'force' shape display for haptic interaction," in *Proceedings of the Thirteenth International Conference on Tangible, Embedded, and Embodied Interaction*, (Tempe, Arizona), pp. 615–623, March 2019.

[196] O. Khatib, “Real-time obstacle avoidance for manipulators and mobile robots,” in *1985 IEEE International Conference on Robotics and Automation*, (St. Louis, MO, USA), pp. 500–505, March 1985.

[197] J. Barraquand, B. Langlois, and J.-C. Latombe, “Numerical potential field techniques for robot path planning,” *IEEE transactions on systems, man, and cybernetics*, vol. 22, no. 2, pp. 224–241, 1992.

[198] Y. Koren, J. Borenstein, *et al.*, “Potential field methods and their inherent limitations for mobile robot navigation.,” in *Proceedings of the 1991 IEEE International Conference on Robotics and Automation*, vol. 2, (Sacramento, California), pp. 1398–1404, April 1991.

[199] R. Zappulla, H. Park, J. Virgili-Llop, and M. Romano, “Real-time autonomous spacecraft proximity maneuvers and docking using an adaptive artificial potential field approach,” *IEEE Transactions on Control Systems Technology*, vol. 27, no. 6, pp. 2598–2605, 2018.

[200] M. C. Lee and M. G. Park, “Artificial potential field based path planning for mobile robots using a virtual obstacle concept,” in *Proceedings of the 2003 IEEE/ASME International Conference on Advanced Intelligent Mechatronics (AIM 2003)*, vol. 2, (Kobe, Japan), pp. 735–740, July 2003.

[201] L. Huang, “Velocity planning for a mobile robot to track a moving target—a potential field approach,” *Robotics and Autonomous Systems*, vol. 57, no. 1, pp. 55–63, 2009.

[202] X. Xu, Y. Hu, J. Zhai, L. Li, and P. Guo, “A novel non-collision trajectory planning algorithm based on velocity potential field for robotic manipulator,” *International Journal of Advanced Robotic Systems*, vol. 15, no. 4, 2018.

[203] C. M. Saaj, V. Lappas, and V. Gazi, “Spacecraft swarm navigation and control using artificial potential field and sliding mode control,” in *2006 IEEE International Conference on Industrial Technology*, (Mumbai, India), pp. 2646–2651, December 2006.

[204] M. Zhang, Y. Shen, Q. Wang, and Y. Wang, “Dynamic artificial potential field based multi-robot formation control,” in *2010 IEEE Instrumentation and Measurement Technology Conference Proceedings*, (Austin, Texas), pp. 1530–1534, May 2010.

[205] K. H. Kowdiki, R. K. Barai, and S. Bhattacharya, "Leader-follower formation control using artificial potential functions: A kinematic approach," in *IEEE International Conference On Advances In Engineering, Science And Management (ICAESM-2012)*, (Nagapattinam, Tamil Nadu, India), pp. 500–505, March 2012.

[206] M. N. Brearley and N. J. De Mestre, "Rolling of a rigid ball on a horizontal deformable surface," *The ANZIAM Journal*, vol. 46, no. 2, pp. 249–264, 2004.

[207] F. E. Schneider and D. Wildermuth, "A potential field based approach to multi robot formation navigation," in *2003 IEEE International Conference on Robotics, Intelligent Systems and Signal Processing*, vol. 1, (Changsha, China), pp. 680–685, October 2003.

[208] E. Fiorelli, N. E. Leonard, P. Bhatta, D. A. Paley, R. Bachmayer, and D. M. Fratantoni, "Multi-auv control and adaptive sampling in monterey bay," *IEEE journal of oceanic engineering*, vol. 31, no. 4, pp. 935–948, 2006.

[209] K. J. Åström and B. Wittenmark, *Adaptive control.* Courier Corporation, 2013.

[210] J. L. Proctor, S. L. Brunton, and J. N. Kutz, "Dynamic mode decomposition with control," *SIAM Journal on Applied Dynamical Systems*, vol. 15, no. 1, pp. 142–161, 2016.

[211] T. M. Mitchell, *Machine learning*, vol. 1. McGraw-hill New York, 1997.

[212] M. Seo, H. Kim, and Y. Choi, "Human mimetic forearm mechanism towards bionic arm," in *2017 International Conference on Rehabilitation Robotics (ICORR)*, (London, United Kingdom), pp. 1171–1176, July 2017.

[213] K. Kawaharazuka, S. Makino, M. Kawamura, Y. Asano, Y. Kakiuchi, K. Okada, and M. Inaba, "Human mimetic forearm design with radioulnar joint using miniature bone-muscle modules and its applications," in *2017 IEEE/RSJ International Conference on Intelligent Robots and Systems (IROS)*, (Vancouver, BC, Canada), pp. 4956–4962, IEEE, September 2017.

[214] X. Xu, Y. Hu, J. M. Zhai, L. Z. Li, and P. S. Guo, "A novel non-collision trajectory planning algorithm based on velocity potential field for robotic manipulator," *International Journal of Advanced Robotic Systems*, vol. 15, no. 4, 2018.